# Generating and characterizing single molecules by atomic force microscopy and scanning tunneling microscopy


Dissertation zur Erlangung des Doktorgrades
der Naturwissenschaften (Dr. rer. nat.)
der Fakultät für Physik
der Universität Regensburg

vorgelegt von

**Katharina Kaiser**

aus Wiesbaden

2021

Die Arbeit wurde von Dr. Leo Gross und Prof. Dr. Jascha Repp angeleitet.
Das Promotionsgesuch wurde am 7. April 2021 eingereicht.
Das Promotionskolloquium fand am 17. Juni 2021 statt.

Prüfungsausschuss: Vorsitzender: Prof. Dr. Andrea Donarini
1. Gutachter: Prof. Dr. Jascha Repp
2. Gutachter: PD Dr. Andreas K. Hüttel
weiterer Prüfer: Prof. Dr. Isabella Gierz-Pehla

# Contents

# Introduction

Scanning tunneling microscopy (STM) and atomic force microscopy (AFM) have opened the door to atomic-scale investigations of surfaces. Since their invention in the 1980s[1,2] several related techniques, known collectively as scanning probe microscopy (SPM), have been developed. SPM-based techniques have been refined and advanced and are nowadays indispensable in experimental nanoscience, as for example in the investigation of single adsorbates. In this thesis, I will examine different aspects of STM- and AFM-based characterization of single molecules.

**Structure elucidation**

Imaging the chemical structure of a molecule by frequency-modulation AFM[3] has been enabled by two major advancements in the field, namely the invention of the qPlus sensor[4] and the introduction of tip-functionalization.[5] While the qPlus sensor allows for stable AFM operation with sub-Ångström oscillation amplitudes, decorating the apex of a metallic tip with an inert atom or molecule allows entering tip-sample distance regimes in which repulsive forces due to the Pauli repulsion between regions of high electron density within tip and molecule become accessible. This facilitates the visualization of atoms and single chemical bonds within a molecule with bond-order resolution, thus even allowing for bond-order analysis or the characterization of a molecule's aromaticity.[6,7] In addition to AFM-based structure elucidation, STM can provide information on the electronic properties of the probed species. Here, the introduction of a thin dielectric spacer layer was a vital step towards the atomic-scale characterization of single molecules. It entails electronic decoupling of the adsorbed molecule from the metallic substrate and thus allows electronic structure investigations such as measuring electron affinity and ionization potential levels or mapping the spatial distribution of frontier orbital densities.[8]

An example of the capability of AFM and STM to resolve and identify structures of *a priori* unknown molecules is given in 8. Here, we characterized molecules extracted from two different stages of the soot formation mechanism, providing unprecedented insights into the complex mechanisms of carbon nanoparticle formation in fuel combustion.

**Atom manipulation**

Already shortly after the first implementation of STM its potential to not only image single atoms but also to deliberately move them with the tip was explored.[9] Within the following 30 years, atom manipulation in SPM has made tremendous progress and it was shown that it is not only possible to move[9–12] or pick up/drop[13,14] single adsorbates but also to break and form bonds[15–18] with high precision. One major advantage of this approach compared to large-scale on-surface synthesis (for example by annealing of precursor molecules adsorbed on a surface) is that it is not necessarily limited to metallic substrates but can be extended to ultrathin insulating layers[19–21] or even thick insulating films.[22] Hence, on-surface synthesis by atom manipulation provides an opportunity to generate highly-reactive molecules in an inert environment. In combination with bond-resolved AFM it is then possible to identify and characterize products or even intermediates of on-surface chemical reactions.[23–25]

This is demonstrated by the formation and subsequent investigation of cyclo[18]carbon, a highly reactive purely *sp*-hybridized carbon allotrope, by tip-induced on-surface synthesis

in chapter 9. We were able to form cyclo[18]carbon from two different precursor molecules, which allows us to compare the yield for the unmasking reaction for two different masking groups. By comparison of experimental AFM images with AFM simulations of different geometrical structures of cyclo[18]carbon we propose a ground state structure for $C_{18}$ adsorbed on bilayer NaCl on Cu(111). This also allows us to investigate how bond length and bond angle alternation within a molecule affect the image contrast in constant-height AFM.

**Luminescence**

In the early 1990s it was shown that luminescence can be observed from the tip-sample junction of an STM,[26] demonstrating yet another possibility for scanning probe-based surface characterization. However, only 13 years later the STM-induced luminescence (STML) of a single isolated molecule was demonstrated.[27] Again, the introduction of a decoupling layer turned out to be crucial to overcome limitations arising from fluorescence quenching from the metallic substrate. By now, vibronically resolved emission from single molecules with sub-molecular spatial resolution and energy resolution comparable to Raman spectroscopy can be achieved.[28,29]

Combining high-resolution AFM and STML to facilitate correlating structural motifs with optical properties is a natural step in advancing the toolbox for characterizing single molecules provided by SPM. A first step in this direction is described in chapter 10, where we combine high-resolution AFM with an optical setup, allowing for the detection of light emitted in STML. This approach allows characterizing the optical and electronic properties of single vanadyl-phthalocyanine molecules as well as investigating the change in those properties upon a tip-induced chemical reaction, *i.e.*, the removal of an oxygen atom generating vanadium-phthalocyanine.

# Part I

# Scanning probe microscopy

## Chapter 1

# Brief introduction

In 1981 scanning tunneling microscopy (STM) was developed by G. Binnig and H. Rohrer,[1] allowing the investigation and imaging of structures down to the atomic scale by using a sharp metallic probe as a sensor. Only 4 years later, in 1985, the invention of the atomic force microscope (AFM) by G. Binnig and the subsequent realization in 1986 by G. Binnig, C. F. Quate and C. Gerber followed.[2] Since then, several techniques that exploit the interaction between a probe and a sample surface were developed, providing the possibility to study a variety of surface properties on the nanoscale.

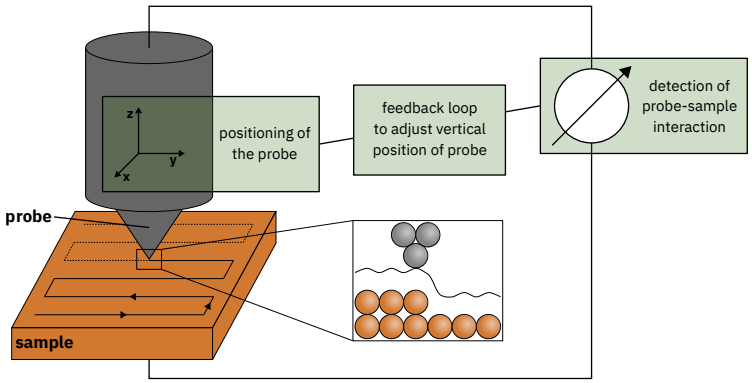


Figure 1.1: **Functional principle of SPM.** Probe in close proximity to a sample surface. A measurand that depends on the interaction between probe and sample is detected (*e.g.*, tunnel current in STM or change in resonance frequency in frequency-modulation AFM). The probe is scanned over the sample and at each pixel the measurand for probe-sample interaction is recorded. In addition, this measurand can be used as a feedback to adjust the distance between probe and sample.

Figure 1.1 introduces the basic concept of scanning probe microscopy (SPM): A probe is positioned in close proximity to a sample surface and scanned across that surface. At each scanning point certain properties of the sample are quantified by measuring physical quantities that relate to the interaction between probe and sample. For certain applications, these quantities are additionally handed over into a feedback loop to continuously adjust the distance between probe and sample. The recorded data is typically represented as a two-dimensional grid of data points.
This part will introduce and give an overview on the SPM techniques that are relevant to this thesis, namely STM and AFM.

## Chapter 2

# Scanning tunneling microscopy

As the name suggests, STM is based on the quantum mechanical tunnel effect. The wave function of a particle decays exponentially into regions with vanishing density of states that are classically forbidden.[30] As a result, the transmission probability of a particle with a certain kinetic energy through a potential barrier of finite height and a length that is on the order of the particle's decay length becomes non-zero. This phenomenon is referred to as tunneling. For charge carriers in a solid the decay length into vacuum is on the order of a few Å and hence, tunneling of charge carriers between two solids placed within that distance becomes measurable.

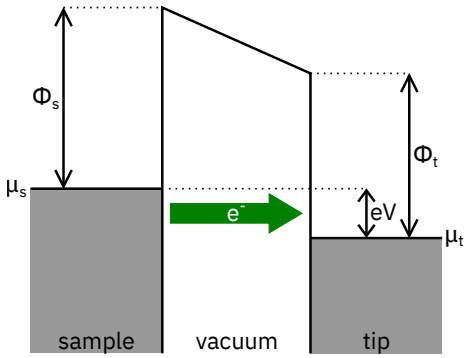


Figure 2.1: **Schematic energy level diagram of the tip-sample junction in STM.** At $T = 0$ K, all electronic states below the electrochemical potential of tip and sample ($\mu_t$ and $\mu_s$) are occupied. The energy to lift an electron from the highest occupied state of the tip (sample) above the vacuum barrier is given by the work function $\phi_t$ ($\phi_s$). If a bias voltage $V$ is applied between tip and sample (in this case negative sample bias voltage), the electrochemical potentials of tip and sample are shifted with respect to each other by $eV$. This allows for a net tunnel current of electrons from occupied sample to unoccupied tip states.

Figure 2.1 shows a schematic energy level diagram of the situation present in STM: A sharp metallic probe (tip) is placed in close vicinity to a conducting surface. Upon applying a bias voltage $V$ the electrochemical potentials of tip and sample $\mu_t$ and $\mu_s$ are shifted with respect to each other and a net tunnel current $I$ of electrons from occupied sample to unoccupied tip states (or *vice versa*, depending on the bias voltage polarity) is observed. The tunnel current decays exponentially for increasing tip-sample distance $z$ with

$$I \approx I_0 \cdot e^{-2\kappa z} \tag{2.1}$$

with the proportionality constant $I_0 = V \cdot G_0$ depending on the conductance quantum $G_0$, and the inverse decay constant

$$\kappa = \frac{\sqrt{2m_e\phi_b}}{\hbar}. \tag{2.2}$$

Here, $m_e$ is the electron mass and $\phi_b$ the height of the vacuum barrier.[31,32] For $eV \ll \phi_b$, $\phi_b$ corresponds approximately to the average work function of tip and sample. For the materials typically used in STM the barrier height is on the order of $\phi_b \approx 5$ eV, which yields a decay constant on the order of $\kappa \approx 1$ Å$^{-1}$. This means that a change in tip-sample distance by 1 Å results in a change in tunnel current by approximately a factor of 10.
Besides the distance dependence of the tunnel current, tunneling in a metal-insulator-metal junction can be described using a time-dependent perturbation theory approach, as developed by J. Bardeen.[31,33] In this approach, tip and sample are treated as two separate subsystems. The tunneling probability of an electron from one side to the other is given by Fermi's Golden Rule:

$$w = \frac{2\pi}{\hbar}|M|^2\rho_f \tag{2.3}$$

with the tunneling matrix element $M$ and the density of final states $\rho_f$. In the low-temperature limit, *i.e.*, small $k_BT$, the Fermi distribution can be approximated by a step function and the tunnel current at a given bias voltage is determined by the convolution of the local density of states (LDOS) of tip ($\rho_t$) and sample ($\rho_s$):

$$I = \frac{4\pi e}{\hbar}\int_0^{eV} \rho_t(\mu_s - eV + \epsilon)\rho_s(\mu_s + \epsilon)|M|^2 d\epsilon. \tag{2.4}$$

The tunneling matrix element is a surface integral of the tip and sample wave functions along a separation surface between tip and sample. Based on Bardeen's tunnel theory, J. Tersoff and D. R. Hamann introduced a model for STM imaging[34] in which the tip is modeled as a geometrical point. As a consequence, the properties of the tip can be excluded such that STM probes the electronic properties of the sample surface instead of properties of the combined tip-sample system. The expression for the tunnel current becomes

$$I \approx \frac{4\pi e}{\hbar}\rho_t|M|^2\int_0^{eV} \rho_s(\mu_s + \epsilon)d\epsilon \tag{2.5}$$

if within the probed energy interval (i) the tip state is spherically symmetric, (ii) $M$ is independent of the energy and (iii) the tip LDOS is constant. In the case of an $s$-wave tip, constant current STM topographies can then be interpreted as contours of constant LDOS. Within this model, the sample LDOS can be deduced from the differential conductance

$$\frac{dI}{dV}(V) \propto \rho_s(\mu_s + eV) \tag{2.6}$$

in scanning tunneling spectroscopy (STS).
This description serves as a good approximation for STM and STS with metallic tips, which typically exhibit an $s$-wave character. In a following work, C. J. Chen extended this theory by including a more sophisticated description of the tip wave function and introducing the so-called derivative rule.[35] The tunneling matrix elements can be obtained by replacing the angular dependence of the tip wave function with a derivative along the respective direction,

*i.e.*, $x \rightarrow {}^{\partial}/_{\partial x}$, $xz \rightarrow {}^{\partial^2}/_{\partial x \partial z}$, *etc.*.[36] Hence, in the case of a $p$-wave tip, $M$ is proportional to the derivative of the sample wave function at the position of the center of the apex atom $\vec{r}_0$, *i.e.*,

$$M_{pz} \propto \frac{\partial \psi(\vec{r}_0)}{\partial z} \tag{2.7}$$

for a $p_z$ tip state.

## STM on single molecules

In a seminal work, B. C. Stipe and co-workers used the STM to characterize a single molecule adsorbed on a metallic substrate.[37] Since then, a whole field has developed around the investigation and manipulation of single molecules using SPM in general. However, when adsorbed on a metallic surface, the presence of substrate electrons perturbs the electronic states of the molecule because of hybridization and electronic characterization is hampered. This problem could be circumvented, though, by introducing a dielectric spacer layer between molecule and metallic substrate. Insulating layers such as metal-oxide[38,39] or alkali-halide[8] layers of only a few atomic layers thickness provide a good decoupling while maintaining a sufficiently high conductance for stable STM operation.
STM on single molecules adsorbed on a thin insulating layer can be described in a double-barrier tunneling junction picture, as depicted in Fig. 2.2a-c. The energetic positions of the molecular states with respect to the vacuum level are fixed and given by the ionization potential (IP, energy needed to remove an electron from the molecule) and the electron affinity (EA, energy gained by attaching an additional electron to the molecule)[a]. Those two quantities together with the sample's work function and the potential drop within the dielectric spacer layer yield the positions of the molecule's ion resonances with respect to the sample's electrochemical potential. The potential drop between tip and sample within the different dielectrics is determined by their dielectric constant. For bilayer NaCl and the typical tip-sample distances used in this thesis it is on the order of $5 - 10\%$ of the potential drop in the tip-sample gap.[40,41] The energetic positions of the positive (PIR) and negative ion resonance (NIR) of a molecule adsorbed on a thin insulating layer can be probed by changing the applied bias voltage; as the tip's electrochemical potential passes the ion resonances, the molecular states can be populated/depopulated with electrons tunneling to or from tip and sample (Fig. 2.2b, c). Figure 2.2c, for example, depicts the situation for a positive sample bias voltage: The electrochemical potential of the tip is shifted above the NIR of the molecule allowing electron transfer from the tip to the molecule and the molecule is (transiently) charged negatively. A subsequent electron transfer from the anion to the sample restores the neutral charge state of the molecule. In STS, a molecule's PIR and NIR are visible as peaks in ${}^{\mathrm{d}I}/_{\mathrm{d}V}$ at the corresponding bias voltages, as shown in Fig. 2.2d for pentacene adsorbed on bilayer NaCl on Cu(111)(see ref. [8]). Imaging at the corresponding bias voltages reveals orbital density images of the highest occupied (HOMO) and lowest unoccupied (LUMO) molecular orbital (Fig. 2.2e, see ref. [8]). However, the picture shown in Fig. 2.2b, c is strongly simplified and does not take into account effects like broadening of the molecular energy levels due to electron-phonon coupling with the

[a] Because of the polarizability of the substrate and associated screening of the charges within the molecule, the energy levels of a molecule adsorbed on a polarizable substrate are shifted towards the sample's electrochemical potential and thus do not correspond to the IP and EA of the free molecule.[8]

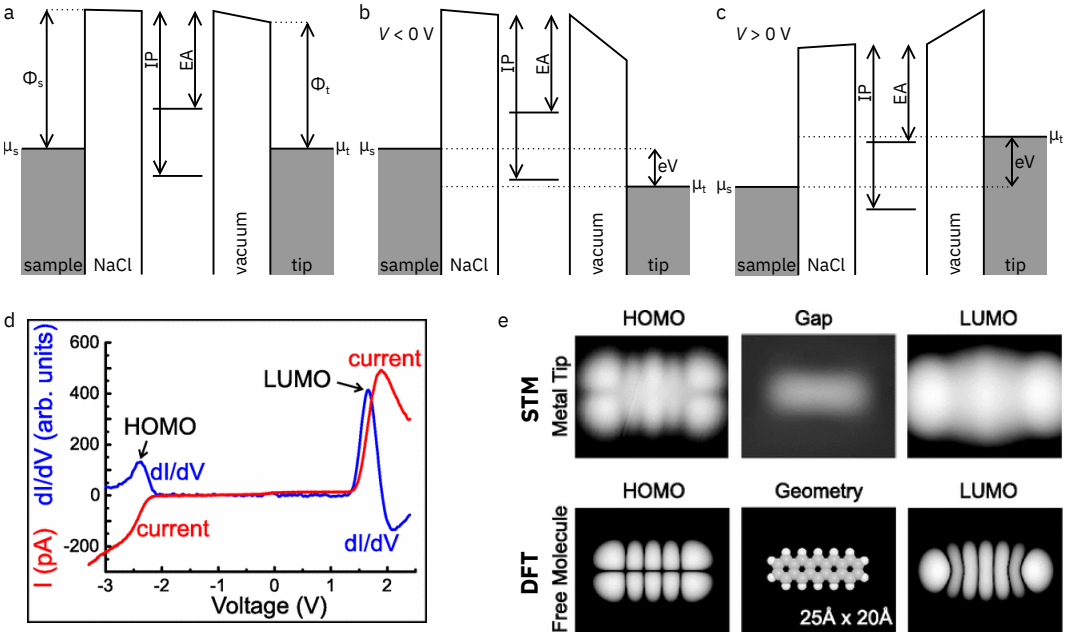


Figure 2.2: **STM and STS on molecules.** (a)–(c) Energy level diagrams of the double-barrier tunnel junction consisting of a metallic substrate (sample), a dielectric decoupling layer (NaCl), the adsorbed molecule, the vacuum barrier and the metallic tip. The alignment of the ion resonances of the molecule with respect to the sample states is determined by the molecule's ionization potential (IP) and electron affinity (EA) and the potential drop within the decoupling layer. In the depicted situation, the molecule is in its neutral charge state at zero applied bias voltage; the energy level of the anion lies above the electrochemical potentials of tip and sample (a). In (b), a negative sample bias voltage is applied such that electron transfer from the neutral molecule to the tip is allowed. In (c), a positive sample voltage is applied such that electron transfer from the tip to neutral molecule is allowed. (d) Differential conductance ($^{\mathrm{d}I}/_{\mathrm{d}V}$) and $I(V)$-curve with the STM tip positioned atop a pentacene molecule adsorbed on bilayer NaCl on Cu(111). The peaks in the differential conductance at positive and negative sample bias voltage correspond to the negative (NIR) and positive ion resonance (PIR), respectively. (e) STM images of pentacene at its PIR (left, HOMO) within the gap between NIR and PIR (center, Gap) and the NIR (right, LUMO) together with DFT simulations of the free molecule showing contours of constant orbital density ($|\psi|^2 = 5 \cdot 10^{-4}$ Å$^{-3}$). *(d) and (e) reproduced with permission from ref. [8]. Copyright (2005) American Physical Society.*

underlying substrate[40,42] or reorganization within the molecule. Upon changing the charge state the equilibrium geometry of the nuclei within the molecule and its surrounding will distort in order to minimize the free energy.[43,44] As a result, the EA of the neutral molecule is smaller than the IP of the anion by the so-called reorganization energy.[41,45] Depending on the level alignment with respect to $\mu_s$ and the amount of the reorganization energy upon charging this effect can lead to the stabilization of certain charge states on the surface.[46,47] Furthermore, charged and neutral molecules can be distinguished in STM. Many metallic surfaces, like Cu(111), exhibit a surface state close to $\mu_s$. This surface state survives as an interface state when the metal is (partially) covered with a thin insulating layer like NaCl.[48]

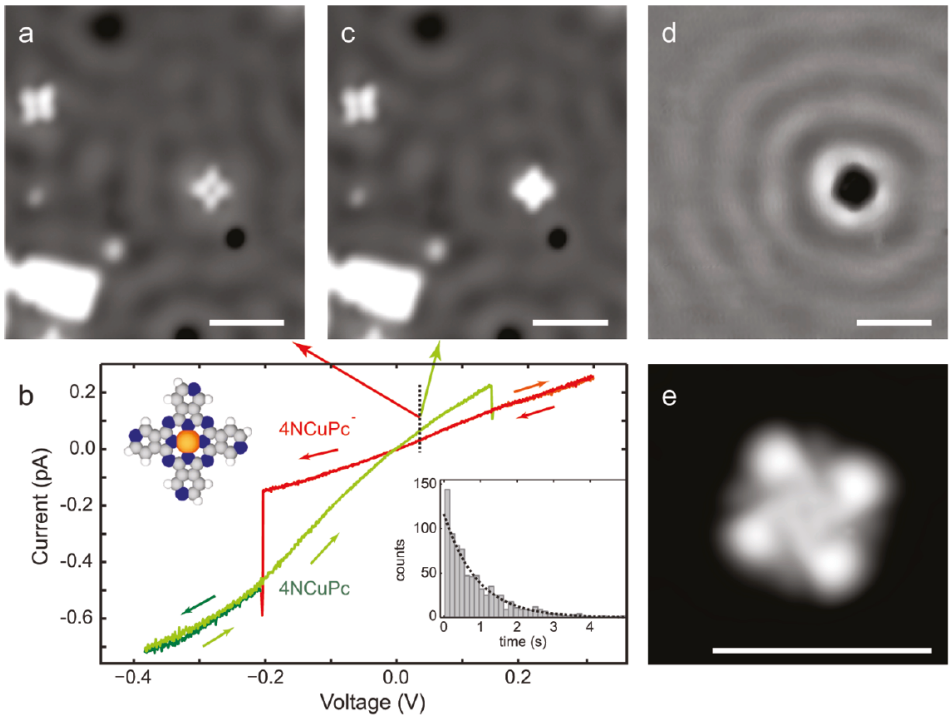


Figure 2.3: **STM images and spectrum of 4NCuPc molecules on NaCl/Cu(111).** (a) Image of two 4NCuPc molecules acquired at 20 mV and $I = 5$ pA (neutral charge state) (b) $I(V)$ spectrum acquired with the tip positioned above the center of a 4NCuPc molecule, showing hysteresis. The red and green curves indicate the two states involved in the switching process. Voltage sweep directions of decreasing and increasing bias are indicated by dark and light colors (and arrows in the corresponding colors), respectively. A model of a 4NCuPc molecule is given. Color coding: gray, C; blue, N; white, H; and orange, Cu. The inset shows a histogram of the observed switching times obtained at $V = 140$ mV and $I = 5$ pA. The dashed line shows an exponential fit of the data. (c) Image of the same molecules as in (a) but now with one molecule in the negative charge state ($V = 20$ mV, $I = 5$ pA) (d) Difference image constructed by subtracting image (c) from image (a) (after drift correction), demonstrating the effects of the manipulation. (e) Image of a 4NCuPc molecule adsorbed on NaCl/Cu(100) ($V = -750$ mV, $I = 2$ pA). *Reprinted with permission from ref. [47]. Copyright (2011) American Chemical Society.*

Deviations from an infinitely extended flat and homogeneous surface, such as step edges or adsorbates on the NaCl can act as scatterers of the two-dimensional gas of electrons (2DEG) in this interface state, resulting in a characteristic standing wave pattern that can be imaged in STM.[49,50] While the interaction between the 2DEG and neutral adsorbates is typically small, the electrostatic potential of charged adsorbates strongly influences the 2DEG in the interface state.[47,51] Thus, charged adsorbates act as scatterers that strongly affect the interference pattern of the interface state. Figure 2.3 shows an example of the effect of a charged adsorbate on the standing wave pattern of the interface state electrons (see also ref. [47]). 4NCuPc molecules exhibit a bistable charge state on bilayer NaCl on Cu(111): Upon charging, the NIR of the molecule shifts below $\mu_s$ and thus, within a certain bias voltage

range, the negative charge state is stabilized on the surface, which is visible in the hysteretic behavior of the $I(V)$-curve (Fig. 2.3b). Hence, the molecule can be prepared and imaged in two different charge states. Figure 2.3a shows the standing wave pattern of the interface state in the presence of two neutral 4NCuPc molecules. Upon charging the molecule on the right, the scattering pattern changes (Fig. 2.3c). The difference image of Fig. 2.3a and c, shown in Fig. 2.3d, supports the conjecture that the charged molecule acts as a scattering center for the interface state electrons. In addition, positive and negative charge states can be differentiated: Positively charged scattering centers induce interface state localization due to their attractive potential, which is not present for negatively charged adsorbates.[40]

## Chapter 3

# Non-contact atomic force microscopy

Since STM relies on the tunnel current as measurand it is limited to (semi-)conducting surfaces. This led Binnig, Quate and Gerber to devise a more generally applicable approach for surface characterization based on measuring the forces acting between a sharp tip and a sample in close proximity. The tip is attached to a flexible cantilever that acts as a force sensor. This system, consisting of the cantilever with attached tip and the sample, can be described by a coupled oscillator model as shown in Fig. 3.1a.
In its first realization the AFM consisted of a tip that was attached to a soft leaf spring. As the tip is scanned over the sample the leaf spring gets deflected because of forces acting on the tip, according to Hooke's law $F = -k \cdot \Delta z$. The deflection was detected *via* an STM junction consisting of a metallic tip and the leaf spring. Since the tunnel current varies exponentially with the distance between both electrodes this allows measuring the deflection with very high precision.[2]
However, in this static mode the junction is mechanically unstable. Because of attractive forces between tip and sample[52] and the soft cantilever the tip tends to snap into the sample, a phenomenon known as 'jump-to-contact'. This can be circumvented by oscillating the cantilever perpendicular to the surface. At the lower turning point a jump-to-contact can be prevented because of the restoring force of the cantilever as long as

$$k_0 \cdot A \geq |F_{ts}^{max}| \qquad \text{(stability criterion)} \tag{3.1}$$

with the spring constant of the unperturbed cantilever-tip system $k_0$, the oscillation amplitude $A$ and the maximum attractive force between tip and sample $F_{ts}^{max}$.[53,54]
The equation of motion of the coupled oscillator system shown in Fig. 3.1 is given by

$$m\ddot{z} = -(k_0 + k_{ts})z, \tag{3.2}$$

with $k_{ts} = -\frac{\partial F_{ts}}{\partial z}$. With the ansatz $z = A \cdot \cos(2\pi f t + \varphi)$ one finds that the resonance frequency is given by

$$f = \frac{1}{2\pi}\sqrt{\frac{k_0 + k_{ts}}{m}} \tag{3.3}$$

and thus directly depends on the interaction potential between tip and sample $V_{ts}$ with $k_{ts} = \frac{\partial^2 V_{ts}}{\partial z^2}$. Figure 3.1b illustrates the effect of variations in the interaction potential between tip and sample: The schematic resonance curve of the unperturbed cantilever-tip system, *i.e.*, without tip-sample interaction, with corresponding resonance frequency $f_0$ shifts upon a change in tip-sample interaction. Figure 3.1b additionally illustrates the two modes of operation in dynamic AFM. In the first mode, called amplitude-modulation AFM (AM-AFM), the cantilever is excited at a constant frequency close to $f_0$ and the change in amplitude upon detuning of the resonance curve $\Delta A$ is recorded.[58] In the second mode, frequency-modulation AFM (FM-AFM), the cantilever is always driven at its resonance frequency to oscillate at a constant oscillation amplitude and the change in resonance frequency

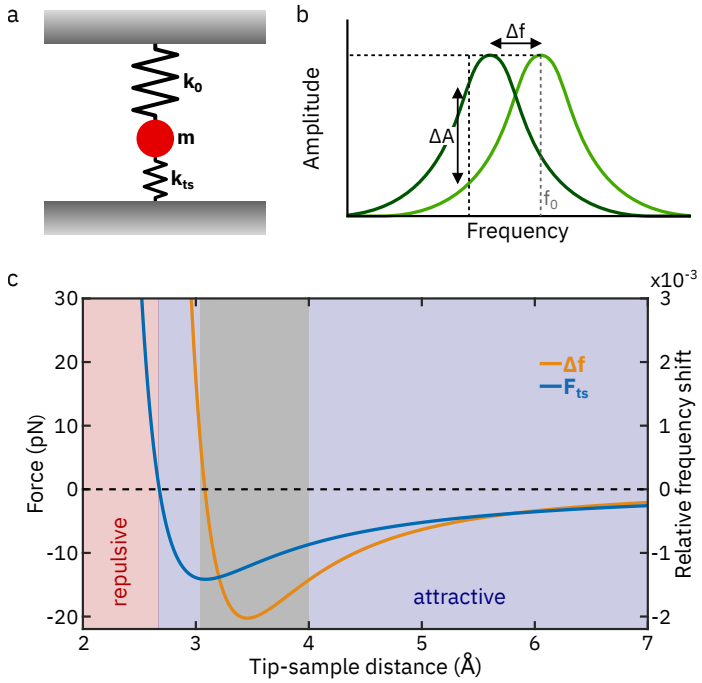


Figure 3.1: **Functional principles of AFM.** (a) Coupled oscillator model representing the interacting system of cantilever, tip and sample. The tip is represented by its effective mass $m$, the spring constant of the cantilever is given by $k_0$, and $k_{ts}$ denotes the coupling between the tip and the sample. (b) Resonance curves of the coupled oscillator system depicted in (a) with (dark green) and without (light green) tip-sample interaction. The resonance frequency of the unperturbed system (without tip-sample interaction, *i.e.*, $k_{ts} = 0$) is given by $f_0$. The change in resonance frequency upon introducing tip-sample coupling depends on $k_{ts}$. At constant frequency a change in tip-sample interaction results in a change in amplitude $\Delta A$ and at constant amplitude the frequency shifts by $\Delta f$. (c) Distance dependence of the total force acting between tip and sample $F_{ts}$ (blue) and the corresponding relative frequency shift $\frac{\Delta f}{f_0}$ (orange) calculated from the force gradient using Equation 3.7. The parameters used for the calculations are: $A_H = 2.5$ eV, $R = 30$ nm, $E_{bond} = 2$ eV, $z_{min} = 3$ Å and $k_0 = 1800$ Nm$^{-1}$ (see also refs. [55–57]). The repulsive and attractive regime of the total force are highlighted in red and blue respectively. The gray shaded area corresponds to typical tip-sample distances in nc-AFM measurements in this thesis.

$\Delta f$ is recorded.[3] The minimum detectable force in both FM- and AM-AFM is given by

$$\delta F_{ts}^{min} = \sqrt{\frac{2k_0 k_B T B}{\pi f_0 Q A^2}} \tag{3.4}$$

with bandwidth $B$, quality-factor of the cantilever $Q$ and oscillation amplitude $A$. In UHV applications, however, FM-AFM is almost exclusively used.[3] Thus, the further description of dynamic AFM will be limited to FM-AFM.

The frequency shift is given by

$$\Delta f = f - f_0 \tag{3.5}$$

$$= -\frac{f_0}{k_0 A^2}\langle F_{ts} A\cos(2\pi f_0 t)\rangle, \tag{3.6}$$

averaged over the full oscillation cycle. In the limit of small oscillation amplitudes and for $k_{ts} \ll k_0$, this expression simplifies to

$$\Delta f \approx -\frac{f_0}{2k_0}\frac{\partial F_{ts}}{\partial z}. \tag{3.7}$$

The total force acting between tip and sample is a sum of different force components with different distance dependencies. In UHV applications, the following contributions to the total tip-sample force are relevant:

**Van der Waals force** Forces stemming from the interactions of local dipole moments are summarized as van der Waals (vdW) force. It consists of the Keesom force between permanent dipoles, the Debye force between permanent and induced dipoles and the London dispersion force between instantaneous dipoles. The latter is always attractive and typically the dominant contribution to the overall vdW force. Following the approach by Hamaker for a spherical tip with radius $R$ at distance $z$ from a flat surface,[52,59] the vdW force is given by

$$F_{vdW} = -\frac{A_H R}{6z^2} \tag{3.8}$$

with the Hamaker constant $A_H$. The vdW force does not vary significantly on the atomic scale and is therefore considered a long-range interaction.

**Electrostatic force** The conductive tip and sample can be described as a capacitor with a distance-dependent capacitance. The electrostatic force acting between them is long-ranged, always attractive and given as

$$F_{el} = \frac{1}{2}\frac{\partial C}{\partial z}(V - V^*)^2 \tag{3.9}$$

with the contact potential difference $V^* = \frac{(\phi_s - \phi_t)}{e}$.

**Pauli repulsive force** For tip-sample distances that are on the order of the next-neighbor distance $z_{min}$, electron wave functions of tip and sample start to overlap significantly. This leads to a short-range repulsive force between tip and sample because of the Pauli exclusion principle. The interplay between the attractive vdW force component and the repulsive force component stemming from Pauli repulsion can be described by a Lennard-Jones (LJ) pair potential with the binding energy $E_{bond}$:[53]

$$F_{LJ} = 12\frac{E_{bond}}{z_{min}}\left[\underbrace{\left(\frac{z_{min}}{z}\right)^{13}}_{\text{Pauli repulsion}} - \underbrace{\left(\frac{z_{min}}{z}\right)^{7}}_{\text{vdW}}\right]. \tag{3.10}$$

The total force (neglecting the electrostatic force) is plotted in Fig. 3.1c with typical parameters,[55–57] together with the corresponding relative frequency shift using Equation 3.7.

## High-resolution AFM on single molecules

Of the three forces contributing to the total tip-sample interaction, only the Pauli repulsive force yields atomic contrast in AFM. Hence, to obtain atomically resolved AFM images the distance between tip and sample needs to be very small (typically around 3–4 Å), which roughly corresponds to region of the maximum attractive force between tip and sample. When working with metal-terminated tips on single molecules, this can lead to stability problems; since metal-terminated tips are typically highly reactive, molecules can be displaced or picked up easily while scanning at small tip-sample distances. The key to achieving atomic resolution in AFM on single molecules is to functionalize the tip, *i.e.*, to deliberately change the termination of the tip, and thereby make it more chemically inert. In this way, tip-sample distances in which the repulsive force contribution can be probed can be achieved without picking up the molecule.[5] Moreover, the tip functionalization will affect the contrast and resolution in AFM images because of several factors:[55] (i) The size of the tip will influence the achievable lateral resolution, *i.e.*, the smaller the tip radius the higher the lateral resolution that can be achieved. (ii) The charge distribution of the tip apex affects the electrostatic force component and thus the AFM contrast.[61] (iii) As a consequence of the forces acting between tip and sample, relaxations of the apex atoms can occur. This can lead to

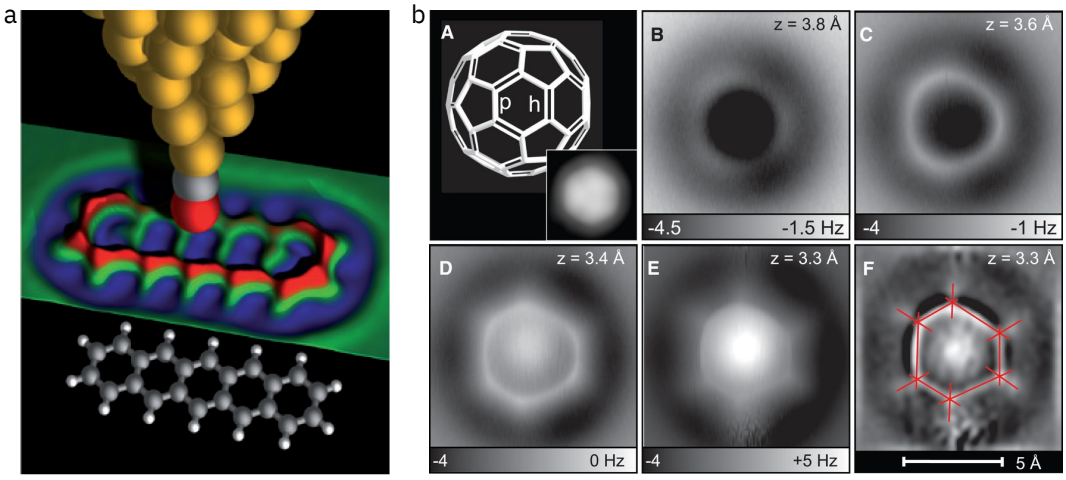


Figure 3.2: **High-resolution AFM on single molecules with CO-functionalized tips.** (a) Model of a CO-functionalized tip above a pentacene molecule. The measured AFM data is shown as a color-coded map ($\Delta f = -7$ Hz (blue) to $-2$ Hz (red); oscillation amplitude $A = 0.2$ Å; measurement data taken from ref. [5]). *Reused with permission from ref. [60]. Copyright (2011) Springer Nature.* (b) Measurements on $C_{60}$. (**A**) $C_{60}$ model. The bonds fusing a pentagon and a hexagon (p) are of smaller bond order compared with the bonds fusing two hexagons (h). (Inset) STM image (sample bias $V = 0.2$ V, current $I = 2$ pA, size 24 by 24 Å$^2$). The molecule and tip are identical to those in (**B**) to (**F**). (B to E) AFM measurements showing $\Delta f$ at different tip heights $z$ above $C_{60}$/Cu(111) using a CO-functionalized tip. Image size 10 by 10 Å$^2$, oscillation amplitude $A = 0.36$ Å, $V = 0$ V. (F) Laplace-filtered and flattened image of (E), used to measure the apparent bond length. *Reused with permission from ref. [6]. Copyright (2012) American Association for the Advancement of Science.*

image artifacts but can also enhance the achievable lateral resolution.[6,61–63] The dominant contribution to the AFM contrast stems from the tip functionalization.[56] It is therefore beneficial for the interpretation of AFM images to use a well-defined tip. The list of potential tip functionalizations in AFM ranges from single atoms like metal, halogen or noble gas atoms[13,64–66] over diatomic molecules like carbon monoxide (CO) or nitric oxide (NO)[5,14,64] to aromatic molecules like pentacene or $C_{60}$.[5,67] The most widely used tip-functionalization in high-resolution AFM is single CO-molecules.

As stated earlier, the atomic-scale contrast in high-resolution AFM stems from the repulsive force contribution between tip and sample due to the Pauli exclusion principle. Thus, AFM is sensitive to the electron density at the position of the tip, which is largest atop atoms and bonds with non-vanishing electron density (*i.e.*, bonds with covalent character)[56] as shown in Fig. 3.2a (see also ref. [60]). This makes it feasible to, for example, distinguish bonds with different electron densities, *i.e.*, different bond order. The concept of Pauling bond order is important in organic chemistry to characterize certain properties of covalently bonded molecules, like aromaticity and stability. The higher the bond order the higher the electron density and the shorter the bond length.[68,69] Figure 3.2b (**B**-**C**) shows AFM images acquired on an individual $C_{60}$ molecule at different tip-sample distances. The differences in bond length of the $p$ and $h$ bonds indicated in the structure model in Fig. 3.2b, **A** are visible in all AFM images. In addition, the $h$ bonds appear brighter, indicating their higher bond order. However, the apparent bond lengths measured in AFM are often significantly larger compared to the real values. This relates to relaxations of the CO at the apex, which is repelled from regions of high electron density, leading to an apparent elongation as well as sharpening of the imaged bonds.[6,62,70,71] This effect is most pronounced atop bonds with small bond order, such that differences in bond length are typically amplified in AFM.[6]

In addition to bond order analysis, differences in adsorption geometry within a molecule are accessible with AFM. The frequency shift at a given position and tip-sample distance depends on the local tip-sample interaction. As a consequence, depending on the probed chemical species and the corresponding adsorption height (*i.e.*, distance between tip and molecule within a plane that is parallel to the surface), the $\Delta f(z)$-curve (shown in Fig. 3.1c for the unperturbed case) will change as a function of lateral position atop a molecule. For chemically identical species this change is directly tied to differences in adsorption height and can be quantified by determining the tip-sample distance that corresponds to the minimum in the $\Delta f(z)$-curves.[65,72] Since the position of the minimum also depends on the probed chemical species, macroscopic tip shape and applied bias voltage, this method is best suited to determine adsorption height differences. However, through gauging on a molecule with known adsorption height and measuring at a bias voltage corresponding to the local contact potential difference (compensated bias), these effects can be minimized such that absolute adsorption height measurements are feasible with a larger systematical error compared to measurements of adsorption height differences within one molecule.

Chapter 4

# Scanning tunneling microscopy induced luminescence

The first observation of light emission from the tunnel junction in an STM has been reported in 1988 by Gimzewski and co-workers.[73] Already then the potential of STM-induced light emission to serve as a highly localized light source in luminescence and fluorescence experiments has been anticipated. In combination with the ability of SPM-based techniques to achieve atomic resolution, this opens the way to investigate optoelectronic properties, for example of single molecules. However, first attempts to investigate molecules adsorbed on clean metallic surfaces did not show molecular luminescence.[26,74–76] This is owing to the fact that, on a metallic surface, light emission is strongly quenched because of interactions between the oscillating dipole in the molecule and its image dipole in the metallic substrate.[27,77] The problem of luminescence quenching can be circumvented, though, by introducing an ultra-thin insulating spacer layer between molecule and metal.[27] An ultra-thin insulating film reduces the interaction between metallic substrate and adsorbed molecules considerably, while still maintaining a sufficiently high conductivity through the tip-sample junction to allow for stable tunneling conditions in STM.[27,77,78]
For the formation of molecular excitons in scanning tunneling microscopy induced luminescence (STML), two different pathways are usually discussed.[27,78–83] They rely either on the transient charging of the molecule from the tip and subsequent charge transfer from the substrate to the molecule (Fig. 4.1) or (plasmon-mediated) energy transfer from inelastically tunneling electrons to the molecule (Fig. 4.2).

## 4.1 Charge-transfer mediated excitation

The basic principle of the charge-transfer mediated excitation mechanism is depicted in Fig. 4.1, here shown for negative polarity of the sample bias voltage. The electronic states of the molecule are denoted as $|n, S_m\rangle$ with the number of electrons in the molecule $n$ and the electronic state of the molecule $S_m$. The number of electrons in the neutral molecule is given as $N$.
Upon applying a sufficiently high bias voltage between tip and sample, charge transfer from the $|N, S_0\rangle$ state, *i.e.*, the ground state of the neutral molecule to the tip can occur, resulting in the formation of the cation $|N-1, D_0\rangle$ (see Fig. 4.1a and b). Depending on the alignment of the ion resonances of the cation and the sample states, subsequent charge transfer from the substrate to the molecule leads to a transition either into the ground state $|N, S_0\rangle$ or an excited state of the molecule, *e.g.*, $|N, S_1\rangle$ (Fig. 4.1b and c)[a]. The latter corresponds to the formation of a molecular exciton. Because of the smaller barrier height, the formation of the $|N, S_1\rangle$ state upon electron transfer to the $|N-1, D_0\rangle$ state is favored over the formation

[a] Since the yield for radiative triplet-singlet transitions is low compared to singlet-singlet transitions[85] triplet states are neglected in the following.

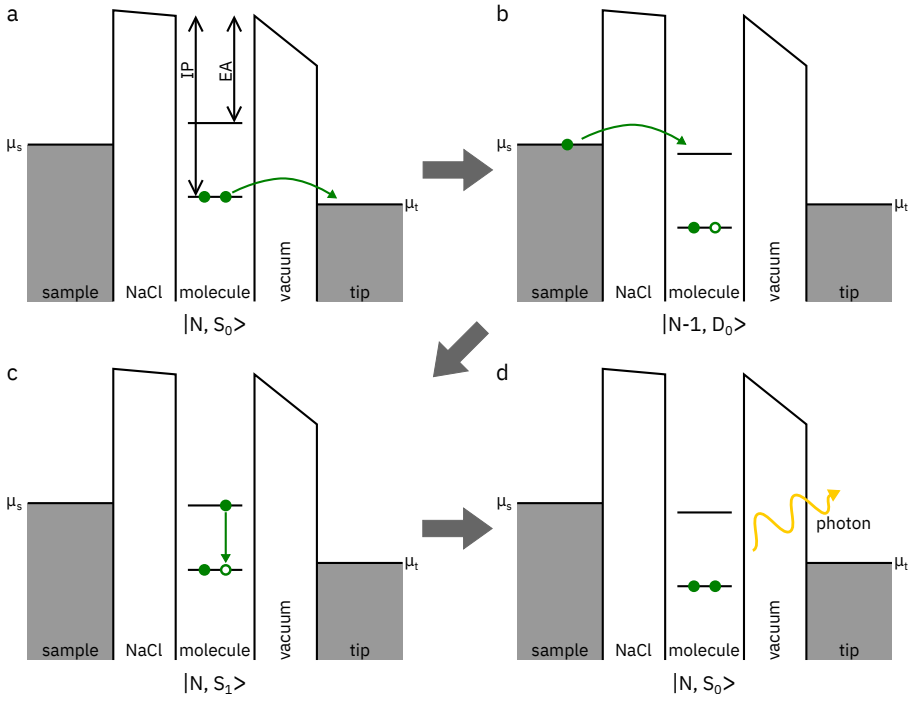


Figure 4.1: **Charge-transfer mediated excitation.** Schematics of the excitation mechanism for a single molecule in the STM-induced light emission process. Molecular electronic states are indicated as $|n, S_m\rangle$, where $n$ and $S_m$ denote the number of electrons in the molecule and the electronic state of the molecule, respectively. The excitation mechanism consists of a set of electron transfer transitions as follows: (a) from the ground state of the neutral molecule $|N, S_0\rangle$ to (b) the ground state of the cation $|N-1, D_0\rangle$ (doublet) to (c) the first excited singlet state of the neutral molecule $|N, S_1\rangle$ and (d) back to the ground state of the neutral molecule $|N, S_0\rangle$ with emission of a photon. In (a) and (b), horizontal lines represent the ionization potential (IP) and electron affinity (EA) for each electronic state. Green and white dots denote electrons and holes, respectively. *Adopted and modified with permission from ref. [84]. Copyright (2019) American Chemical Society.*

of the ground state. Note that this barrier height argument prefers the formation of the ground state over the excited state in the case of the path over the anion at positive sample bias voltage. Figure 4.1c to d shows the transition from the $|N, S_1\rangle$ state into the ground state upon emission of a photon.

## 4.2 Plasmon-mediated energy transfer

In the vicinity of a metal-dielectric interface, excitations of the conduction electrons in the metal can couple to the electric field in the dielectric.[86] The interaction between these coupled excitations and excitons in STML can be described by an energy transfer *via* so-called plasmon polaritons localized in the tip-sample junction, *i.e.*, nanocavity plasmons (NCPs).[80,87]

**Nanocavity plasmons**

The optical properties of a metal (being its response to an electromagnetic field) can be described by the collective motion of the conduction electrons for a wide range of frequencies. If a bulk metal is excited at a certain frequency, the sea of conduction electrons will start oscillating against the background of fixed positive ion cores. The quanta of this collective oscillation are called plasmons and the corresponding resonance frequency plasma frequency $\omega_p$. In the vicinity of an interface to a dielectric , *e.g.*, vacuum, the electron plasma in the conductor can couple to the electromagnetic field in the dielectric (plasmon polariton). On extended and flat surfaces, plasmon polaritons cannot couple to photons because of a mismatch in their dispersion relations, hence, simultaneous conservation of energy and momentum is not possible.[86] In conducting nanostructures, as in the sharp apex of a metallic SPM tip, however, the translational invariance parallel to the surface is broken, plasmon polaritons can couple to photons, *i.e.*, they can be excited *via* illumination and decay radiatively.[88,89] In the presence of a metallic surface, the coupling of the nanostructure's dipole and the image dipole in the surface leads to a highly localized enhancement between plasmonic nanoparticle and surface,[90–92] referred to as nanocavity plasmon (NCP). For a nanoscopic SPM tip in close proximity ($\approx$ nm) to the sample surface, the NCP is localized within a radius of a few nanometers below the tip apex.[81,93]

In STM, fluctuations in the tunnel current can cause oscillations of the conduction electrons in tip and sample, either *via* inelastic tunneling or hot charge carriers, leading to an ex-

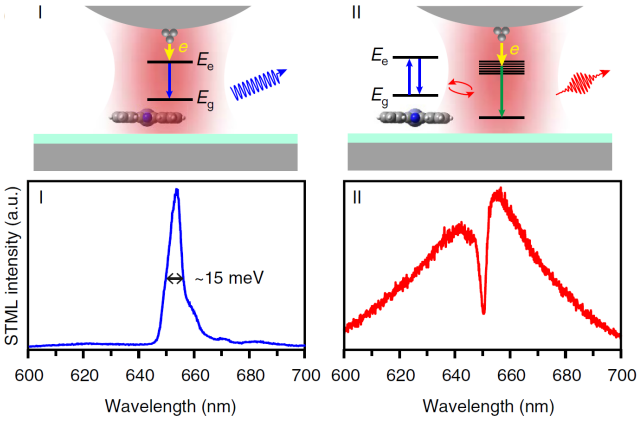


Figure 4.2: **Single-molecule luminescence in STML.** Two different junction structures on monolayer NaCl on Ag(100) with an adsorbed ZnPc molecule (top schematics) and corresponding STML spectra (bottom, −2.5 V, 200 pA, 20 s). Situation I: Charge-injection mediated exciton formation. A consecutive charge transfer from tip and substrate to the molecule allows the formation of the first excited singlet state (exciton). Situation II: Plasmon-mediated exciton formation. Energy transfer from inelastically tunneling electrons to the molecule *via* nanocavity plasmons (NCP) fosters the formation of molecular excitons. The NCP-exciton coupling strength depends on the energetic positions of the NCP resonance and molecular exciton energy with respect to each other. A typical Fano lineshape is observed due to the interaction between the NCP and the two-level emitter in close proximity. *Adopted and modified with permission from ref. [94]. Copyright (2017) Springer Nature.*

citation of NCPs.[90,91,95,96] They can be detected through their radiative decay exhibiting a broad resonance with a cutoff that is typically given by the applied bias voltage[b].[88,100] The resonance frequency depends on the dielectric properties of tip and sample as well as tip-sample distance and geometry of the tip.[89,91,101,102] The intensity of the radiative decay of NCPs in STM is found to increase linearly with the tunnel current, suggesting a dominant contribution of single-electron processes in their excitation.[98,103]

**Plasmon-exciton coupling**

NCPs were found to play a vital role in STML on single molecules, since they can couple to molecular excitons.[80,81,87,94,104–106] This is visible for example in the NCP spectrum shown in Fig. 4.2 Situation II: In the proximity of a molecule that can be excited in STML the NCP spectrum exhibits a dip at the energetic position of the molecular exciton.[81,94] The coupling can lead to the excitation of molecules from $S^0$ to $S^1$ by an energy transfer from inelastically tunneling electrons *via* the NCP. However, this excitation mechanism is typically expected to play a minor role compared to a charge-transfer mediated excitation, since it requires the coupling between inelastically tunneling electrons and NCP as well as between NCP and molecular exciton.[84,94,107,108] Nevertheless, as they provide a high density of radiative modes in the vicinity of the molecule, the radiative decay of the molecular exciton can be strongly enhanced as a consequence of the Purcell effect.[82,109]

[b] Multi-electron excitation processes can occur, shifting the cutoff to multiples of the applied bias voltage.[97,98] However, these processes occur with a considerably lower yield compared with the single-electron process and are therefore neglected in the following. Depending on the tip-material, the cutoff can also be given by interband transitions.[99]

# Part II

# Experimental setup and Methods

## Chapter 5

# Measurement system

All experiments presented in this thesis were performed with a low-temperature combined STM/AFM operated under ultra-high vacuum (UHV) conditions. The system was designed by Gerhard Meyer[110] and is, in a modified version, commercially available (CreaTec Fischer & Co. GmbH[111]). This chapter introduces the STM/AFM system as well as the methods used for preparation of tip and sample.

## 5.1 Combined STM/AFM system

The STM/AFM system is shown in Fig. 5.1a. The UHV chamber consists of two parts, *i.e.*, the preparation chamber and the chamber with the low-temperature scanning probe stage, which are separated by a gate valve. The preparation chamber is used for sample preparation and storage. It is equipped with a titanium sublimation pump and an ion getter pump, a sputter gun and heatable crucibles serving as effusion evaporators typically used for the thin-film preparation. The typically achieved base pressure is on the order of $p \approx 10^{-10}$ mbar. The metal samples are mounted onto small resistive button heaters on the sample holders and a thermocouple is attached for controlling the temperature. The manipulator is used to move samples and can be positioned in all three directions as well as rotated along its longitudinal axis. It can be cooled with liquid nitrogen ($\mathrm{lN_2}$) or liquid helium (lHe) and is electrically contacted for annealing. The preparation chamber is connected to a small loadlock chamber that is equipped with a turbomolecular pump and is used to transfer samples into and out of the vacuum chamber, *via* a gate valve.
The microscope stage is based on the beetle type introduced by K. Besocke.[112,113] Scanning and coarse motion of the sensor across the sample in $xy$-direction as well as motion along $z$ (approach/retract) is achieved using three piezo tubes that are each divided into four separately actuatable segments. The sensor is attached to a small central piezo tube that drives the tip oscillation. For vibration isolation, the microscope is suspended on three springs and equipped with an eddy current damping system. The STM/AFM is cooled *via* a bath cryostat consisting of a lHe tank that is enclosed by an $\mathrm{lN_2}$ tank and two radiation shields, each thermally connected to one of the tanks. The microscope is thermally coupled to the liquid helium tank such that it can be operated at a temperature of $T \approx 5$ K.
The microscope has optical access *via* windows in the radiation shields. One of them hosts a biconvex lens that allows the collection of photons emitted from the tip-sample junction in a solid angle of $\Omega \approx 0.03$. This optical access was used for conducting the STML experiments presented in chapter 10. To that end, a fiber optic cable is positioned in the focal point $f_2$ of the lens outside the UHV chamber and connected to a spectrograph (Acton SP-300i, Princeton Instruments) with attached $\mathrm{lN_2}$-cooled CCD camera (PyLoN, Princeton Instruments) with a minimal spectral resolution of $\delta\lambda \approx 0.2$ nm. For positioning of the fiber optic it is mounted to a 2D translation stage with micrometer screws. The tunnel current and voltage are increased (typically $V \approx -2.5$ V, $I = 1$ $\mu$A) such that photon emission from the junction is visible by eye through an ocular that is attached to the chamber and the fiber

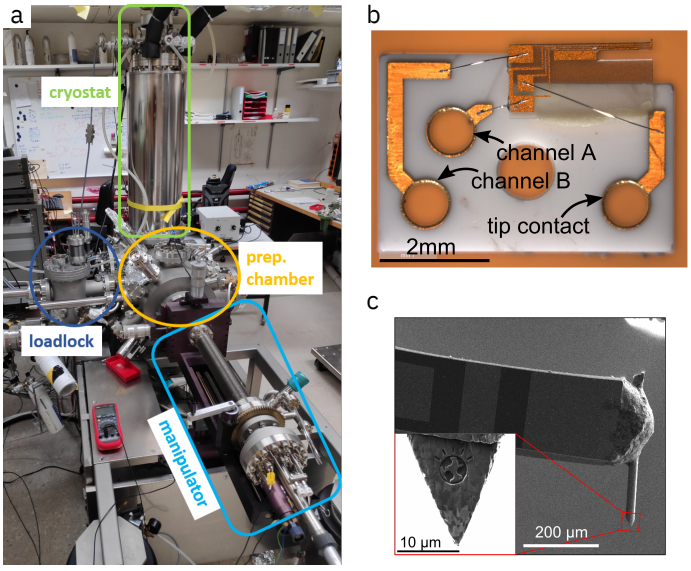


Figure 5.1: **STM/AFM system and qPlus sensor.** (a) Photograph of the combined STM/AFM system with the main components highlighted: The cryostat (green) with the microscope attached to it, the preparation chamber (orange), the manipulator (light blue) and the loadlock (dark blue). (b) Photograph of a qPlus force sensor with electrodes for deflection sensing as well as contacting the conductive tip. (c) Scanning electron microscopy image of the free prong of the sensor with a PtIr tip attached. The inset shows a scanning electron microscopy image of the tip apex with the IBM Smarter-Planet icon engraved. *(b) and (c) reprinted with permission from ref. [114]. Copyright (2016) IBM Research.*

optic is positioned such that the total intensity on the CCD is maximized.

The STM/AFM is controlled *via* homebuilt electronics and a customized software. The piezos are actuated *via* a high-voltage amplifier. Tunnel current and deflection signal are amplified by two operational amplifiers with gain $10^{10}$ and $10^8$, respectively, located on the $lN_2$ shield. The deflection signal is additionally amplified by an external amplifier (Stanford Research Systems SR560) with gain 20. For the tunnel current, an additional variable gain amplifier that can be operated at higher currents and higher bandwidth is available. The analog components of the electronics are connected to a digital signal processor comprising, *i.a.*, the $z$ feedback.
A scheme for the FM-AFM feedback is depicted in Fig. 5.2. The oscillation of the sensor produces a current that is converted into a voltage (deflection signal). The bandpassed deflection signal is fed into a phase-locked loop (PLL) that generates a signal that is proportional to the frequency shift $\Delta f$. This signal can also be used in a $z$ feedback, which allows constant-frequency shift imaging. The automated gain control (AGC) constitutes the amplitude feedback. Its phase-shifted output signal is used to adjust the gain for driving the oscillation. In addition, the tunnel current upon applying a bias voltage between tip and sample can be measured.
The tip is held at virtual ground, *i.e.*, bias voltages given in this thesis always refer to sample bias voltage.

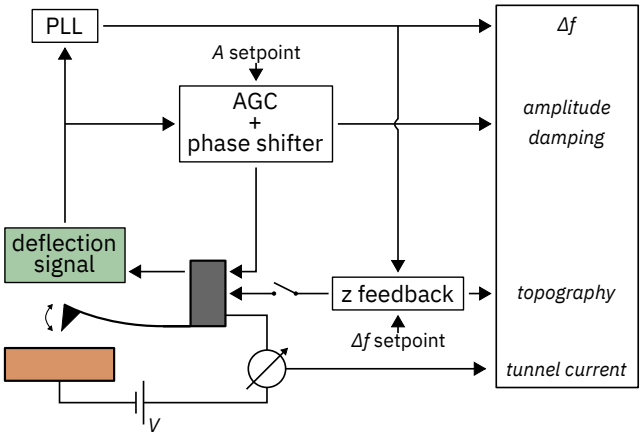


Figure 5.2: **Feedback scheme for FM-AFM.** The most important components as well as the output and input signals are depicted. The (bandpassed) deflection signal is fed into a phase-locked loop (PLL) that outputs a voltage that is proportional to the frequency shift $\Delta f$. $\Delta f$ is forwarded to the $z$ feedback, which can be either switched on (constant-frequency shift mode) or off (constant-height mode). In addition, the deflection signal is fed into an automated gain control (AGC), which is a closed-loop feedback circuit adjusting the gain for driving the oscillation in order to maintain a constant oscillation amplitude $A$. It outputs the oscillation amplitude as well as the damping. *Adapted from ref. [57].*

## 5.2 qPlus sensor

The microscope is equipped with a qPlus sensor of the third generation, invented by F. J. Giessibl[4,115] with a spring constant of $k_0 \approx 1800$ Nm$^{-1}$, oscillation frequency $f_0 \approx 32$ kHz and a $Q$-factor on the order of about 100000 at $T = 5$ K. It consists of a quartz cantilever that is glued onto a ceramic substrate. A PtIr wire is glued to the free prong and serves as STM/AFM tip, as shown in Fig. 5.1 on the right. Due to the piezoelectricity of quartz, the mechanical oscillation of the tuning fork is translated into an electrical signal such that no additional detection scheme is necessary. The sensor is connected *via* electrodes that are used for deflection sensing as well as measuring of the tunnel current. To minimize crosstalk between the AFM and STM signals, the current electrode is positioned in the center of the beam. A photo of a qPlus sensor is shown in Fig. 5.1b. The sensor is glued onto a MACOR tip holder and excited mechanically by the central piezo tube. As a consequence of the high spring constant, the qPlus sensor can be operated with sub-Ångström oscillation amplitudes (see Equation 3.1). Unless stated otherwise, the oscillation amplitude was set to $A = 0.5$ Å.

## 5.3 Tip-sample system

As tip a PtIr wire with a diameter of 25 $\mu$m was used, which was glued to the free prong of the qPlus sensor. The tip was sharpened using a focused ion beam (FIB) (a scanning electron microscopy image of the tip is shown in Fig. 5.1c) followed by *in situ* indentation into the bare metal surface of the sample inside the STM/AFM. The general sample system that was used in this thesis was a metallic substrate that was partially covered with a thin dielectric film. As metallic substrate either a Cu(111) or Ag(111) single crystal was used,

which was cleaned *in situ* by repeated sputtering and annealing cycles. As a decoupling layer we typically used NaCl that was sublimed onto the clean metal at a fixed temperature yielding a partial coverage of two to four layers of (100) oriented NaCl, depending on the experimental requirements.[48,116] For some of the measurements presented in chapter 9, a thin layer of Xe instead of NaCl was deposited onto the clean Cu(111) surface held at $T \approx 15$ K inside the microscope. To that end, gaseous Xe was allowed into the preparation chamber up to a partial pressure of $2 \cdot 10^{-5}$ mbar and the shutter to the microscope was opened for 35 s.[21]

A sub-monolayer coverage of well-dispersed molecules on the sample surface was achieved by thermal sublimation onto the sample held at $T \approx 10$ K. To that end, a small amount of molecules was deposited onto a Si-wafer that was subsequently transferred into the preparation chamber and positioned in front of a small opening in the shutter to the microscope. The wafer was then flash-annealed to approximately 900 K *via* resistive heating[a], facilitating diffusion of the molecules to an energetically favorable lattice site upon adsorption while preventing long-range diffusion and cluster formation.

Unless stated otherwise, single CO molecules were used for tip-functionalization. To that end, gaseous CO was allowed into the preparation chamber up to a partial pressure of $p \approx 5 \cdot 10^{-8}$ mbar and the shutter to the microscope was opened for 20 s. To pick up a CO (typically from bilayer NaCl), the bias voltage was decreased and the metallic tip approached to a CO molecule adsorbed on the surface.[14] An STM overview of a typical sample surface after preparation is shown in Fig. 5.3.

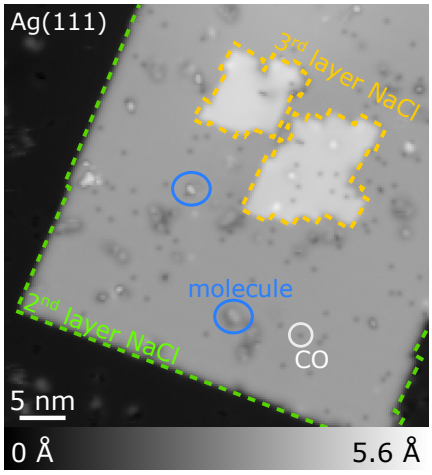


Figure 5.3: **Constant-current STM overview of a typical sample surface after preparation.** The area marked by the green dashed line is a bilayer NaCl island on a Ag(111) surface, the yellow dashed line indicates regions with third layer NaCl patches. The adsorbed CO molecules used for tip functionalization appear as small circular depressions (white circle), adsorbed molecules as protrusions that are, in some cases, surrounded by a dark halo (blue circles).

[a] Fast heating can favor sublimation of the molecules over decomposition.[117,118]

## Chapter 6

# Modes of data acquisition

Depending on the properties that are investigated, different data acquisition modes can be utilized. This chapter introduces the ones that were used to obtain the experimental results presented in this thesis.

## Imaging

In SPM there are many possible imaging modes. In this thesis two imaging modes were typically used: First, an active $z$ feedback loop adjusts the distance between tip and sample such that the measured signal is held constant. In the combined STM/AFM setup the signal used for the $z$ feedback can either be the current, *i.e.*, the microscope is operated in constant-current mode, or the frequency shift $\Delta f$, *i.e.*, constant-frequency shift mode. In constant-current mode, the recorded images show contours of constant LDOS along which the tip was scanned, according to Equation 2.5. In constant-frequency shift mode, the recorded images show contours of constant gradient of the tip-sample force along the direction of oscillation, see Equation 3.7. Second, the $z$ feedback loop controlling the tip-sample distance is switched off, such that the tip is scanned across the sample at a constant height, *i.e.*, constant-height mode. The recorded images then show the tunnel current and/or frequency shift as a function of tip-position in a defined plane above the sample surface.

## Spectroscopy

Recording the measurement signal as a function of certain applied parameters, like bias voltage or tip-sample distance, in SPM is typically referred to as spectroscopy. Depending on the type of spectroscopy that is utilized, different properties of the sample that are not accessible by imaging can be deduced.

**Scanning tunneling spectroscopy (STS)** In STS, the change in tunnel current upon applying an alternating bias voltage is recorded as a function of bias voltage using lock-in detection to obtain the differential conductance as a function of applied bias voltage. According to Equation 2.5, this allows inferences on the sample's LDOS.

**Force-distance spectroscopy** The tip-height dependence of the tip-sample interaction can be probed by recording the frequency shift as a function of tip-height offset $\Delta f(z)$. This can be either used to obtain the total vertical force component $F_{ts,z}$ by numerical integration using the method of Sader and Jarvis,[119] or to determine differences in adsorption geometry of adsorbates.[65]

**Optical spectroscopy** STML point-spectra are recorded by positioning the tip atop the position of interest with enabled feedback. Typically, bias voltages on the order of

$2 - 3$ V and tunnel currents on the order of $100 - 400$ pA are applied. The integrated photon intensity over a set integration time as a function of wavelength is recorded using the LightField data acquisition software by Princeton Instruments.[120] The software provides the option to remove cosmic rays from the data, *i.e.*, to remove highly localized spikes that are for example caused by cosmic rays hitting the silicon sensor. In case of remaining outliers, the data can be processed using a Hampel filter.[121]

Chapter 7

# Theoretical calculations and simulations

## Density functional theory calculations

Density functional theory (DFT) is a quantum mechanical method to calculate the electronic structure of many-body systems. In this framework, many-electron systems are described through a functional of their electron-density.
DFT is based on the Hohenberg-Kohn theorem, which describes the properties of an inhomogeneous gas of interacting electrons in the presence of an external potential on the basis of its electron density. According to this theorem the total energy of such a system is a functional of its density, and the density that minimizes the total energy is the ground state density.[122] In an approach formulated by Kohn and Sham, this N-electron problem is reduced to a problem of N non-interacting electrons moving in an effective potential that consists of the external potential, the electrostatic potential, and an exchange-correlation (x-c) term.[123] The set of equations describing the electron density and the effective potential are referred to as the Kohn-Sham equations of DFT and must be solved self-consistently.[124]
By approximating this x-c functional, DFT facilitates the calculation of, *e.g.*, molecular geometries and electronic structures. To that end, the DFT based FHI-aims (Fritz Haber Institude *ab initio* molecular simulations) package was used.[125] It allows, *i.a.*, computing the electronic ground state of molecules or solids and the corresponding total energy and derived quantities for different charge and/or spin states.
The calculation alternates between electronic and ionic contributions, *i.e.*, first the charge density and the corresponding total energy of the electronic system is calculated for the input geometry. These values are then used as input to calculate the resulting relaxations of the ionic cores and the relaxed atomic coordinates are then again used as new input geometry. This cycle is repeated until the computed total energies, charge density and forces between the ionic cores have converged, that is the difference of these values between two consecutive computing cycles is smaller than the set accuracy levels.
As approximation to the exchange-correlation (x-c) functional either the Heyd-Scuseria-Ernzerhof (HSE) hybrid functional[126] or the Perdew–Burke-Ernzerhof (PBE) generalized gradient approximation[127] was used. For the atomic basis sets we employed the default settings, which can be varied between 'light', 'tight' and 'very tight'.

## AFM simulations

AFM images acquired with functionalized tips can be efficiently simulated *via* a well-established molecular-mechanics model implemented by P. Hapala and co-workers,[62,63] hereafter referred to as probe particle model (PPM). The model takes into account the flexibility of the probe particle at the tip apex and the interaction between tip and sample is modeled

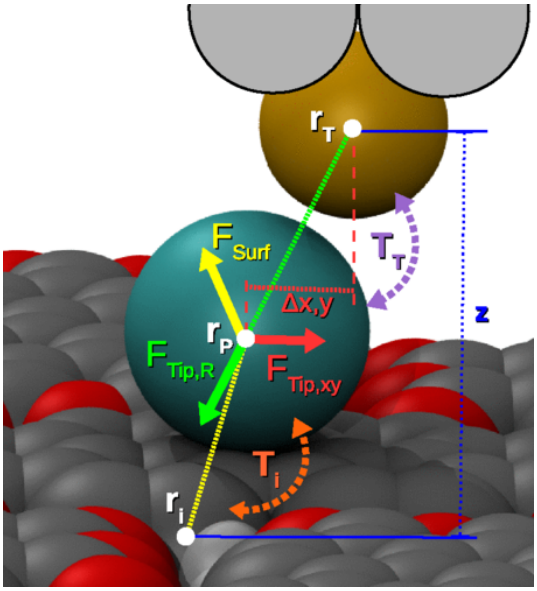


Figure 7.1: **Model of interactions between probe particle and sample.** Schematic view of the mechanical model of a functionalized tip. The last metal atom of the tip (tip base) is shown in sand color, the probe particle in cyan, and the molecular layer (sample, in the example a herringbone PTCDA layer) in gray (carbon atoms) and red (oxygen atoms). The forces acting on the probe particle are shown in color: radial tip force $F_{Tip,R}$ (green); lateral tip force $F_{Tip,xy}$ (red); force $F_{Surf}$ exerted by atoms of the sample (yellow). Force-determining geometric parameters are shown in the same color as the corresponding forces. The two distinct hopping processes in our STM model are denoted by violet (probe particle tip, $T_T$) and orange (probe particle sample, $T_i$) color. The reference distance $z$ is shown in blue. *Reprinted with permission from ref. [62]. Copyright (2014) American Physical Society.*

*via* classical force fields. Figure 7.1 illustrates the forces acting on the probe particle (blue sphere) that are included in the model, *i.e.*, a radial and lateral tip force $F_{Tip,R}$ (green) and $F_{Tip,xy}$ (red), respectively, stemming from the potential of the last metal atom of the tip (tip base, sand colored sphere), and the force $F_{Surf}$ exerted by atoms of the sample (yellow). They can be divided into three main force contributions: (i) The restoring force that keeps the probe particle below the tip base, which is described by a radial LJ potential and a lateral harmonic potential. (ii) Pauli repulsion and vdW interaction between the probe particle and the sample, which are modeled by a LJ pair potential (Equation 3.10). (iii) Electrostatic forces arising from the interaction between the sample and the multipole of the probe particle.
The PPM code together with an introduction and instructions on how to use it is available on `https://github.com/ProkopHapala/ProbeParticleModel` and `https://nanosurf.fzu.cz/wiki/doku.php?id=probe_particle_model`.

# Part III

# Results

## Chapter 8

# Elucidating the structure of molecules from early stages of soot formation

*The work presented in this chapter has been published. Text and figures are reprinted and modified with permission from refs. [128] and [129]. Copyright (2018) and (2019) Elsevier. The part presented in this chapter is shortened compared to the original publications and focuses mainly on the capabilities of AFM and STM to characterize certain molecules from mixtures. Hence, for more detailed information on, e.g., the preparation of the soot samples, additional characterization methods and the soot formation process I refer to the aforementioned publications.*

To date, most data on the chemical composition of complex molecular mixtures stems from mass spectrometry, nuclear magnetic resonance (NMR) spectroscopy and optical spectroscopic methods. In certain cases, molecule identification relies on the comparison with analytical standards and often requires the synthesis of new reference molecules.[130–132] This is a very indirect method and and the synthesis of new model compounds can take years. Most importantly, the above-mentioned methods only comprise averaging techniques and are thus only sensitive to more abundant molecules.
AFM with its sensitivity to electron density, on the other hand, has been shown to facilitate imaging of atoms and covalent bonds and can therefore identify single molecules from unknown organic samples.[133–135] In constant-height AFM, where the tip is scanned within a predefined plane above the molecule, variations in the atomic-scale contrast can be tied to either chemical contrast, *i.e.*, differences in electron density due to differences between chemical species, or variations in adsorption height, *i.e.*, differences in electron density due to differences in tip-molecule distance within the scanning plane.[65,136–140] Deviations from a planar geometry, *e.g.*, due to the presence of $sp^3$ hybridized carbon atoms, are thus visible in the AFM contrast. Hence, structure elucidation on single molecules can be achieved through the analysis of the contrast in constant-height AFM images at different tip-sample distances. An assignment of structural motifs is facilitated for example by comparison with model compounds or AFM simulations of different possible structures or orbital density imaging by STM of molecules adsorbed on bilayer NaCl and subsequent comparison with orbital densities from DFT.
However, sample preparation as well as imaging mechanism pose certain restrictions on the molecules and molecular structures that can be identified by AFM. The sample preparation technique poses an upper boundary on the molecular mass; during flash annealing, two competing processes take place being the sublimation of molecules and their fragmentation. Generally speaking, fast heating favors sublimation, however, depending on the size of the

molecules or the adhesive forces between them, fragmentation can dominate over sublimation.[117,118] Experiments show that this can be the case for molecules with masses of about 1000 Da and above.[141,142] On the other hand, very small molecules (< 100 Da) are typically very mobile on the surface and can therefore not be imaged. Another restriction in terms of imaging is the degree of planarity. Since AFM is only sensitive to the electron density in the imaged plane it is a surface-sensitive technique. Hence, bulky structures (*i.e.*, structures consisting of more than one 'layer' of atoms) cannot be identified. Single bulky moieties such as a single methyl group can make an exception, though, since they are often small enough to not cover the underlying structure and show a characteristic contrast evolution with varying tip-sample distance. Also, some degree of non-planarity can be dealt with by adjusting the scanning plane parallel to the molecule (part) rather than to the substrate.[143] These constraints lead to an over-representation of planar structures with molecular weight of 100–1000 Da. Hence, the analyzed AFM data is typically not statistically representative for the complete mixture. Nevertheless, high-resolution AFM and STM can serve as complementary analysis tools for the composition of complex molecular mixtures, like for example combustion products.

Combustion-generated soot particles can have significant impact on climate, environment and human health. Thus, understanding the processes governing the formation of soot particles in combustion is a topic of ongoing research. Especially the early stages of soot formation, *i.e.*, directly before and after the onset of the nucleation process, are central, though still highly debated, *e.g.*, regarding the exact size of the nanoparticles[144] , their chemical composition,[145] presence of five-membered rings,[146] and cross-linking among aromatic groups.[147,148] Since in these stages the size of the soot particles is on the order of 2–4 nm or slightly larger,[149–151] high-resolution AFM is a promising technique to identify different structures that are formed during soot formation.
The formation and evolution of soot particles in fuel-rich flames are the result of a complex mechanism including both chemical and physical processes. The soot formation process starts with the decomposition reactions of the fuel molecules, *i.e.*, pyrolysis and oxidation, and subsequent recombination and cyclization reactions lead to the formation of polycyclic aromatic hydrocarbons (PAHs). After nucleation, particles undergo further growth followed by coagulation/agglomeration and formation of chain-like aggregates. To simplify this highly complex problem and to allow controlling operative parameters with high precision, the majority of the studies aimed at investigating the soot formation mechanism are performed in laboratory premixed or diffusion flames of gaseous hydrocarbons. In a laminar premixed flame, the different stages of the soot formation process can be followed at increasing distances to the burner. Hence, collecting particles at different burner-to-probe separation distances provides snapshots of the particles involved in this intricate process.
We analyzed soot particles extracted from a laminar premixed flame at different burner-to-probe distances corresponding to the nucleation as well as particle growth zone.

## 8.1 Methods

Soot nanoparticles were generated in a laminar premixed flame burning an ethylene-air mixture in the groups of Mario Commodo[a] and Andrea D'Anna[b]. In this flame reactor, the

[a]Istituto di Ricerche sulla Combustione, CNR, P.le Tecchio 80, 80125 Napoli, Italy
[b]Dipartimento di Ingegneria Chimica, dei Materiali e della Produzione Industriale, Universitàdegli Studi di Napoli Federico II, P.le Tecchio 80, 80125 Napoli, Italy

temperature and the species concentrations only depend on the height above the burner, which directly relates to the flame residence time. Soot particles were collected from the flame at 8 and 14 mm burner-to-probe separation distance ($Z$), which correspond to the particle nucleation and particle growth zone of the flame, respectively. In the following, we will therefore refer to molecules detected in the particles extracted from the nucleation zone ($Z = 8$ mm) as incipient soot molecules (IS), and to molecules from particles collected in the growth zone ($Z = 14$ mm) as primary soot molecules (PS). The soot was collected on a quartz filter and analyzed by Raman spectroscopy before being shipped to the IBM Research lab. There, the soot particles were applied onto a Si-wafer (by gently pressing the quartz filter onto the wafer) that was subsequently transferred into the UHV chamber. The molecules were deposited onto a clean Cu(111)-surface, partially covered with bilayer NaCl held at $T \approx 10$ K by thermal sublimation.

## 8.2 Results

Figure 8.1 shows an excerpt of the identified molecular constituents of incipient as well as primary soot particles together with proposed structures (for the full set, see ref. [129]).
**IS20** and **IS55** (Fig. 8.1) show a uniform contrast, indicating a fully planar geometry as well as planar adsorption on the surface. This suggests that **IS20** and **IS55** are purely $sp^2$ hybridized PAHs. **IS22** and **IS56**, for example, exhibit bright features at their periphery in the AFM images. This indicates the presence of $sp^3$ hybridized C-atoms protruding from the molecular plane.[141] The structure assignment is facilitated by comparison with the model compound 1,2-dihydro-3,5-dimethylbenz(J)aceanthrylene (DHDMBA). As shown in Fig. 8.2a, DHDMBA contains an acenaphthene-type moiety (five-membered ring with two methylene moieties, see Fig. A.2b in the appendix). Because of the $sp^3$ hybridization, one of the two hydrogens for each C1 and C2 carbon atom is positioned above the plane of the molecular carbon backbone (Fig. 8.2b–d). As can be seen from the image at the largest tip-sample distance (Fig. 8.2b, $z = 2.20$ Å), this results in an onset of repulsive forces already at larger tip-sample distances compared to the carbon backbone, and thus the $CH_2$ moieties appear particularly bright in the AFM images. The out-of-plane hydrogens also govern the contrast between the C1 and C2 carbons, causing the C1-C2 bond to appear elongated with respect to its actual length. This is caused by the CO molecule tilting at the tip apex[5,63,133] and becomes more pronounced as the tip-sample distance is reduced (Fig. 8.2c, $z = 2.45$ Å). At the smallest tip-sample distance probed here (Fig. 8.2d, $z = 2.70$ Å), this effect also leads to the acenaphthene-type moiety appearing almost square-shaped. This characteristic evolution of the AFM contrast as a function of tip height is in very good agreement with the contrast observed on **IS22** and **IS56** as well as many of the soot molecules and allows us to assign this moiety with high certainty.
We can convert DHDMBA into its fully aromatic counterpart, 3,5-dimethylbenz(J)aceanthrylene (DMBA) by using atom manipulation to selectively dissociate one hydrogen from each of the two $CH_2$ moieties, as schematically depicted in Fig. 8.2e. In Fig. 8.2f, an AFM image of an intact DHMBA molecule is shown. Applying two consecutive voltage pulses of $V = 3.8$ V with the tip located above the molecule, we are able to successively remove one hydrogen from each $CH_2$ moiety and observe how the contrast in the AFM images changes (Fig. 8.2f–h). After the second pulse, we recover the usual contrast of an aromatic five-membered ring, with brightness similar to those of the adjacent six-membered rings and smaller apparent C1-C2 bond length compared to the doubly methylated molecule (Fig. 8.2i). Molecules **IS54** and **IS57** show bright features in their AFM images with a

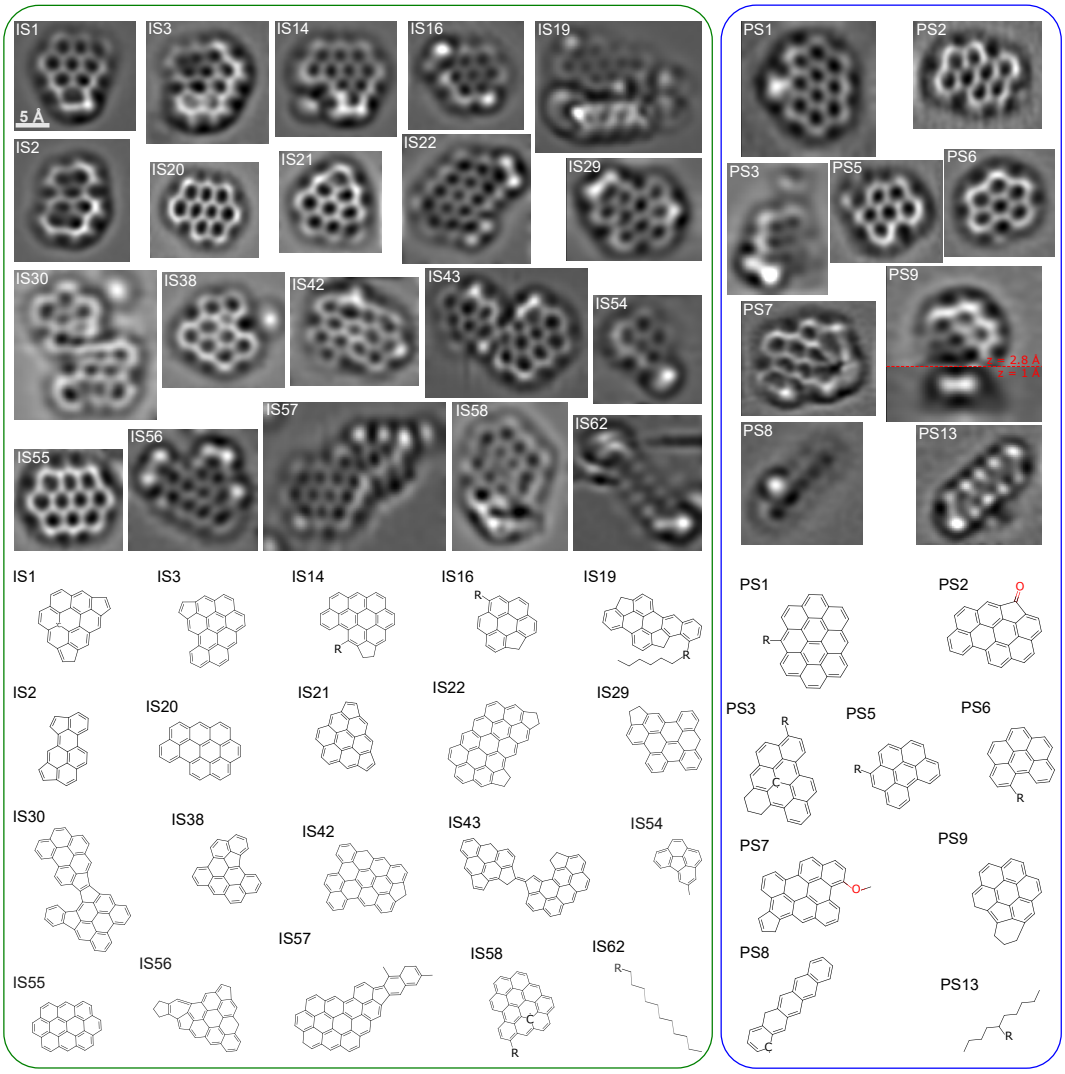


Figure 8.1: **AFM images of identified IS and PS molecules.** Laplace-filtered constant-height AFM images of an excerpt of identified molecules found in soot particles collected at $Z = 8$ mm (IS, indicated by a green frame) and $Z = 14$ mm (PS, indicated by a blue frame). The red line in **PS9** indicates a change in tip-sample distance during the constant-height scan; the top part of the image is recorded at a smaller tip-sample distance to facilitate atomic resolution while the bottom part is recorded at a larger tip-sample distance to avoid contact formation between the tip and the more bulky part of the molecule. For details on the IS and PS fractions, see text. All images have the same scale.

brightness similar to the one observed atop the methyl (–$CH_3$) groups in DHDMBA and DMBA. Due to their $sp^3$ character and since they are not directly incorporated into the otherwise mostly planar PAH, they can protrude even further out of the molecular plane than methylene moieties. This is visible in AFM images at large tip-sample distance (Fig. 8.2b, $z = 2.2$ Å). For decreasing tip-sample distance, the methyl group is pushed down by

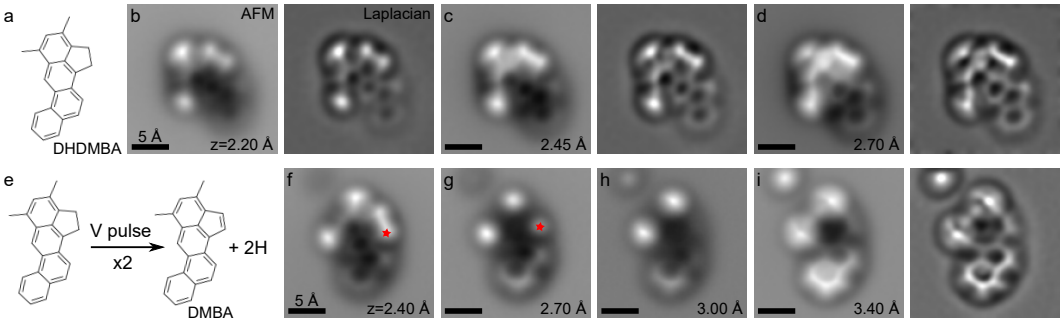


Figure 8.2: **Investigation of model compound DHDMBA.** (a) Chemical structure of acenaphthene-type model compound DHDMBA. (b)–(d) AFM images of DHDMBA at different tip-sample distances and corresponding Laplace-filtered images. (e) Schematic of the conversion of DHDMBA to DMBA by tip-induced atomic manipulation. (f) AFM image of initially intact DHDMBA. The red star indicates the tip position for the application of the first voltage pulse to remove one hydrogen from the first $CH_2$ moiety. (g) AFM image of the molecule after applying the first voltage pulse, with one H removed. (h) Image of the molecule after applying a second voltage pulse to also remove one H from the second $CH_2$ moiety, yielding DMBA. (f) AMF image of DMBA at smaller tip-sample distance and corresponding Laplace-filtered image. z values correspond to the decrease in tip height with respect to the STM set point of $V = 0.2$ V, $I = 0.5$ pA.

the tip such that the brightness of methylene and methyl groups assimilate (Fig. 8.2c, d, z = 2.45–2.7 Å). For very small tip-sample distances ((Fig. 8.2i, $z = 3.4$ Å)), a characteristic cross-shape is visible. This is in good agreement with the observed contrast on **IS54** and **IS57**, which can therefore be assigned to methyl groups.

In the AFM image of **PS2** a dark region is visible at the periphery of the molecule. This contrast is characteristic for oxygen.[65] As a heteroatom in planar PAHs, oxygen typically adsorbs closer to the surface compared to the neighboring carbon atoms. Its high electronegativity leads to an additional lowering of the electron density in the imaged plane. Hence, in constant-height AFM images oxygen and directly adjacent atoms appear darker than the C-atoms within the rest of the PAH.

AFM images of **IS62** and **PS13** show a zigzag structure characteristic for aliphatic chains.[141] About 120 molecules were analyzed by AFM; 44% of which were PAHs and 11% were substituted benzenes and chain-like structures with substantial aliphatic character. Molecules that are mobile on the surface during scanning (typically small, *i.e.*, $\lessapprox$ 100 Da) as well as non-planar/3D structures can typically not be identified by AFM. This applied to about 45% of the molecules.

From the structures identified by AFM some common characteristics of IS can be deduced: (i) The molecular masses range from 200 to 700 Da (14-60 C-atoms) with a large number of molecules with masses around 300 to 400 Da (24-30 C-atoms). (ii) A large fraction of the molecules contains fused six-membered ring units organized in almost entirely pericondensed (three rings share a common C-atom) structures. (iii) Several molecules exhibit aliphatic branches - mostly methyl ($CH_3$) groups. (iv) Most of the imaged molecules contain five-membered-rings on their periphery (see also Fig. A.2a in the appendix) while a smaller fraction shows five-membered rings (partially) embedded into the aromatic structure (see also Fig. A.1 in the appendix). (v) A large presence of $sp^3$ hybridized carbons forming C-H bonds in methylene-type groups is observed in peripheral five-membered rings (see also Fig.

A.2b–d in the appendix), and in some cases also in peripheral six-membered rings.
The analysis and identification of the molecules constituting the particles after coagulation/growth (PS) turned out to be more challenging. For these particles, sublimation appeared to be a major bottleneck. The analyzed sample mostly contained very bulky or small/mobile molecules and aliphatic chains, which we attribute to fragmentation of the molecules during the sublimation process. Only few aromatic molecules (about 7%) could be identified; the corresponding AFM images as well as proposed structures are shown in Fig. 8.1. Although the resolved aromatics are of limited statistical significance because of their small number, the average size of the molecules that could be analyzed by AFM is similar to that of the molecules from IS. Different from the molecules found in incipient soot, a few of the imaged molecules (**PS2**, **PS7**) contain oxygen atoms.

## 8.3 Discussion

Our results show a large complexity of the molecular constituents of soot collected in a laminar premixed flame, ranging from small aliphatic chains/substituted benzene molecules to few very large polyaromatic compounds containing up to 52 carbon atoms (*e.g.*, **IS30** in Fig. 8.1). Furthermore, molecules with aliphatic branches with an increased abundance in primary soot particles have been identified, mostly in the form of methyl groups. This is the first direct observation of a rather large fraction of soot constituents in the form of alkylated aromatics. Their importance in the physical agglomeration of PAHs leading to soot formation has already been theorized.[152]
The third relevant observation is the presence of an appreciable number of aromatic molecules containing five-membered rings. Different types of peripheral five-membered rings are observed, as shown in Fig. A.1a–d in the appendix. Their configurations allow certain inferences on their formation mechanism within the flame. To the best of our knowledge, our results represent the first observation of the existence of acenaphthene- and acenaphthylene-type five-membered rings in soot.
Further structural motifs contain methylene groups. They results in a higher value of the H/C ratio of the soot molecules compared to purely benzenoid pericondensed aromatics, commonly considered as precursors to soot. In the soot formation process methylene groups could either foster the formation of $\pi$-radicals (upon H abstraction) or be formed from $\pi$-radicals (upon H addition). Hence, their abundance indicates that $\pi$-radicals play a fundamental role in the soot formation process. Our AFM analysis also indicates the presence of such radicals among soot molecules, as apparent from the proposed chemical structures in Fig. A.3a in the appendix. The $\pi$-radical **IS1**, for example, could have been formed by removal of a hydrogen atom from the C-atom highlighted in red, as proposed in Fig. A.3b in the appendix, forming a delocalized unpaired electron ($\pi$-radical). Our results on $\pi$-radical formation allow a new interpretation of particle inception and can probably explain the different tendency to sublime molecules from IS and PS. IS is composed of PAHs with different molecular sizes and shapes. These molecules are probably mostly held together by weak van der Waals forces, so that they easily sublime without decomposing during sample preparation. Soot particle growth is driven by $H_2$ release during molecular organization.[153,154] This can, for example, lead to the formation of chemical bonds between different aromatic units, *i.e.*, the formation of archipelago-type/cross-linked structures. This is supported by the presence of structures such as **IS43**, where the two aromatic subunits are linked via a C–C bond, and **IS30**, which might have been formed by the fusion of two five-membered rings and $H_2$ loss. Figure A.4 in the appendix shows a comparison of STM orbital density

images at the PIR and NIR of **IS43** with orbital densities of the proposed structure calculated by DFT, corroborating that the two aromatic subunits are indeed linked via a covalent bond. These molecules might also indicate that chemical cross-linking between aromatics is promoted by the presence of peripheral five-membered rings. On the other hand, the observation of a large number of methylene groups results in the possibility of having many resonantly stabilized $\pi$-radicals within the pool of soot's molecular constituents. The presence of $\pi$-radicals may increase the binding forces among aromatics,[155] thus enhancing the clustering/aggregation propensity of PAHs at the early stages of the soot formation process, potentially explaining why it was challenging to sublime the molecules from the sample of PS.

## 8.4 Conclusions

Within the above mentioned restrictions in terms of size and planarity, high-resolution AFM allows investigating and identifying *a priori* unknown molecules from molecular mixtures such as soot particles.
In incipient (IS) and early grown flame-formed soot (PS), extracted from a slightly sooting ethylene/air premixed flame but at two different flame positions, a large complexity of molecular constituents was found. Not all the features were present in both samples, still, common characteristics were the molecular masses, ranging from 200 to 700 Da with most molecular masses around 300 to 400 Da, as well as the distinct radical character of some molecules that could be identified. In IS, we frequently observed molecules containing fused six-membered ring units organized in almost entirely pericondensed structures and several molecules exhibiting aliphatic side-groups. Many of the imaged molecules contained five-membered rings on their periphery, a smaller fraction partially embedded into the aromatic structure. A large fraction of molecules contained $sp^3$ hybridized carbons forming C-H bonds in methylene-type groups, which we confirmed by comparison with a model compound. This may have some implications on the understanding of molecule clustering and particle inception. In addition, we found evidence for the presence of $\pi$-radicals as well as the formation of archipelago-type/cross-linked structures among the detected soot molecules, both of which are believed to play a role during the aging process of the soot particles.

## Chapter 9

# Formation of cyclo[18]carbon by atom manipulation

*Most of the work presented in this chapter has been published. Text and figures are reprinted and modified with permission from refs. [156] and [157]. Copyright (2019) American Association for the Advancement of Science and (2020) American Chemical Society.*

In 1990, D. Eigler and E. Schweizer used an STM tip to move single atoms with atomic precision,[9] demonstrating for the first time that single atoms can be deliberately manipulated using STM. Since then, this technique has been extended, showing that atoms and even molecules can be moved laterally[9–12] and even picked up and dropped again.[13,14] In addition to moving single adsorbates, the SPM tip can be used to locally trigger chemical reactions, for example by applying voltage pulses between tip and sample.[15–18]
Using high-resolution AFM with functionalized tips it is possible to identify reaction products as well as reaction intermediates formed by atom manipulation.[24,158] Exploiting the conditions that are typically present in those experiments, *i.e.*, low temperatures and UHV, and having the reactants adsorbed on an inert surface like NaCl, it is thus feasible to create and characterize highly reactive molecules that would not be stable under standard synthesis conditions (*e.g.*, room temperature or ambient pressure).[25,159]

One particular example for a highly reactive molecule whose structure has been heavily debated since its prediction in 1966 is cyclo[18]carbon.[160] Carbon exists in different forms, known as allotropes. They can have a variety of structures and properties, but so far, only four- and three-fold coordinated carbon allotropes, could be stably isolated. The idea to build carbon allotropes from $n$ two-fold coordinated atoms forming rings (cyclo[$n$]carbons) has been introduced in the 1960's[160] and has since then fascinated chemists. Especially the question concerning their aromaticity has been highly debated. Cyclo[18]carbon is predicted to be one of the most stable cyclocarbons[160,161] and there is evidence for the existence of cyclocarbons in the gas phase,[161–164] still, due to their high reactivity, cyclocarbons could not be isolated or characterized. A route to synthesizing stable precursors to cyclocarbon, though, has been introduced by Diederich and coworkers 30 years ago.[161]

A distinctive feature of *sp*-hybridized carbon allotropes is that they possess two perpendicular $\pi$-conjugated electron systems (Fig. 9.1a). Hückel's rule predicts for planar, cyclic conjugated systems with $(4n + 2)$ $\pi$ electrons an aromatic structure with no bond-length alternation (BLA).[165] Diederich predicted, in 1989, that two orthogonal ring currents would be formed in $C_{18}$, causing double aromatic stabilization.[161] Since then, the structures of cyclo[$n$]carbons have been a topic of theoretical debate, and the results depend on the level of theory.[165–167] Most DFT and Møller-Plesset perturbation theory calculations predict that

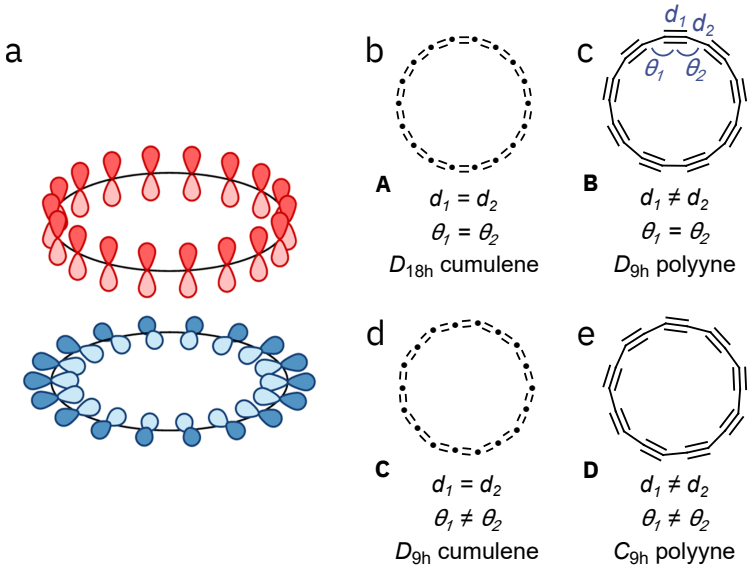


Figure 9.1: **Possible resonance structures of cyclo[18]carbon.** (a) Visualizations of the perpendicular $\pi$-systems. (b)–(e) Four possible structures of cyclo[18]carbon, **A**-**D**. (b) **A**: $D_{18h}$ cumulene with $d_1 = d_2 = 1.30$ Å, $\theta_1 = \theta_2 = 160°$. (c) **B**: $D_{9h}$ polyyne with $d_1 = 1.38$ Å, $d_2 = 1.24$ Å, $\theta_1 = \theta_2 = 160°$. (d) **C**: $D_{9h}$ cumulene with $d_1 = d_2 = 1.24$ Å, $\theta_1 = 171.4°$, $\theta_2 = 148.6°$. (e) **D**: $C_{9h}$ polyyne with $d_1 = 1.38$ Å, $d_2 = 1.24$ Å, $\theta_1 = 173.1°$, $\theta_2 = 146.9°$.

the lowest energy geometry of $C_{18}$ is cumulenic $D_{18h}$[166,167](Fig. 9.1b). However, second-order Jahn-Teller effects have been proposed to cause both BLA and bond-angle alternation (BAA) in these homo-atomic rings.[166,168–171] Theoretical studies have suggested four possible geometries for $C_{18}$: $D_{18h}$ cumulene, $D_{9h}$ polyyne, $D_{9h}$ cumulene and $C_{9h}$ polyyne (**A**–**D**, Figure 9.1b–e).[166,168–171]

Most attempts at synthesizing cyclocarbons have used a masked alkyne equivalent incorporated into a cyclic precursor designed to generate cyclo[$n$]carbon when activated by heat or light. Methods of unmasking included a retro-Diels-Alder reaction,[161] decomplexation,[172] decarbonylation[173] and [2 + 2] cycloreversion.[174] These attempts have given tantalizing glimpses of cyclo[$n$]carbon in the gas phase. Gas-phase electronic spectra of $C_{18}$, formed by laser ablation of graphite, have been measured, but these studies did not reveal whether the structures are cumulenic, *i.e.*, with consecutive double bonds, or polyynic with alternating bond lengths.[175]
An alternative to gas phase detection of highly reactive molecules is to detect them on an inert surface at low temperature using scanning probe techniques. STM and AFM are powerful tools for the structure elucidation and characterization of single molecules.[5,23,176] In addition, by atom manipulation, *e.g.*, applying bias voltage pulses between tip and sample, certain chemical reactions can be triggered,[16,19,25,176] even on inert surfaces like thin insulating layers. This allows, *i.a.*, the investigation of reaction intermediates or the formation and characterization of highly reactive species.[25,156] Following this approach we used two different precursor molecules ($C_{24}O_6$ and $C_{18}Br_6$, Fig. 9.2a and b) synthesized by Lorel Scriven from the group of Prof. Harry Anderson (Oxford University) to form cyclo[18]carbon and

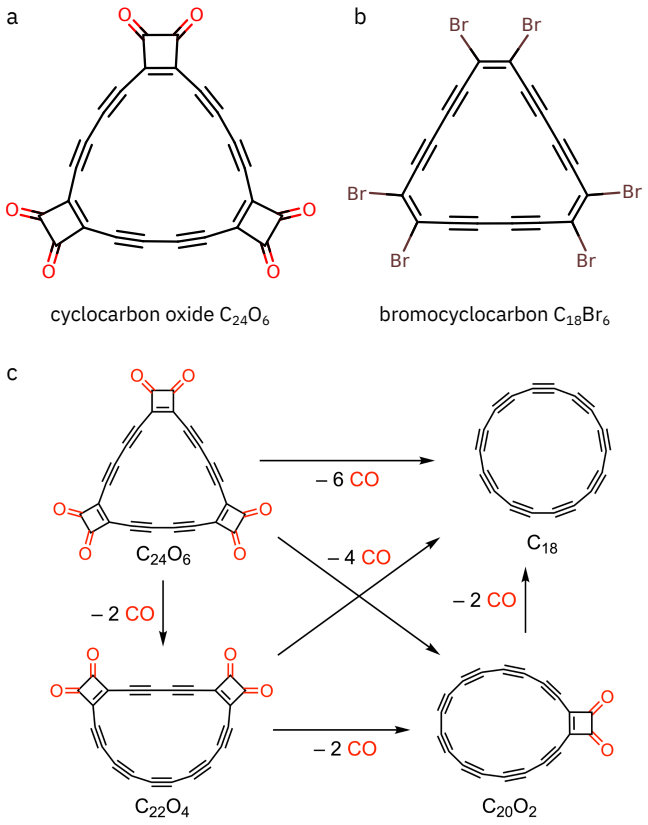


Figure 9.2: **Reaction scheme for the on-surface synthesis of cyclo[18]carbon.** Chemical structure of (a) the cyclocarbon oxide precursor $C_{24}O_6$ and (b) the bromocyclocarbon precursor $C_{18}Br_6$. (c) Reaction scheme for on-surface formation of cyclo[18]carbon from $C_{24}O_6$.

investigate its structure adsorbed on a thin insulating film.

Cyclocarbon oxides ($C_{8n}O_{2n}$), developed by Diederich and co-workers, were selected as suitable candidates for on-surface cyclocarbon generation as their molecular weight is sufficiently low (384.25 g/mol for $C_{24}O_6$) for sublimation and the masking groups (three $(CO)_2$ units in total) are small and expected to be planar with respect to the carbon ring, which facilitates the imaging of the molecule with AFM. To form cyclo[18]carbon from cyclocarbon oxide (Fig. 9.2c) six CO moieties need to be dissociated *via* atom manipulation. In $C_{24}O_6$ the bonds between the carbon ring and the masking groups are covalent C-C single bonds as are the directly adjacent bonds within the carbon ring. This implies that both neighboring bonds are likely to be of similar energy, which could render their breaking a similarly likely process, potentially quenching the yield of cyclo[18]carbon formation. It has been shown that tip-induced unmasking in STM/AFM experiments can work reliably on halogenated molecules[20,25] due to the weaker nature of carbon-halogen bonds compared to covalent carbon-carbon bonds. Thus, an additional target precursor based on dehalogenation, $C_{18}Br_6$ was selected. The molecular weight (695.62 g/mol) is sufficiently low, and based on previous results on dehalogenation of carbon-rich structures by atom manipulation[25] we

predicted that their unmasking could be achieved under mild conditions
Cyclocarbon oxides are light-sensitive and prone to decomposition whereas $C_{18}Br_6$ shows remarkable stability in solution and the solid state. The precursor molecules were thus shipped on dry-ice immediately after their synthesis was completed, prepared for sublimation directly upon their arrival at the Zurich Research Lab, and transferred into the UHV system as fast as possible without contaminating the UHV chamber to minimize the degree of decomposition prior to sublimation. $C_{18}Br_6$ was found to be a shock-sensitive explosive (*e.g.*, when scratched with a spatula) and thus care was taken to work on a small scale and only with non-flammable solvents. Both, $C_{24}O_6$ and $C_{18}Br_6$ are thermally stable up to approximately 85°C and thus for both precursors thermal sublimation, which requires temperatures of $T \approx 600$°C, turned out to be a bottleneck. Cyclocarbon oxide was observed to explode upon sublimation and while for bromocyclocarbon no explosions were observed, the sublimation yield was still found to be low. Thus, several sublimation cycles were necessary for both precursor molecules to achieve a reasonable coverage of molecules on the sample surface.
As we could not find any intact or (partially) unmasked precursors on the bare Cu(111) surface, possibly due to its high reactivity, all atom-manipulation experiments were carried out on bilayer NaCl. AFM images were simulated using the probe particle model[62] based on the structure relaxed in the gas phase, calculated by DFT, see Appendix B.

## 9.1 Cyclo[18]carbon from cyclocarbon oxide $C_{24}O_6$

After deposition, we found molecules of the precursor $C_{24}O_6$ on the NaCl surface, as well as some fragmented or (partially) decarbonylated molecules and single CO molecules (Fig. 9.3). This observation indicates that partial decarbonylation and dissociation took place during sublimation. Figure 9.4 shows AFM data and corresponding simulations for $C_{24}O_6$ and products created by atom manipulation. $C_{24}O_6$ molecules appear as triangular objects with dark features at the corners and two bright protrusions at each side (Fig. 9.4b). The dark contrast is characteristic of ketone groups. Due to the high electron affinity of oxygen and a reduced adsorption height compared to their neighboring C atoms, the electron density is comparatively low in the imaged region above O atoms. This leads to reduced Pauli repulsive forces in the imaging plane above the oxygen compared to the carbon and thus, ketone groups appear as dark contrast in the $\Delta f$ signal in constant-height AFM images.[65]
In AFM images recorded at moderate tip height, differences in bond order are visible in the $\Delta f$ signal with high brightness, *i.e.*, high $\Delta f$ indicating high bond order.[6,23,25] In the AFM image recorded at larger tip-sample distance ('AFM far', Fig. 9.4b) the two bright features at each side of the molecule can be assigned to triple bonds. At smaller tip-sample distance ('AFM close', Fig. 9.4c), repulsive forces have a greater contributions and tip relaxations, *i.e.*, tilting of the CO at the tip apex, affect the AFM images substantially. These effects lead to an apparent sharpening of the bonds, and pronounced differences in apparent bond lengths.[6,62,177] Both, the dark contrast atop the ketone groups as well as the bright lobes atop triple bonds, that transition into sharp, bond-like features, can be nicely reproduced in AFM simulations for different tip-sample distances (see Fig. 9.4 for comparison and Appendix B Fig. B.8 for additional information on the AFM simulations). The different contrasts of the three different sides of $C_{24}O_6$ (Fig. 9.4b) suggest an adsorption geometry that is not parallel to the surface.[65]

To decarbonylate the $C_{24}O_6$ precursor, the tip was positioned in the vicinity (a few nanome-

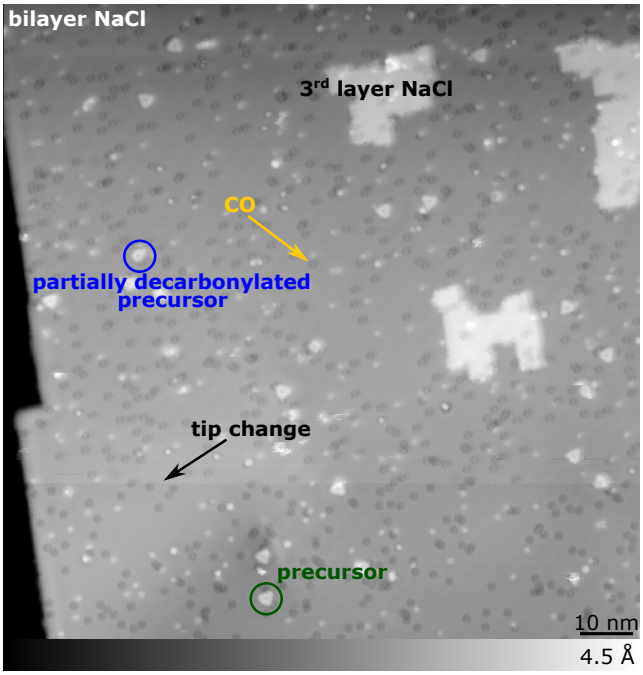


Figure 9.3: **Overview image.** STM overview recorded at a setpoint of $V = 0.4$ V, $I = 0.5$ pA. Most of the image shows bilayer NaCl on Cu(111), a few islands of third layer NaCl are visible (3rd layer NaCl). The small depressions are single CO molecules. The overview shows mainly intact $C_{24}O_6$ precursor molecules (example shown in the dark green circle) and a few partially decarbonylated intermediates (example shown in the blue circle). In the lower part of the image, the contrast changes abruptly, which can be attributed to a tip change.

ters) of the molecule, retracted by about 3 Å from the STM setpoint (typically $V = 0.2$ V and $I = 0.5$ pA) and the sample bias voltage $V$ was increased to about $V = +3$ V, for a few seconds. We found that decarbonylation was rather delocalized and hence also possible for lateral distances of several nm between tip and molecule. Because of the nonlocality of the process, we tentatively propose that it is mediated by hot interface-state charge carriers,[176,178–180] without excluding an influence of the electric field on the dissociation barriers. In most cases, two, four or six CO molecules were removed with one voltage pulse, such that either the product cyclo[18]carbon or an intermediate, with an even number of COs still attached, was formed. The most abundantly formed intermediates were those with either one or two intact masking groups still attached ($C_{22}O_4$ in Fig. 9.4f and $C_{20}O_2$ in Fig. 9.4k)). Other molecules that were less frequently created from $C_{24}O_6$ by voltage pulses are shown in Fig. B.4 in Appendix B.

The removal of a masking group ($(CO)_2$) results in the formation of a longer bent polyynic segment. Assigning the bright features in the 'AFM far' images to the location of triple bonds, we observed curved polyyne segments with the expected number of triple bonds: 5 in $C_{22}O_4$ (Fig. 9.4g) and 8 in $C_{20}O_2$ (Fig. 9.4l). At small tip height (Fig. 9.4h and m), sharp bond-like features with corners at the assigned positions of triple bonds and straight lines in between are visible. This contrast can be explained by CO tip relaxation, in that maxima in the potential energy landscape, from which the tip apex is repelled, are located

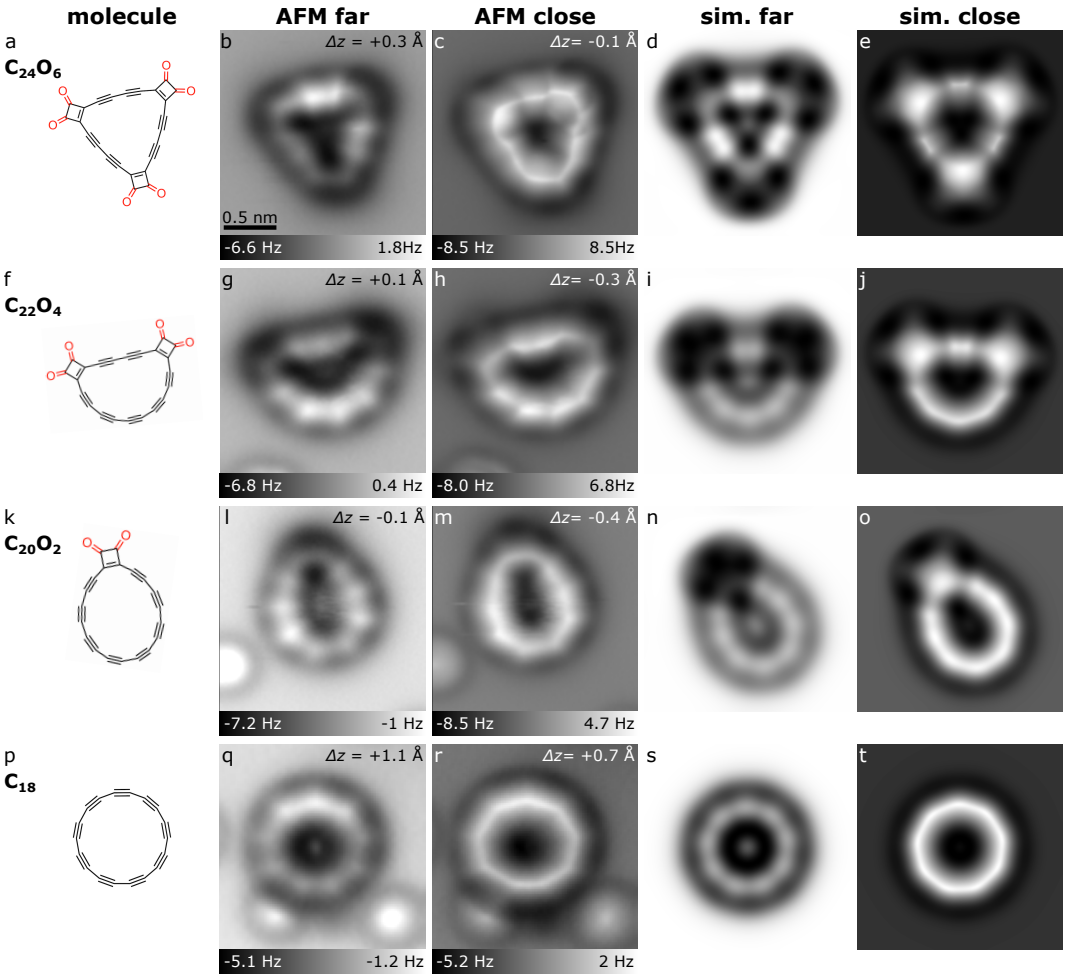


Figure 9.4: **$C_{24}O_6$ precursor and products generated by tip-induced decarbonylation.** Structures are shown in column 1. AFM images (columns 2 and 3) were recorded at different tip offsets $\Delta z$, with respect to an STM setpoint of $I = 0.5$ pA, $V = 0.2$ V above the NaCl surface. (a)–(e) Precursor. (f)–(j) and (k)–(o) The most frequently observed intermediates. (p)–(t) Cyclo[18]carbon. The bright features in the lower part of (l), (m), (q), and (r) correspond to individual CO molecules. Columns 4 and 5 show simulated AFM images based on gas-phase DFT-calculated geometries. The difference in probe height between 'sim. far' and 'sim. close' corresponds to the respective difference between 'AFM far' and 'AFM close'. The scale bar in (b) applies to all experimental and simulated AFM images.

above the triple bonds because of their high electron density. In between these maxima, ridges in the potential landscape lead to straight bond-like features.[62,63,181] The assignment of the intermediates is further supported by AFM simulations (Fig. 9.4, $4^{th}$ and $5^{th}$ column) and STM images within the fundamental gap and at the ion resonances (see Appendix B and Figs. B.1 and B.2).

The removal of all three masking groups from $C_{24}O_6$ typically resulted in circular molecules (Fig. 9.4q and r) that are identified as cyclo[18]carbon. At moderate tip heights (Fig. 9.4q) the resulting molecule exhibits a cyclic arrangement of nine bright lobes. For smaller tip heights (Fig. 9.4r), the contrast difference between the bright lobes and the darker spacings in between them gradually disappears. The lobes that are observed at larger tip-sample distances transition into corners that are connected by bright, bond-like features and the molecule appears as a nonagon (Fig. 9.4q and Fig. B.7d in Appendix B). Such a contrast, as is typically observed above regions of high exposed electron density, allows certain inferences on the ground state structure of cyclo[18]carbon on bilayer NaCl and will be discussed in more detail in section 9.3.
The non-uniform brightness of the bright features indicates that its adsorption geometry is not parallel to the surface (see also Appendix B Fig. B.7), with the brighter parts of the molecule indicating their increased adsorption height,[65] as also observed for $C_{24}O_6$. The non-planar adsorption could be related to the mismatch in symmetry of cyclo[18]carbon with the fourfold symmetric NaCl surface. The AFM images shown in Fig. B.7c and d were recorded at tip sample distances where a part of the molecule shows the contrast for larger heights (*cf.* 'AFM far' in Fig. 9.4), *i.e.*, with bright lobes along the carbon ring, while on the opposing side of the ring the contrast for small tip heights is visible ('AFM close' in Fig. 9.4), *i.e.*, corners connected by sharp lines. These images visualize the non-planar adsorption geometry of the molecules and the evolution of the contrast as a function of tip-sample distance. Moreover, they corroborate that the corners observed at small tip height are at the locations of the bright lobes at large tip height.
Cyclo[18]carbon was very mobile on the surface and often jumped to a different location during STM and AFM imaging (see also Appendix B), indicating a low diffusion barrier on bilayer NaCl. It was usually found adjacent to other adsorbates, mostly CO molecules. This is visible in Fig. B.7a to c in Appendix B, where the bright contrast directly next to the cyclo[18]carbon stems from adjacently adsorbed CO molecules. We conclude that these CO molecules were not covalently bound to cyclo[18]carbon, because of the following observations: i) The adjacent CO molecules show the same contrast and adsorption site (on top of Na cations) as single isolated CO molecules, indicating they are also adsorbed in a vertical geometry on the NaCl surface. ii) If a cyclo[18]carbon jumped to a different adsorption site, the previously adjacent CO molecules did not move in conjunction with it. iii) The typical observed distance between cyclo[18]carbon and adjacent CO molecules, determined from the separation of $\Delta f$ maxima in AFM images (Fig. B.7a to c), is about 4 Å, which is too large for a covalent bond, even when taking into account possible image distortions for tip relaxations. Presumably, the CO molecules interact with the cyclo[18]carbon *via* van der Waals forces and stabilize the cyclo[18]carbon molecule such that it can be imaged without moving. However, the presence of the closely adsorbed CO molecules can affect the tilting of the CO tip and thus lead to distortions during constant-height imaging at small tip-sample distances, affecting also the contrast observed above cyclo[18]carbon in the vicinity of CO molecules.

For different reactions we observed different voltage thresholds that increased with the number of already dissociated masking groups. The voltage threshold for decarbonylation, at positive voltage polarity and typical currents on the order of pA, increased from about +1.5 V for the first decarbonylation ($C_{24}O_6$ to $C_{22}O_4$) to about +2.5 V for the final, third decarbonylation ($C_{20}O_2$ to $C_{18}$). The most successful conditions for decarbonylation involved large tip-sample distances (small currents, *i.e.*, $I < 1$ pA) and bias voltages of about +3 V. Table B.1 in Appendix B summarizes the outcome of all tip-induced decarbonylation

attempts starting from either the intact precursor or one of the intermediates. The two most abundant intermediates are listed separately and denoted by their chemical formula $C_{22}O_4$ and $C_{20}O_2$, respectively. We evaluated a total of 90 atomic manipulation events, in which the initial and final product were characterized. The resulting yield for the generation of cyclo[18]carbon from the precursor $C_{24}O_6$, including its synthesis *via* intermediates, was calculated by summing the measured individual yields (Table B.1) for the observed pathways. The respective yields per pathway are shown in Table B.2. The resulting total yield for the on-surface synthesis of cyclo[18]carbon by atom manipulation was 13% for the cyclocarbon oxide precursor.

## 9.2 Cyclo[18]carbon from bromocyclocarbon $C_{18}Br_6$

Sublimation of $C_{18}Br_6$ yielded almost exclusively intact $C_{18}Br_6$ molecules on bilayer NaCl on Cu(111) with no appearance of $C_{18}$. A small fraction of the molecules (less than 5%) appeared to be missing one of the six Br atoms. This indicates that, unlike for the cyclocarbon oxide precursor $C_{24}O_6$, no significant unmasking occurs during sublimation. Figure 9.5a–d shows AFM images of the intact $C_{18}Br_6$ precursor recorded at different tip-sample distances, showing the characteristic triangular shape. The six bright features at the corners relate to the Br atoms and the bright features along the edges of the triangular core correspond to C ≡ C triple bonds.[23] The non-uniform brightness of Br atoms and triple bonds within the molecule results from a non-planar adsorption geometry, with the brighter parts of the molecule indicating their greater height.[65] These differences are most distinct in the AFM images recorded at larger tip-sample distances. At smaller distances, tip relaxations, such as tilting of the CO, affect the AFM images considerably.[6,62,177] This leads to obscured contrast differences related to nonplanarity as well as an apparent sharpening of the bonds up to the point where the contrast of neighboring triple bonds blends (see Fig. 9.5c, d).

Debromination of $C_{18}Br_6$ was typically achieved by positioning the STM tip a lateral distance of 1–3 nm from the center of the molecule, retracting it by 2–3 Å from the STM setpoint (typically $V = 0.2$ V, $I = 0.5$ pA) to minimize the tunnel current ($I < 50$ fA) and increasing the bias voltage to 2 V for up to 5 s. With this procedure we could remove 1 to 6 bromines and ultimately generate cyclo[18]carbon from $C_{18}Br_6$ with a yield of ≈ 64%. In some cases, partially debrominated intermediates could be observed. The dissociated Br atoms typically stayed directly adjacent to the molecule (see also Figs. B.5 and B.6 in Appendix B). This could lead to imaging artifacts such as apparent bonds that relate to the flexibility of the CO at the tip apex rather than the presence of a real bond.[62,182] In addition, adjacent Br atoms appeared to influence and distort the geometry of the partially debrominated intermediates. As a result, for the intermediates it was not always clear whether and how many Br atoms were actually dissociated. For cyclo[18]carbon, however, the circular geometry as well as the appearance of the characteristic nine bright lobes on the ring allowed for an unambiguous assignment of the molecular structure. Table B.3 in Appendix B summarizes the outcome of all tip-induced debromination attempts starting from either the intact precursor or a partially debrominated intermediate. The increased yield of formation of cyclo[18]carbon from $C_{18}Br_6$ (compared with formation from $C_{24}O_6$) is probably related to the lower voltage required for unmasking, which renders it less likely to break covalent bonds within the carbon ring upon atom manipulation. Thus cyclo[18]carbon could be generated more reliably and in higher yield compared to the formation from $C_{24}O_6$.

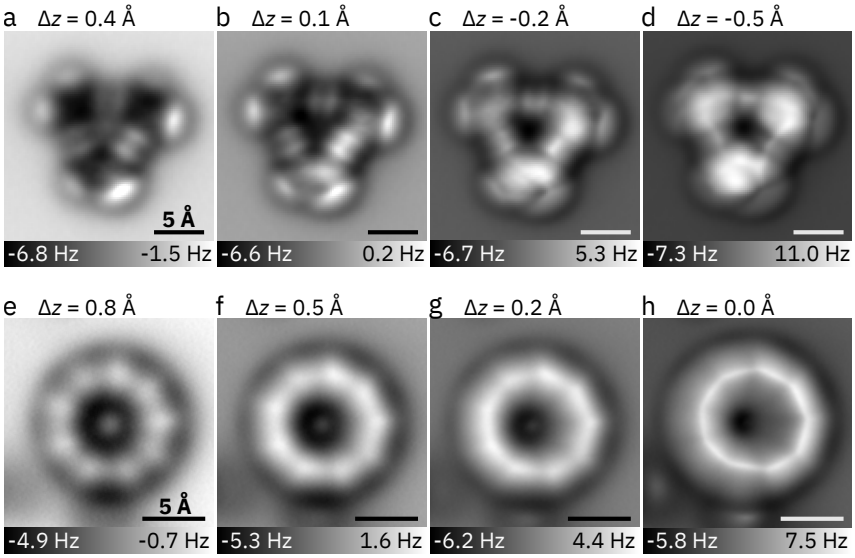


Figure 9.5: **$C_{18}Br_6$ precursor and products generated by tip-induced debromination.** AFM images were recorded with different tip offsets $\Delta z$, with respect to an STM setpoint of $I = 0.5$ pA, $V = 0.2$ V above the NaCl surface. (a)–(d) $C_{18}Br_6$ precursor. (e)–(h) Cyclo[18]carbon generated from $C_{18}Br_6$ by atom manipulation. The dark features next to the molecule (e) and (f) (bright features in (g) and (h)) correspond to individual dissociated Br atoms. All scale bars correspond to 5 Å.

Figure 9.5e–h shows AFM images of cyclo[18]carbon synthesized from $C_{18}Br_6$ recorded at different tip-sample distances. Cyclo[18]carbon adsorbs in a non-planar geometry on bilayer NaCl. In Fig. 9.5e–h, the plane for constant-height imaging was adjusted by 4° with respect to the plane of the NaCl surface to adjust the tilt of the imaging plane to be parallel to the molecular plane, so as to obtain a uniform contrast across the molecule. The dark features next to the cyclo[18]carbon molecule in Fig. 9.5e (bottom and left), which become bright features in Fig. 9.5h, can be assigned to the dissociated bromine atoms. They were found to stabilize the cyclo[18]carbon molecules and prevent lateral movement. The contrast of the product is identical to cyclo[18]carbon formed from $C_{24}O_6$; the molecule shows nine bright lobes in the AFM images recorded at larger tip-sample distances (9.5e and f) that transition into nine corners for smaller tip-sample distances (9.5g and h).

## 9.3 Structure elucidation

The structure of cyclo[18]carbon on the surface can be inferred from the AFM contrast and by comparison to simulated AFM images of model geometries. In AFM images recorded at large tip-sample distances (Figs. 9.4q and 9.5e, f), the molecules exhibit a nine-fold geometry with nine bright lobes. This indicates that cyclo[18]carbon possesses a non-uniform electron density along the carbon ring. For comparable bonds (*i.e.*, bonds with the same environment), such contrast variations are typically observed in structures containing bonds with different bond order.[6,23] In the case of $C_{18}$, this implies that the molecule has a considerable polyynic character, *i.e.*, alternating single and triple bonds. This inference was verified by comparison of the experimental data with simulated images of $C_{18}$ using the probe

particle model[62] based on model geometries **A**-**D** with different degrees of BLA and BAA. Bond lengths and bond angles were adopted from previously published high level ab initio CCSD theory calculations with the cc-pVDZ basis set ($D_{18h}$ cumulene: $d_1 = d_2 = 1.30$ Å, $\theta_1 = \theta_2 = 160°$; $D_{9h}$ polyyne: $d_1 = 1.38$ Å, $d_2 = 1.24$ Å; $\theta_1 = \theta_2 = 160°$. $D_{9h}$ cumulene: $d_1 = d_2 = 1.30$ Å, $\theta_1 = 162.9°$, $\theta_2 = 157.2°$; $C_{9h}$ polyyne: $d_1 = 1.38$ Å, $d_2 = 1.24$ Å, $\theta_1 = 163.3.1°$, $\theta_2 = 156.7°$).[171] Figure 9.6 shows again the experimental data from Fig. 9.5 together with simulated AFM images of the theoretically predicted structures.
The simulated AFM images of cyclo[18]carbon with a $D_{18h}$ cumulene geometry (see also Fig. B.9 in Appendix B) show a uniform circular shape, without contrast modulations for all tip-sample distances.

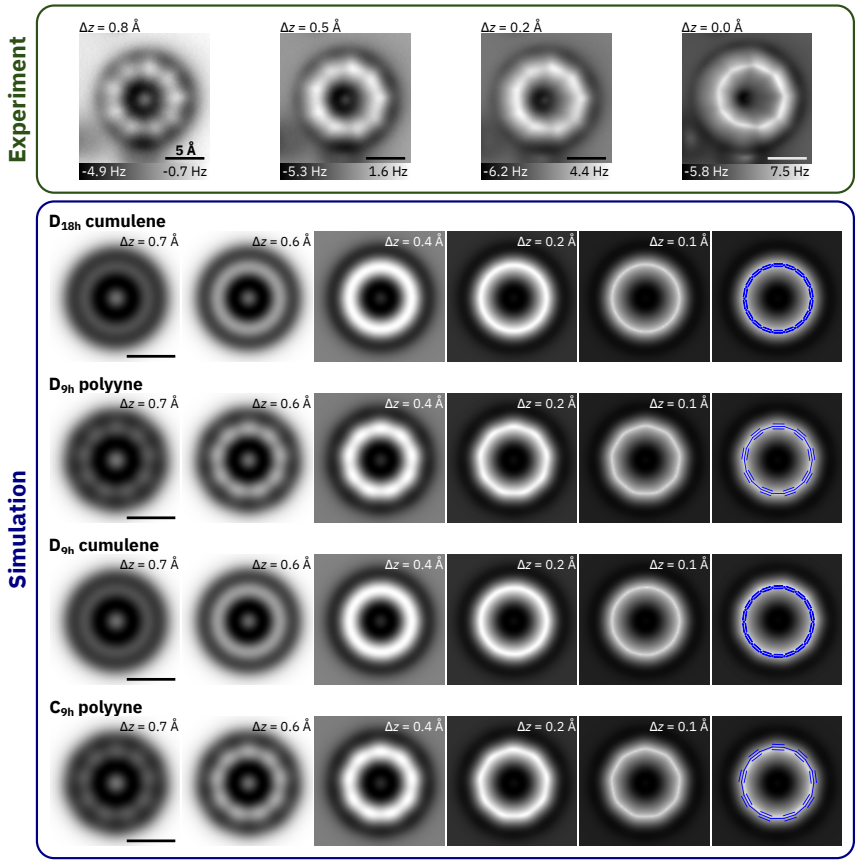


Figure 9.6: **Comparison of experimental and simulated AFM images.** Experimental AFM images of a $C_{18}$ recorded at different tip-sample distances (top row) together with simulated AFM images of four theoretically predicted resonance structures.[171] $D_{18h}$ cumulene with $d_1 = d_2 = 1.30$ Å, $\theta_1 = \theta_2 = 160°$. $D_{9h}$ polyyne with $d_1 = 1.38$ Å, $d_2 = 1.24$ Å, $\theta_1 = \theta_2 = 160°$. $D_{9h}$ cumulene with $d_1 = d_2 = 1.30$ Å, $\theta_1 = 162.9°$, $\theta_2 = 157.2°$. $C_{9h}$ polyyne with $d_1 = 1.38$ Å, $d_2 = 1.24$ Å, $\theta_1 = 163.3.1°$, $\theta_2 = 156.7°$.

For the $D_{9h}$ polyyne geometry with the BLA theoretically predicted in ref. [171] (see also Fig. B.10b in Appendix B), bright lobes are visible at the positions of the triple bonds for 0.6 Å $\leq \Delta z \leq$ 0.8 Å. The differences in the $\Delta f$ signal between the neighboring single and triple bonds in cyclo[18]carbon relate to their respective differences in electron density:

The high electron density of the triple bonds in the imaged plane leads to stronger repulsive tip-sample forces due to Pauli repulsion and thus, brighter contrast in the $\Delta f$ signal compared to the lower electron density regions atop the single bonds. Figure B.10 in Appendix B illustrates how the AFM contrast evolves with different BLA in the $D_{9h}$ polyyne geometry: The larger the BLA, the greater are the differences in electron density between formal single and triple bonds (bond order alternation) and thus, the more pronounced are the differences in the AFM contrast above single and triple bonds. In agreement with this, the bright lobes atop the triple bonds in the AFM simulations at large tip-sample distances (0.8 Å $\leq \Delta z \leq$ 0.5 Å) are most pronounced in Fig. B.10c (largest BLA) and least pronounced in Fig. B.10a (smallest BLA). With the parameters that we used in the PPM simulations, Fig. B.10b fits best to our experimental data.
Simulated AFM images of the $D_{9h}$ cumulene geometry are almost identical to those of the $D_{18h}$ cumulene geometry; the BAA is barely visible (see also Fig. B.11a in Appendix B). For twice the theoretically predicted BAA (11.4°, Fig. B.11b), the changes in the bond angles become apparent as corners in the AFM simulations for small $\Delta z$. However, at larger $\Delta z$ the contrast still resembles that of the $D_{18h}$ geometry. For the BAA of 22.8° (Fig. B.11c) a nine-fold symmetry is already visible at large $\Delta z$, *i.e.*, $\Delta z = 0.7$ Å, where corners can be seen. In contrast to the polyyne geometries, the magnitude of the $\Delta f$ contrast is uniform above the ring. Interestingly, the simulations at small tip-sample distances, *i.e.*, $\Delta z = 0.1$ Å and $\Delta z = 0.2$ Å, are very similar to the contrast of the polyyne geometries exhibiting a nonagon, although the origin of the nonagonal contrast is quite different for cumulene and polyyne. In the $D_{9h}$ polyyne, the nonagonal shape arises because of the different electron densities above single and triple bonds and the corners of the nonagon are located above the positions of triple bonds. In $D_{9h}$ cumulenes, the nonagon relates to the geometry of the molecule and the corners are located above the atom positions at more acute bond angles.
AFM simulations of the $C_{9h}$ polyyne geometry with the theoretically predicted BLA and BAA (see also Fig. B.12a in Appendix B) as well as geometries with twice and four times the BAA (Fig. B.12b, c) show nine-fold symmetry with bright lobes atop the triple bonds at larger tip-sample distances (0.8 Å $\leq \Delta z \leq$ 0.4 Å) that transition into corners for smaller $\Delta z$, similar to the $D_{9h}$ geometry. At larger tip-sample distances (0.8 Å $\leq \Delta z \leq$ 0.5 Å) the lobes appear slightly asymmetric (droplet-shaped rather than oval), with the larger end pointing towards the more acute bond angle, reflecting the prochirality of the molecule. The $C_{9h}$ geometries with different BAA look very similar in the simulated AFM images.
In summary, the differences in BLA between the cumulenic and polyynic structures produce distinct changes in the simulated images, while differences in BAA lead to less pronounced changes. BAA strongly affects the simulated contrast of the $D_{9h}$ cumulene for small tip heights and the contrast of the cumulene with large BAA becomes very similar to those of the polyynes. Nevertheless, the polyyne models can be distinguished from both cumulene models at larger tip height; only the polyynes exhibit nine bright lobes in agreement with the experiment. Thus, both cumulenic geometries of cyclo[18]carbon ($D_{18h}$ and $D_{9h}$) can be excluded. However, the polyyne geometries ($D_{9h}$ and $C_{9h}$) show almost no change in contrast variations as we varied the BAA, which implies that for the polyyne geometries it is challenging to resolve or quantify the extent of BAA from AFM images. Two factors may contribute to this effect: (i) In the cumulenic geometries, the introduction of BAA corresponds to a significant change in symmetry from $D_{18h}$ to $D_{9h}$ (*i.e.*, from 18-fold to 9-fold symmetry). However, in the polyyne geometries, the introduction of BAA corresponds to a more subtle change in symmetry from $D_{9h}$ to $C_{9h}$, both of which are 9-fold symmetric. (ii) The AFM contrast of the polyynic geometries is dominated by strong modulations around the carbon ring, due to the large differences in the electron density between triple and single

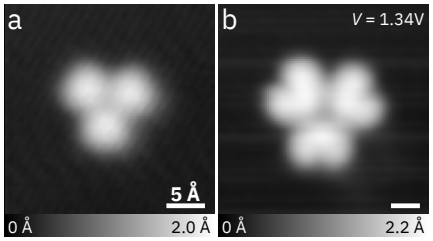


Figure 9.7: **STM images of $C_{18}Br_6$.** (a) In-gap STM image acquired at $I = 1$ pA, $V = 0.4$ V. (b) LUMO density recorded at $I = 1.2$ pA, $V = 1.34$ V. Both STM images were recorded on Xe/Cu(111) with a metal-terminated tip.

bonds, which are enhanced in AFM by relaxations of the CO-tip.[6] On the other hand, BAA affects the position and orientation of the bonds without causing large changes in the electron densities of bonds, resulting in relatively subtle contrast modulations. Hence, although we can be sure that cyclo[18]carbon exhibits a polyynic structure on NaCl, we cannot distinguish between a $D_{9h}$ and $C_{9h}$ geometry.

To test whether the relaxation into the polyynic ground state is favored over the cumulene because of the influence of the underlying NaCl we attempted to investigate the formation of cyclo[18]carbon on a thin insulating film with different symmetry and properties. To this end, a Cu(111) surface was partially covered with closed-packed Xe islands, which are sixfold symmetric. $C_{18}Br_6$ was used since unmasking could be achieved under less harsh conditions compared to the cyclocarbon oxide precursor.
The molecules were found to be very mobile, thus AFM imaging with Xe- as well as CO-terminated tip was not possible. Attempts to remove Br masking groups using bias voltage pulses of up to 3 V were unsuccessful and only resulted in small lateral movement of the precursor. At higher bias voltages the molecules usually jumped away or the cyclic structure was broken, such that it was not possible to evaluate whether tip-induced unmasking was successful. However, while attempts to attain orbital density images on NaCl/Cu(111) resulted in the (partial) unmasking of the molecule, it was possible to address the negative ion resonance of $C_{18}Br_6$ on Xe/Cu(111). Figure 9.7b shows an STM image of $C_{18}Br_6$ recorded at its negative ion resonance ($V = 1.34$ V), revealing the LUMO density.

## 9.4 Charge state determination

The charge state of a molecule can crucially influence its structure.[183] In the neutral charge state, cyclo[18]carbon has 18 electrons in each of the perpendicular $\pi$-systems, which conforms to Hückel's rule. An additional charge would lead to a deviation from this rule, possibly fostering a non-aromatic ground state (polyyne) over an aromatic one (cumulene). It is therefore necessary to determine whether cyclo[18]carbon remains neutral upon adsorption on NaCl/Cu(111).
The charge state of molecules can be inferred by observation of the standing wave patterns of interface-state electrons.[8,51] On NaCl/Cu(111), the Cu(111) surface state survives as an interface state. Scattering patterns of interface-state electrons can be made visible by imaging at low bias voltage.[48] The scattering of interface-state electrons serves as a hallmark for

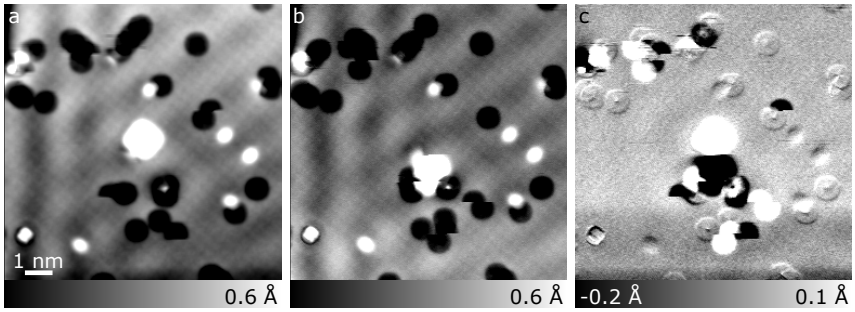


Figure 9.8: **Interface-state scattering behavior of neutral cyclo[18]carbon.** (a), (b) STM images acquired at $I = 0.7$ pA, $V = 0.1$ V before and after moving the (charge neutral) cyclo[18]carbon, in the center of the image, laterally on the surface, respectively. (c) Difference image (a)–(b), exhibits almost no contrast of a standing wave pattern, providing evidence that this molecule was charge neutral. The cyclo[18]carbon molecule and CO molecules that moved between image A and B appear with a white and black contrast at their positions in A and B, respectively.

charged particles because charged adsorbates act as scattering centers while neutral adsorbates do not.[47,51] Figure 9.8a shows an STM image with a standing wave pattern of the interface state visible. Because of scattering at step edges and island edges[48] it is not obvious if the cyclo[18]carbon molecule in the center of the image acts as a scattering center. The molecule was moved laterally, and the same area was imaged again, using the same setpoint (Fig. 9.8b). To emphasize changes in the scattering pattern, caused by moving the molecule, both images were subtracted from each other (Fig. 9.8c). For a charged molecule a pronounced standing wave pattern would be expected in the difference image. The resulting difference image does not exhibit such a standing wave pattern, which evidences that this cyclo[18]carbon is not acting as a scattering center for interface-state electrons and thus is charge neutral.
However, cyclo[18]carbon could be charged and exhibits charge bistability on this surface. This behavior is demonstrated in Fig. 9.9. A change in the charge state of the molecule was deliberately triggered by STM imaging at $V = +0.6$ V and is evidenced by the change

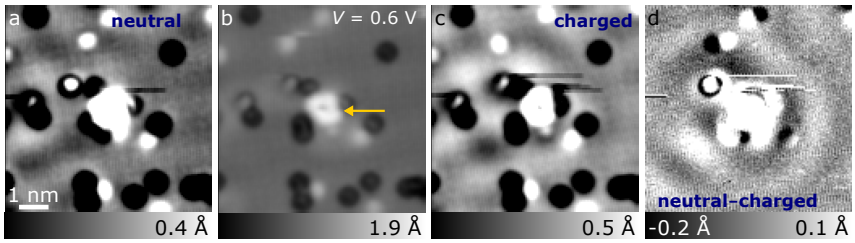


Figure 9.9: **Interface state scattering behavior of charged cyclo[18]carbon.** (a) Image of the neutral cyclo[18]carbon acquired at $I = 0.4$ pA, $V = 0.1$ V. (b) Image of the same cyclo[18]carbon acquired at $I = 0.4$ pA, $V = 0.6$ V, leading to a change in charge state at the scan line indicated by the arrow. (c) Image of the charged cyclo[18]carbon acquired at $I = 0.4$ pA, $V = 0.1$ V. (d) Difference image of (a)-(c) showing an interference pattern, indicating charge-state switching of the molecule.

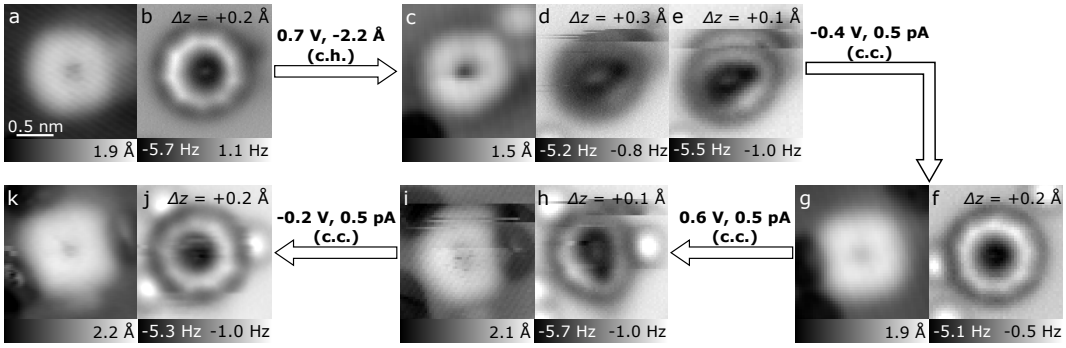


Figure 9.10: **Reversible charge-state transitions of cyclo[18]carbon.** Series of STM (a, c, f, i, k) and AFM (b, d, e, g, h, j) images recorded after charging and discharging events of a cyclo[18]carbon molecule, starting with the neutral molecule (a), (b). Upon applying positive bias voltages $V > 0.6$ V, the molecule could be charged (C-E), upon applying negative voltages the molecule could be switched back into its neutral state (g), (f). It was charged again (i), (h) and switched back to neutral again (k), (j). The arrows indicate how the charge state was manipulated, 'c.h.' indicates that the change in charge state happened during a constant-height image with the given parameters, 'c.c.' indicates that the change occurred during a constant-current STM image at the given parameters. Note the markedly different, less symmetric and less stable AFM contrast of the charged cyclo[18]carbon compared to the neutral one. STM images displayed were recorded at a setpoint of $V = 0.1$ V and $I = 0.5$ pA and $\Delta z$ for the constant-height AFM images displayed is given with respect to that setpoint.

in standing wave pattern of the interface-state electrons. Figure 9.9a shows an STM image of a neutral cyclo[18]carbon, acquired at a setpoint of $I = 0.4$ pA, $V = 0.1$ V. By imaging the same molecule at a bias voltage of $V = +0.6$ V (Fig. 9.9b), an abrupt change in shape occurred, during the scan line indicated by the arrow. Subsequent imaging of the same area, shown in Fig. 9.9c, recorded with the same setpoint as in Fig. 9.9a, shows a change in the standing wave pattern around the molecule compared to Fig. 9.9a. This change is emphasized in the difference image Fig. 9.9d, where the interference pattern around the molecule indicates a change in charge state between Fig. 9.9a and Fig. 9.9c.
Figure 9.10 shows a series of charging and discharging events of an individual cyclo[18]carbon molecule. The molecule was charged by imaging it at voltages $V > 0.6$ V. Presumably, cyclo[18]carbon is charged negatively by resonantly attaching a long-lived electron to its LUMO, in analogy to the reported charge-state switching of CuPc.[47] In contrast to neutral cyclo[18]carbon, the charged molecule exhibits a distorted, less circular geometry (see Fig. 9.10d, e and h). Its structural characterization is even more challenging than for neutral cyclo[18]carbon, as it often changed its adsorption geometry and site, leading to the stripy images observed in Fig. 9.10d, e and h. At voltages $V < -0.2$ V, the molecule was switched back to the neutral charge state reestablishing the 9-fold geometry of neutral cyclo[18]carbon.
Often a change in the charge state of the molecule was accompanied by lateral displacement of the molecule and sometimes chemical reactions with surrounding molecules. The charge bistability and the high reactivity render imaging of the orbital densities of cyclo[18]carbon with STM extremely challenging. As a result of the charging of cyclo[18]carbon at positive bias voltages, the LUMO related resonance cannot be spatially imaged. The threshold for

charging the molecule at about $V = 0.6$ V gives an indication for the onset of the NIR, related to the LUMO, at this voltage. Once the molecule has been charged negatively, the corresponding state remains occupied and is therefore not available as a tunneling path. The next-higher unoccupied state of the singly negatively charged molecule lies higher in energy by the Coulomb energy and can therefore only be addressed by applying markedly higher voltages. Applying voltages larger than 1.5 V for imaging of cyclo[18]carbon has resulted in this molecule reacting with other molecules on the surface in all attempts. Imaging the HOMO density at negative bias voltages was also not possible since imaging at elevated negative bias voltages ($V < -1.5$ V) led to the molecule jumping away.

## 9.5 On-surface covalent bond formation

The high reactivity of cyclo[18]carbon and its oxides makes them promising candidates for on-surface covalent molecular fusion by atom manipulation, of which very few previous examples have been reported.[16] By applying an elevated bias voltage near two proximate molecules covalent bond formation could be promoted and thus fusion of two molecules could be achieved. One example is shown in Figure 9.11, where two neighboring cyclocarbon oxide intermediates, $C_{20}O_2$ and $C_{22}O_4$ (Fig. 9.11a), were fused in this way. After constant-current imaging at a setpoint of $V = 3$ V and $I = 0.5$ pA, the molecules had reacted and formed covalent bonds, as revealed by the AFM resolved structure of the product shown in Fig. 9.11c. A possible reaction mechanism is shown in Fig. 9.11d, showing that, upon scanning with an elevated bias voltage, we could potentially trigger cycloaddition and cycloreversion reactions within the covalent bonds of the molecules. In cycloaddition reactions, unsaturated molecules/parts of molecules generate a cyclic adduct by reducing the net bond order, i.e., $\pi$-electrons move and form $\sigma$-bonds and thereby form a ring. The number of electrons

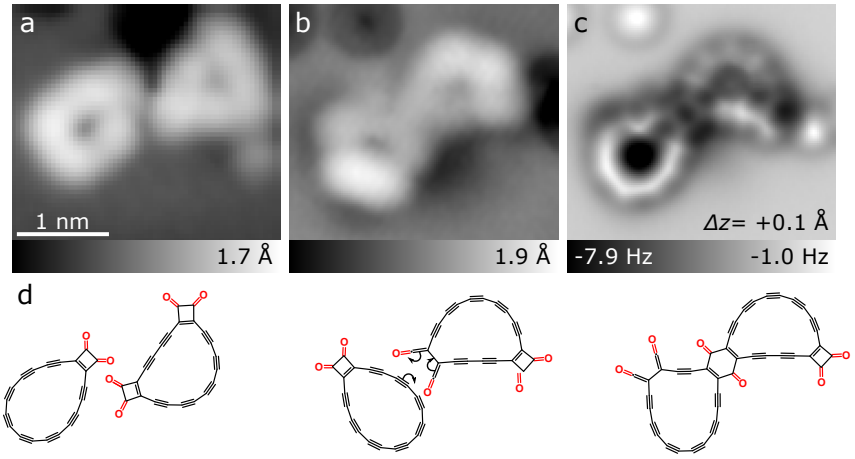


Figure 9.11: **Fusion of two molecules by atom manipulation.** (a) STM image of two neighboring intermediates, identified as $C_{20}O_2$ and $C_{22}O_4$. Imaging the area at constant current (c.c.) with a setpoint of $V = 3$ V, $I = 0.5$ pA resulted in the reaction between the molecules. (b), (c) STM and AFM images, respectively, of the resulting fused molecule. (d) Proposed reaction mechanism. One of the cyclobutene-1,2-dione groups of $C_{22}O_4$ undergoes a [2+2] cycloreversion to form a bisketene moiety. This then undergoes a [4+2] cycloaddition with a triple bond of $C_{20}O_2$ to form the benzoquinone product.

involved in the addition reaction are specified by the addition $[i+j+...]$, with $i$, $j$, *etc.* being the involved electrons of the reacting species, respectively. Reverse cycloaddition reactions are called cycloreversions.[184,185] In the reaction shown in Fig. 9.11, one of the single bonds in the four-membered ring of one of the masking groups was broken (the cyclobutene-1,2-dione groups of $C_{22}O_4$ underwent a [2+2] cycloreversion to form a bisketene moiety). The resulting ketene groups then underwent a [4+2] cycloaddition with a triple bond of $C_{20}O_2$ to form the benzoquinone product. The nonlocality of the process suggests that it is mediated by hot interface-state charge carriers.[176,178–180] For more examples of on-surface reactions see Figs. B.13 and B.14 in Appendix B. These results demonstrate that the high reactivity of the strained polyynic moieties of cyclo[18]carbon and its oxide intermediates fosters covalent coupling by atom manipulation.

## 9.6 Conclusion

In conclusion, we demonstrated the successful synthesis of cyclo[18]carbon by tip-induced on-surface synthesis from two different precursors, namely cyclocarbon oxide $C_{24}O_6$ and bromocyclocarbon $C_{18}Br_6$. The generation of cyclo[18]carbon by debromination of $C_{18}Br_6$ showed a five times greater yield than from $C_{24}O_6$ precursors. Bond-resolved AFM images of $C_{18}$ showed nine pronounced lobes along the carbon chain, indicating a polyynic structure of cyclo[18]carbon adsorbed on NaCl rather than a cumulenic, with the bright lobes being located atop the triple bonds. Comparison with AFM simulations of different geometries of $C_{18}$ showed that BAA can have a considerable effect on the simulated AFM images for the cumulenic structure but is barely visible for the polyyne. The simulations confirm that the cumulene geometries, even those with extreme BAA, can be excluded, corroborating the polyynic structure of $C_{18}$ on NaCl. However, it is challenging to rule out or quantify BAA in the polyynic geometry. Interaction with the surface may affect the molecular structure, and the structure of $C_{18}$ in vacuum might be different from that on NaCl.
On bilayer NaCl on Cu(111) $C_{18}$ was found to be charge neutral. However, charge state switching accompanied by a change in geometry from circular to oval could be observed at negative bias voltage polarities.
Finally, we could demonstrate that the strained polyynic moieties of cyclo[18]carbon and its oxide intermediates allow covalent coupling by atom manipulation, potentially opening the way to create other elusive carbon-rich molecules by atom manipulation.

## Chapter 10

# Investigation of the reduction reaction of vanadyl-phthalocyanine VOPc

*Most of the work presented in this chapter has been published. Text and figures are reprinted and modified with permission from ref. [186]. Copyright (2019) American Chemical Society.*

Since the first observation of Scanning tunneling microscopy-induced luminescence (STML) on single molecules[26] the field has seen significant advancements int recent years[27,78,82] with astounding resolution not only spatially but also energetically.[28,29,79] However, whether an electronic/vibronic intramolecular transition is fostered can substantially depend on the exact environment like, *e.g.*, the adsorption position.[187–189] Likewise, changes in the molecular geometry and chemical structure, like conformation or the presence/absence or substitution of specific moieties, can intrinsically alter a molecule's optical properties.[82,189] Yet, combining structural and optical information like exciton energies in molecules remains challenging. Since STM is sensitive to the electronic structure, STML is ideally suited for probing optoelectronic properties of single adsorbed molecules, *i.e.*, imaging the densities of molecular frontier orbitals and measuring fundamental gaps[8,190,191] and exciton energies.[27,29,78,81,83] High-resolution atomic force microscopy (AFM), on the other hand, is highly sensitive to the forces between probe and substrate. This allows measuring the structure of molecules[5,6] and their adsorption geometry, including conformation,[183] adsorption orientation, site and height.[65] Accordingly, AFM is ideally suited to investigate the intermediates and products of on-surface reactions[23,192–194] and reactions triggered by atom manipulation.[16,19,21,195] The combination of AFM with STML therefore enables the investigation of the change in a molecule's optoelectronic properties throughout a chemical reaction. In addition, atomically precise assignment of symmetry axes of allowed radiative transitions to the molecular structure could be facilitated by overlaying STML maps with high-resolution AFM images.[108] The effect of adsorption height as well as adsorption position on the quenching of the radiative decay is accessible as well for suitable molecules, *i.e.*, molecules with different stable adsorption conformations. Combining both techniques is therefore a promising route to link atomically resolved structural information with optical properties of individual molecules.

Phthalocyanines (Pc) are well-characterized because of their widespread use in organic light-emitting diodes and photovoltaics,[196–198] making them an excellent model system for STML experiments.[28,29,78,81,82] Since they offer the possibility of induced on-surface chemical reactions, metal-oxide Pc are potentially interesting to investigate the influence of reduction on their electronic and optical properties.
In this context, single vanadyl-phthalocyanine (VOPc) molecules decoupled from a Ag(111)

substrate by an ultra-thin NaCl layer were investigated in a a combined AFM and STML study, allowing for detailed structure determination with atomic resolution and controlled atom manipulation conjunct with the investigation of optoelectronic properties. The reduced counterpart of VOPc, vanadium-phthalocyanine (VPc), could thus far not be synthesized by standard solution chemistry. It is therefore inaccessible to standard optical characterization techniques, while VOPc has already been characterized.[199,200]
We were able to specifically dissociate the central oxygen using atom manipulation.[15,20,23,201,202] The successful reduction of VOPc to VPc could be confirmed by high-resolution AFM structural elucidation. In STML spectra, VOPc showed a characteristic light emission at 682 nm, while no light emission was detected from VPc.

## 10.1 Methods

VOPc molecules were deposited onto the cold ($T = 10$ K) NaCl(2ML)/Ag(111) sample *via* thermal sublimation from a Si-wafer that was flash-annealed to approximately 900 K within a few seconds. Since the aim was to perform STML experiments, the presented results are obtained from molecules adsorbed on bilayer NaCl, which is necessary for decoupling. All AFM images were recorded with CO-functionalized tips. STML spectra were recorded in an energy range of $1.28 - 3.07$ eV ($404 - 969$ nm) and $1.18 - 2.53$ eV ($491 - 1054$ nm) and by averaging over several frames, where each frame typically lasted 3 to 4 minutes, yielding total acquisition times per spectrum between 8 and 60 minutes. The shown spectra are background corrected.

## 10.2 Characterization of vanadyl-phthalocyanine.

After deposition we found molecules of two different appearances on Ag(111) as well as on bilayer NaCl (Fig. 10.1b, first and second column) with approximately equal occurrences. The two species can be identified as the two possible adsorption conformations of VOPc[203–205] distinguished by their appearance in AFM and STM with a CO-functionalized tip (Fig. 10.1b and c). From the AFM images, they can be assigned to a conformation with the central oxygen atom pointing away from the surface (O-up) and towards the surface (O-down), respectively.[203–205] For the O-up conformation, only the outermost phenylene groups can be resolved by AFM while in the center it exhibits an extended repulsive feature stemming from the central oxygen sticking out of the surface plane. In the O-down conformation, the full macrocycle, *i.e.*, the cyclic porphyrin core of the molecule, can be resolved by AFM. For small tip-sample distances, the core of the macrocycle becomes distinctly more repulsive than the phenylene groups, indicating that the macrocycle is not fully planar but rather dome-shaped. This can be rationalized by the adsorption geometry: Because of the oxygen pointing towards the surface in the O-down conformation, the macrocycle is pushed away from the surface in the center and bends slightly down at the outer part. In both conformations, the molecule adsorbs with the center on a Na-site (Fig. 10.1d).
The reduced species VPc, shown in the right column in Figure 10.1, can be generated from VOPc O-up by atomic manipulation, as described in the following.

## 10.3 On-surface synthesis of VPc from VOPc by atom manipulation

Synthesizing VPc is known to be challenging as it immediately oxidizes to the more stable VOPc in oxygen containing environments. As of yet, its synthesis has only been achieved by Eguchi *et al.* by on-surface metalation of free-base Pc in UHV-environment.[206] An alternative route to synthesize VPc is the controlled reduction of single VOPc molecules by SPM-based atom manipulation. In this approach, the highly localized nature of the electric field and/or tunnel current between tip and molecule is exploited.
We found that the reduction reaction could be actuated reliably. To that end, we first positioned the tip above the center of a VOPc O-up at a setpoint of $V = -2$ V, $I = 0.5$ pA and then retracted the tip by about 2 Å. Next, the sample voltage was ramped from $-2$ V to $-4$ V, resulting in currents on the order of 10 to 100 pA, and held constant for up to 30 s while the tip position was kept fixed. To monitor whether and when a reaction occurred, tunnel current $I$ and frequency shift $\Delta f$ were recorded simultaneously. The dissociation of the oxygen usually occurred after a few to a few tens of seconds and was accompanied by a sharp drop in current and increase in $\Delta f$, as shown in Figure 10.2 for one exemplary reaction. Subsequent imaging with AFM confirmed the structural change (see Figure 10.1c); the molecular structure is clearly different from both observed VOPc conformations. Similar to VOPc O-down, the full macrocycle can be resolved by AFM. However, the outermost phenylene groups appear distinctly brighter compared to the central part. In the center, a bright, cross-shaped feature is visible in the AFM images, a similar contrast as has also been observed on other metal phthalocyanines like FePc.[207,208]

To quantify the non-planar adsorption geometries of the molecules, we performed force-

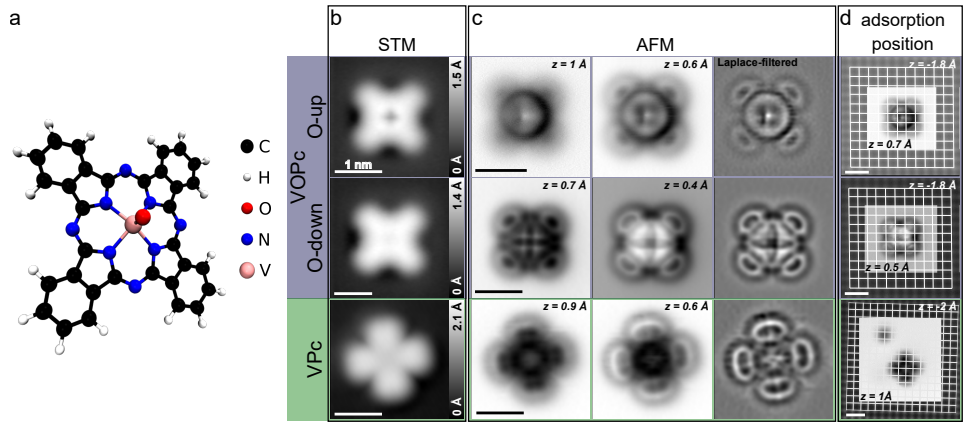


Figure 10.1: **Structure of VOPc and VPc.** (a) Ball-and-stick model of VOPc. (b)-(c) Images of VOPc in O-up (left column) and O-down (central column) conformation and VPc (right column) acquired with (b) STM with CO-functionalized tip and (c) AFM at different tip heights. (d) AFM data resolving the adsorption position of VOPc O-up and O-down and VPc on bilayer NaCl. The grid indicates the Cl-sites, which are resolved in the outer regions of the images by using a decreased tip height $z$. STM images were acquired at a setpoint of $V = 0.2$ V and $I = 0.5$ pA. $z$ indicates the tip height relative to the STM setpoint. Positive $z$ correspond to an increased tip-sample distance.

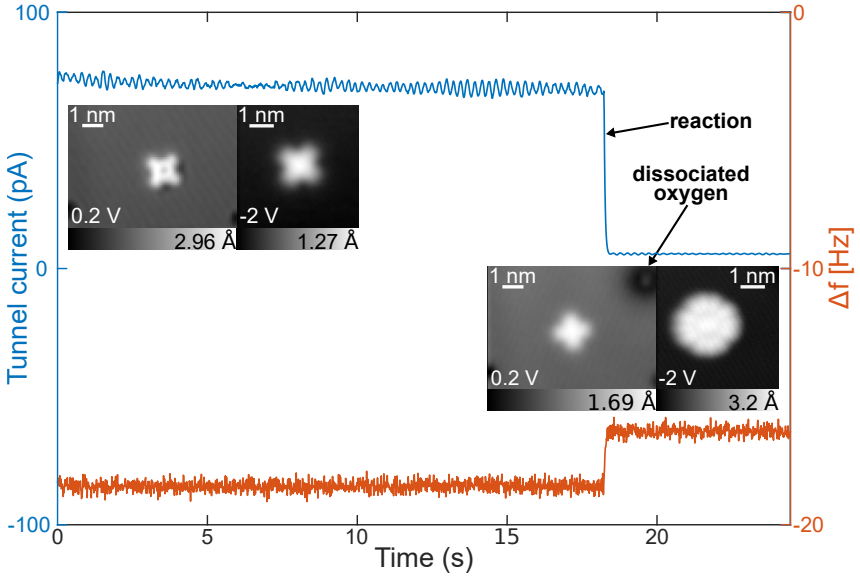


Figure 10.2: **Reduction of VOPc *via* atom manipulation.** Tunnel current $I$ and frequency shift $\Delta f$ recorded over time during the reduction of a VOPc in O-up conformation at $V = -4$ V. The reaction is accompanied by a sharp drop in tunnel current and increase in $\Delta f$. The insets show constant-current STM images ($I = 0.5$ pA) before and after the spectrum was obtained.

distance spectroscopy [$\Delta f(z)$], yielding the tip height $z^*$, *i.e.*, the tip height at which the minimum $\Delta f(z)$ is reached.[65] This allows determining differences in the adsorption height within a molecule, allowing inferences on the adsorption geometry. To this end, $\Delta f$ was recorded as a function of tip height $z$ at different positions atop the molecules, *i.e.*, above the center of the macrocycle and one of the phenylene groups at the periphery of the molecule, respectively, as indicated in the inset in Figure 10.3. In the resulting $\Delta f(z)$-curve $z^*$ is identified using a parabolic fit to the data around the minimum. Figure 10.3 shows the recorded $\Delta f(z)$-spectra and the corresponding $z^*$ for the different species, *i.e.*, VOPc O-up, VOPc O-down and VPc.

To draw conclusions on the adsorption geometry, the $z^*$ obtained at different positions within the molecule, *i.e.*, the center of the macrocycle $z_c^*$ and one of the phenylene groups at the periphery $z_p^*$, were compared[a]. The difference in $z^*$ between both positions, in combination with the contrast in the AFM images, provides a measure for the shape of the molecule. Table 10.1 summarizes $z^*$ determined with a CO-functionalized tip above a phenylene group ($z_p^*$) and the center ($z_c^*$) of the molecules as well as the relative difference in height of both positions ($\Delta z^* = |z_c^*| - |z_p^*|$) for all three species. For the error of $z^*$, we follow the error estimation of Ref. [65] of around 0.05 Å.

For VOPc O-down, $z_c^*$ is larger than $z_p^*$, corroborating the finding from the AFM image in Figure 10.1b that the molecule is dome-shaped. After the reaction, the bright appearance

[a]Note that, since the distance dependence of the frequency shift gives a chemical contrast/is sensitive to chemical properties and the atomic species of the different positions are dissimilar (C in the phenylene group, V/O in the center of the macrocycle), an exact one-to-one comparison of the adsorption height is not possible. However, in combination with high-resolution AFM images, a qualitative conclusion on the geometry/shape of the molecule is possible.

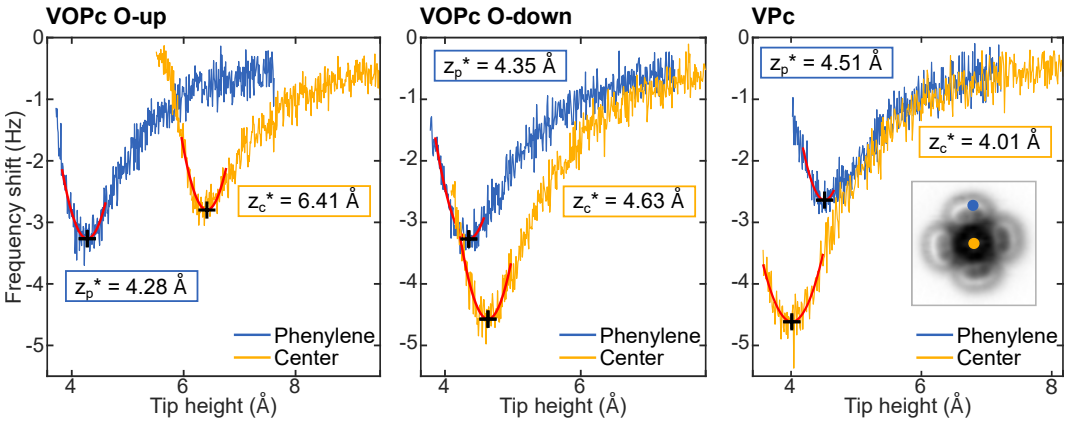


Figure 10.3: **Force-distance spectroscopy on VOPc and VPc.** Data was obtained on VOPc O-up (left), VOPc O-down (center) and VPc (right) with a CO-functionalized tip. The tip height $z$ is given with respect to the STM setpoint of $I = 0.5$ pA and $V = 0.2$ V on bilayer NaCl (next to the molecule). The spectra were recorded above one of the phenylene groups (blue) as well as the center (orange), as indicated in the inset. Around the minimum of $\Delta f(z)$, the curve is fitted using a parabolic fit-function (red) to obtain the relative tip height corresponding to the minimum in $\Delta f(z)$, *i.e.*, $z^*$, indicated by the black cross. The corresponding $z^*$ for the different tip positions are given in the insets in the plots.

Table 10.1: $z^*$ **for VOPc O-up, VOPc O-down and VPc.** $z^*$ for the different molecular species (VOPc O-up, VOPc O-down and VPc) was determined from the $\Delta f(z)$-curves atop a phenylene group ($z_p^*$) and the center ($z_c^*$) and the respective height difference ($\Delta z^*$) between the two positions.

| | $z_p^*$ (Å) | $z_c^*$ (Å) | $\Delta z^*$ (Å) |
|---|---|---|---|
| VOPc O-up | 4.28 | 6.41 | 2.13 |
| VOPc O-down | 4.35 | 4.63 | 0.28 |
| VPc | 4.51 | 4.01 | -0.5 |

of the phenylene groups and the dark center in the AFM image indicate a clear change in the molecule's shape. This is confirmed by force-distance spectroscopy, showing that indeed the phenylene groups are further away from the surface than the center of the molecule ($z_c^* < z_p^*$). This finding agrees with the expected change in the molecular geometry upon dissociation of the central oxygen. In addition, Figure 10.1d and the inset in Figure 10.2 show a newly arisen defect in the vicinity of the molecule after the reaction, presumably the dissociated oxygen atom, which is adsorbed on a Cl-Cl bridge-site. For these reasons, we exclude a mere switching behavior between the O-up and O-down conformation.[205]
Investigation of the adsorption position reveals that after the reaction, the molecule has rotated in-plane by about 45° and moved laterally such that now its center is located on a Cl-site (see Figure 10.1d). The AFM images of VPc (Figure 10.1c, right column) show the phenylene groups with an apparently increased diameter and bond-like features appearing in the center of the rings. We assign this contrast to two different energetically degenerate, mirror symmetric adsorption orientations in which the symmetry axes of the molecule are rotated by a few degrees with respect to the symmetry axes of the surface. The adsorption

orientation is switched under the influence of the tip, preferring the orientation in which an outer ring is located under the tip. The apparent bond-like features arising within the rings appear at the tip positions at which the molecular orientation switches.[21,25,209] This shuttling motion is already well-known for certain metal-phthalocyanines adsorbed on different surfaces.[82,210]

## 10.4 STML on VOPc and VPc

Even though there generally is no one-to-one correspondence between the electronic transitions probed by STS and the allowed optical transitions, in STML they are often closely related. Measuring the differential conductance thus can yield valuable information that complement the characterization of a molecule's optical properties.
Figure 10.4a displays STS and STM data of the three different molecular species, *i.e.*, VOPc in O-up and O-down conformation as well as VPc. The energy levels of VOPc O-up and O-down are shifted with respect to each other. We tentatively explain this shift by a concurrence of several effects: i) The electrostatic dipole of the molecule, related to its partial negative charge accumulation at the oxygen, shifts both resonances to higher (lower) energies in the O-down (O-up) adsorption conformation. ii) The increased adsorption height of the macrocycle in the O-down conformation will lead to an increased relative voltage drop across the NaCl film[8,39] and thus to an up-shifted negative ion resonance (NIR) and a down-shifted positive ion resonance (PIR) compared to the O-up conformation. Both effects work in the same direction in the case of the NIR, explaining its significant up-shift for the O-down conformation with respect to the O-up conformation. In case of the PIR, which is found at similar energies for both conformations, the effects work in opposite directions. iii) In addition, we cannot exclude shifts in the energies due to strain in the different adsorption geometries[189] as well as a different response and reorganization of the NaCl due to the different adsorption geometries.[41,211,212] The spatial distribution of the molecular orbital densities in VOPc in O-up and O-down conformation is very similar, though (Fig. 10.4b). Slight variations are only present in the center of the molecule, where the VO-group is pointing in opposite directions.
After reduction of VOPc to VPc, also the electronic structure of the molecule has significantly changed (Figure 10.4). The spatial distributions of both HOMO and LUMO density look distinctly different compared to VOPc in either conformation. Additionally, the PIR for intact VOPc in both conformations is found at voltages below $-2$ V. In contrast, the reduced VPc exhibits a PIR already at around $-0.7$ V. Hence, imaging at bias voltages between $-0.7$ V and $-2$ V serves as a fingerprint to differentiate between VPc and VOPc, as shown in the insets in Figure 10.2.

To investigate whether the observed changes in adsorption geometry and electronic structure also affect the molecule's optical properties as VOPc is reduced to VPc, we recorded STML spectra on both species. The STML spectra on pristine VOPc in O-up conformation show a single peak at 682 nm (1.82 eV) for sample bias voltages $V < -2.4$ V with the tip positioned atop one of the extremities of the macrocycle (Figure 10.5a). The excitonic emission stems from a radiative transition from the degenerate Q-band to the ground state and is in good agreement with experimental results for the energy of the Q-band transition in (dissolved) VOPc.[199,200] Light emission could only be observed above VOPc in the O-up conformation, since for O-down it was not possible to establish stable conditions, *i.e.*, the molecule would always jump to the tip or away for high bias voltages and currents, which would both be

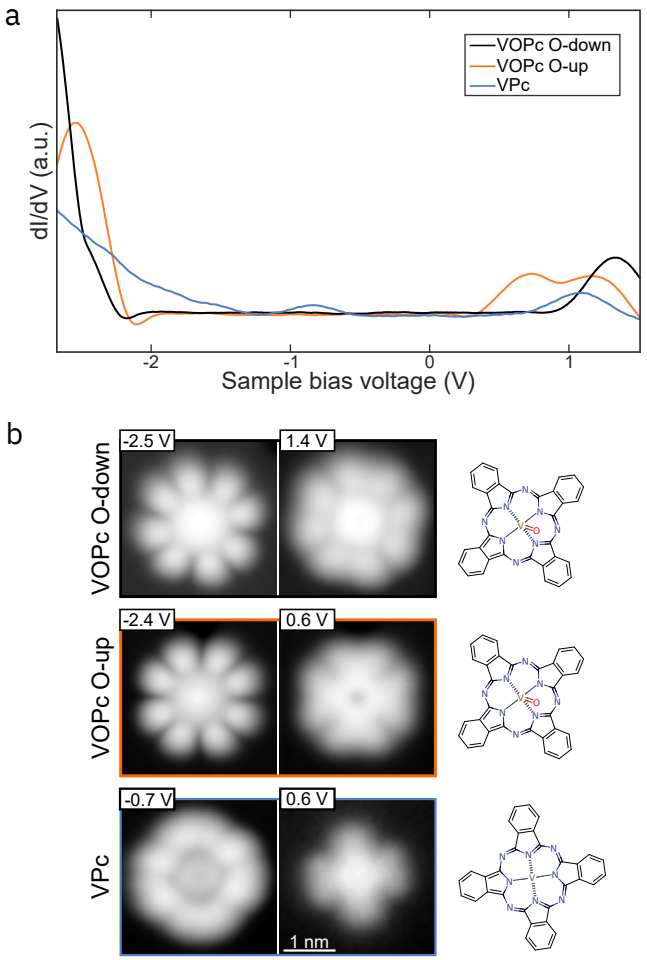


Figure 10.4: **STS on VOPc and VPc.** (a) Differential conductance curves recorded on VOPc in O-up (red) and O-down (black) conformation and VPc (blue). (b) Orbital densities corresponding to the HOMO at negative and the LUMO at positive voltages of the three different species, measured with a metallic tip. The structure drawings indicate the orientation of the molecules.

needed for inducing as well as detecting molecular luminescence on bilayer NaCl.
After the dissociation of oxygen from VOPc O-up, no emission was observed on the product anymore, independent of the position of the tip above the molecule. Figure 10.5b shows a direct comparison of the molecular luminescence recorded with the tip positioned above one of the extremities of a VOPC O-up before and after its reduction using the exact same tip as well as the same STM setpoint and spectrum acquisition parameters. The peak at 682 nm, which is clearly visible in the spectrum recorded on VOPc (Figure 10.5b, left spectrum), disappeared in the VPc-spectrum (Figure 10.5b, right spectrum). Also, no energetically shifted photon emission is detected on VPc for energies down to the near infrared of 1.2 eV. Taking spectra at different applied bias voltages ($-1.5$ V to $-2.7$ V and 2 V to 2.4 V) neither led to a detectable signal in the emission. The absence of detectable luminescence could either indicate that the exciton formation in VPc is quenched or hindered, or that the

radiative decay path is quenched compared to the situation in VOPc.

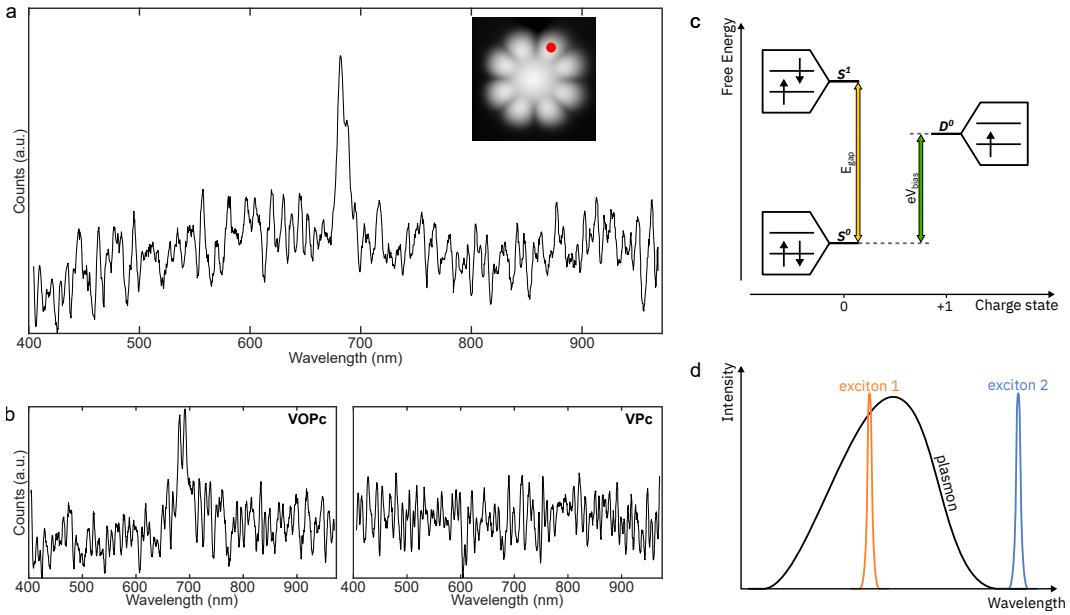


Figure 10.5: **STML on VOPc and VPc.** (a) STML spectrum recorded on a phenylene group of a VOPc (O-up) ($V = -2.6$ V, $I = 350$ pA). (b) Comparison of STML spectra recorded on a phenylene group of a VOPc before and after tip-induced reduction, using the exact same tip and parameters ($V = -2.4$ V, $I = 150$ pA). (c) Scheme with the relevant many-body transitions for the charge-transfer mediated exciton formation for 0 V applied bias voltage. In order to transiently form the cation ($D^0$) upon removal of an electron from the molecule to the tip, the respective energy difference depicted by the green arrow, a sufficient bias voltage has to be applied. A transition from $D^0$ to $S^1$ upon attachment of an electron from the sample to the molecule is only possible if through this transition the free energy is minimized, *i.e.*, if $D^0$ is higher in energy than $S^1$. The depicted scheme is simplified and does not take into account the potential drop within the NaCl spacer layer between molecule and metallic substrate. (d) Schematic illustration of the change in plasmon-exciton coupling for different exciton energies, denoted by 'exciton 1' and 'exciton 2'. Exciton 1 overlaps with the NCP spectrum, hence, excitation via a plasmon-mediated energy transfer is possible and the radiative decay of the exciton is enhanced because of the Purcell effect. Exciton 2 has no overlap with the NCP spectrum and hence, plasmon-exciton coupling is weak and radiative transitions within the molecule are not enhanced.

Figure 10.5c and d illustrates potential explanations for the absence of luminescence. A charge-injection mediated process (Fig. 4.2) is closely linked to the energetic positions of the molecule's PIR/NIR. Figure 10.5c schematically shows a simplified many-body energy diagram with the singlet ground and excited state ($S^0$ and $S^1$) as well as the transient cationic ground state ($D^0$). In order to charge the molecule transiently positively from the tip, a sufficient bias voltage needs to be applied. A transition from $D^0$ to $S^1$ upon electron attachment from the sample is only possible if the free energy is reduced in this process, *i.e.*, if $eV_{bias} > E_{gap}$. The depicted energy diagram does not account for the potential drop within the NaCl spacer layer between molecule and metallic sample. For a more sophis-

ticated consideration this has to be taken into account, however, the simplified picture is sufficient for a qualitative assessment.
Upon reduction, the PIR of VOPc shifts closer to the electrochemical potential of the sample, meaning that less energy is required to attach a hole to the PIR compared to VOPc. This could lead to the situation depicted in Fig. 10.5c, where a subsequent charge transfer from the sample resulting in the electronically excited $S^1$ state is not possible any longer.
On the other hand, the decrease in fundamental gap upon reduction of VOPc observed in STS (Fig. 10.4a) could indicate a concurring red-shift of the exciton energy which in turn could affect the plasmon-exciton coupling, as illustrated in Fig. 10.5d[b]. Here, the energy of exciton 1 has a large overlap with the NCP spectrum. Hence, the exciton can be excited via a plasmon-mediated energy transfer and its radiative decay is enhanced as a consequence of the Purcell effect. Exciton 2, however, has a vanishing overlap with the NCP spectrum, so excitation via plasmon-mediated energy transfer is unlikely and the radiative decay channel is not fostered over other possible decay mechanisms. Figure C.1 in Appendix C shows the NCP resonance recorded on the bare bilayer NaCl. As indicated, at the position of the exciton energy of VOPc ($\approx$ 680 nm) there is still considerable intensity detected. For larger wavelengths, however, the intensity of the NCP resonance is decreased considerably. Thus, a potential red-shift in exciton energy upon reduction of VOPc could significantly reduce the coupling between NCP and exciton, which would result in a strong quenching of radiative transitions in VPc compared to VOPc. However, the exciton energy is challenging to quantitatively deduce from the change in fundamental gap, since a direct general correlation is not given. Optical transitions are governed by symmetry and optical selection rules and, furthermore, many-body effects can have significant impact on both the involved energies and orbitals.[191,213,214] In metal Pc, the Q-band emission is driven by a transition between the ground state of $A_{1g}$ symmetry and the first excited state of $E_u$ symmetry of the orbitals delocalized over the macrocycle ($\pi - \pi^*$).[215,216] The energy of this transition is usually only slightly affected by a change in the metallic center.[217–219] This might indicate that the change in exciton energy in VOPc driven by the reduction of its metal oxide center is smaller than the change in fundamental gap of 1 eV might suggest.
Quenching of the radiative decay channel could also be caused by changes in the environment or geometrical changes within the molecule.[82,187–189] A change in adsorption site for example, as observed for the reduction from VOPc to VPc, could significantly alter the relative likelihood of different decay pathways. This could facilitate a non-radiative decay of the molecular exciton, quenching the luminescence to below our detection limit.

## 10.5 Conclusion

We demonstrated that by a combination of AFM and STML the investigation of changes in excitonic emission by a chemical reaction becomes feasible. As a model system we used single VOPc molecules adsorbed on NaCl(2ML)/Ag(111). Using atom manipulation, we were able to deliberately reduce VOPc to form VPc, which was confirmed by AFM atomic resolution imaging, adsorption site determination and force-distance spectroscopy, and compare the emission characteristics before and after the chemical reaction using STML. While for VOPc a peak at 682 nm (1.82 eV) was detected, no light emission was detected on

[b] It is also possible that excitonic emission in VPc occurs below our minimal measured energy of 1.2 eV. However, such pronounced changes in exciton energies in metal centered phthalocyanines upon change of the metallic center is unlikely, as explained later in the text.

VPc. Based on STS measurements on the different molecules, we relate this to a shift in energies of the molecular resonances with respect to the electrochemical potential. Possible explanations for the absence of excitonic emission after reduction to VPc are the energetic hindrance for the $D_0$ state of the cation to decay into the $S_1$ state of the neutral molecule by electron transfer from the substrate (charge-injection mediated process), a quenching of radiative decay (plasmon-mediated process) or a shift of the exciton energy out of our optical detection window.

The combination of AFM with STML allows linking a molecule's structure with its opto-electronic properties. This approach can be extended using Kelvin probe force microscopy (KPFM), to incorporate also the internal charge distribution, charge state or dipole moment. Exploiting the AFM's capabilities for precise atom manipulation, this can be used to investigate the change in a molecule's properties induced by a chemical reaction. Because of the low temperature and UHV environment, this provides access to the properties of molecules that cannot be synthesized by standard solution chemistry or where standard optical characterization is not possible, as shown for VPc. Moreover, STML could assist AFM in the identification of molecules within complex molecular mixtures[128,133,220] by providing complementary information on the same individual molecule.

# Summary

The pivotal idea behind this thesis was to use on-surface synthesis by atom manipulation to investigate the influence of certain chemical reactions on the general properties of a single molecule as well as to generally use it to form and study novel molecules. In addition, we extended our toolbox by taking first steps in combining high-resolution AFM with STML.

Chapter 8 focuses on identifying structures and recurring structural motifs in complex molecular mixtures, *i.e.*, incipient and primary soot, demonstrating the applicability of high-resolution AFM as a method to complement standard analytical techniques like mass spectrometry and NMR in fields other than surface science. We could identify a large complexity of molecular structures ranging from small aliphatic chains to large PAHs, suggesting that aliphatic moieties play a vital role in the physical agglomeration of PAHs during the soot formation process. The abundance of methylene groups in the imaged molecules as well as the presence of molecules with $\pi$-radical character could indicate that $\pi$-radicals are important in particle inception. They could lead to bond formation between aromatics in primary soot, whereas in incipient soot the molecules should be mainly held together by weak vdW forces. Our results helped to shed light on some of the processes present in soot formation.

The goal of the experiments described in chapter 9 was to form and characterize a purely *sp*-hybridized carbon allotrope (cyclo[18]carbon). Cyclo[18]carbon is highly reactive and has thus not been stably isolated nor characterized before. The prevalent conditions in the microscope, *i.e.*, low temperature, UHV and an inert surface as a support for the molecule can foster its stability after an *in situ* synthesis. Two different precursors (cyclocarbon oxide $C_{24}O_6$ and bromocyclocarbon $C_{18}Br_6$) were used for the formation of cyclo[18]carbon. By tip-induced unmasking we could form several intermediates, *e.g.*, $C_{22}O_4/C_{18}Br_4$ and $C_{20}O_2/C_{18}Br_2$, as well as cyclo[18]carbon with a total yield for the complete unmasking of the bromocyclocarbon precursor being about five times higher compared to the one of cyclocarbon oxide (64% *vs.* 13%). By comparison of experimental and simulated AFM images of different proposed ground state symmetries with varying degree of bond length alternation and bond angle alternation we found that cyclo[18]carbon exhibits a polyynic ground state. However, we cannot distinguish between structures with and without bond angle alternation. In addition, we found that on bilayer NaCl on Cu(111), cyclo[18]carbon exhibits a bistable charge state and charging is accompanied by a distortion of the circular geometry. Because of its high reactivity, cyclo[18]carbon was expected to be a suitable candidate for tip-induced on-surface intermolecular coupling. Indeed, we could trigger covalent bond formation between close-by cyclo[18]carbon molecules/precursors. However, *i.a.* because of their high mobility on bilayer NaCl, bond formation could not be triggered in a controlled or directed way.

In chapter 10, we demonstrate first measurements combining high-resolution AFM and STML on molecular systems. The presented experiments aimed at investigating how the optoelectronic properties of a metal-oxide phthalocyanine, in this case VOPc, change upon tip-induced reduction (*i.e.*, dissociation of oxygen). Intact VOPc shows a peak in STML

at 1.82 eV, which is in agreement with the expected energy of the Q-band emission. Upon reduction, adsorption position and height change, increasing the interaction between the molecule and the substrate. In addition, NIR and PIR shift up in energy compared to the intact molecule. The change in adsorption could lead to a different degree of luminescence quenching in STML, while a shift in ion resonances could hinder $S_1$ exciton formation by charge injection from the substrate to the molecule. Either way, STML from the reduced species VPc could not be observed.

**Outlook**

On-surface synthesis, especially by atom manipulation, together with the characterization toolbox that is provided by high-resolution SPM is a key instrument for gaining a deeper understanding of bond breaking and formation. The demonstrated tip-induced fusion of molecules (cyclocarbon precursors) on NaCl indicates that the generation of larger carbon rich organic structures on insulators is feasible. Improving the control and versatility in such tip-induced synthesis might allow us to build up and control atomically defined complex model systems to explore fundamental processes like bond formation with ultimate spatial resolution and deepen our understanding of the codependence of geometric and for example optoelectronic properties.

The combination of luminescence measurements and AFM is highly promising since it allows for the investigation of the influence of geometrical and chemical changes on the luminescence properties of dyes. A wider understanding of these dependencies can lead to a more sophisticated understanding on how luminescence properties can be controllably manipulated. On the long run, this is crucial for organic LEDs or organic photovoltaics to not only understand the influence of certain defects or 'imperfections' but to eventually design them to improve material properties.

# Appendix

## Appendix A

# Identification of single molecules

Figures A.1 and A.2 show different observed structures containing five-membered rings at different characteristic positions. The position of the five-membered ring within the molecular structure as well as the hybridization of the C-atoms in the five-membered ring can indicate certain formation mechanisms of those molecules and might foster certain growth/agglomeration mechanisms.

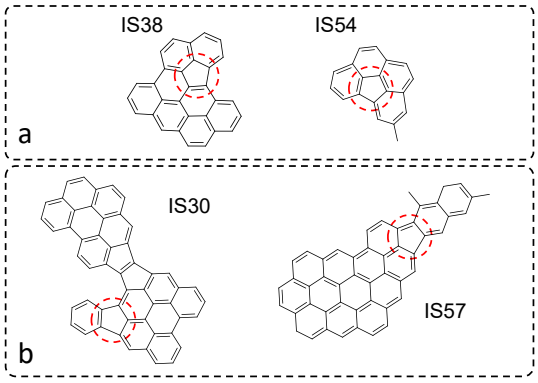


Figure A.1: **Chemical structures of molecules with internal five-membered rings.** (a) Molecules incorporating benzo[*ghi*]fluoranthene-type moieties. (b) Molecules incorporating fluoranthene-type moieties.

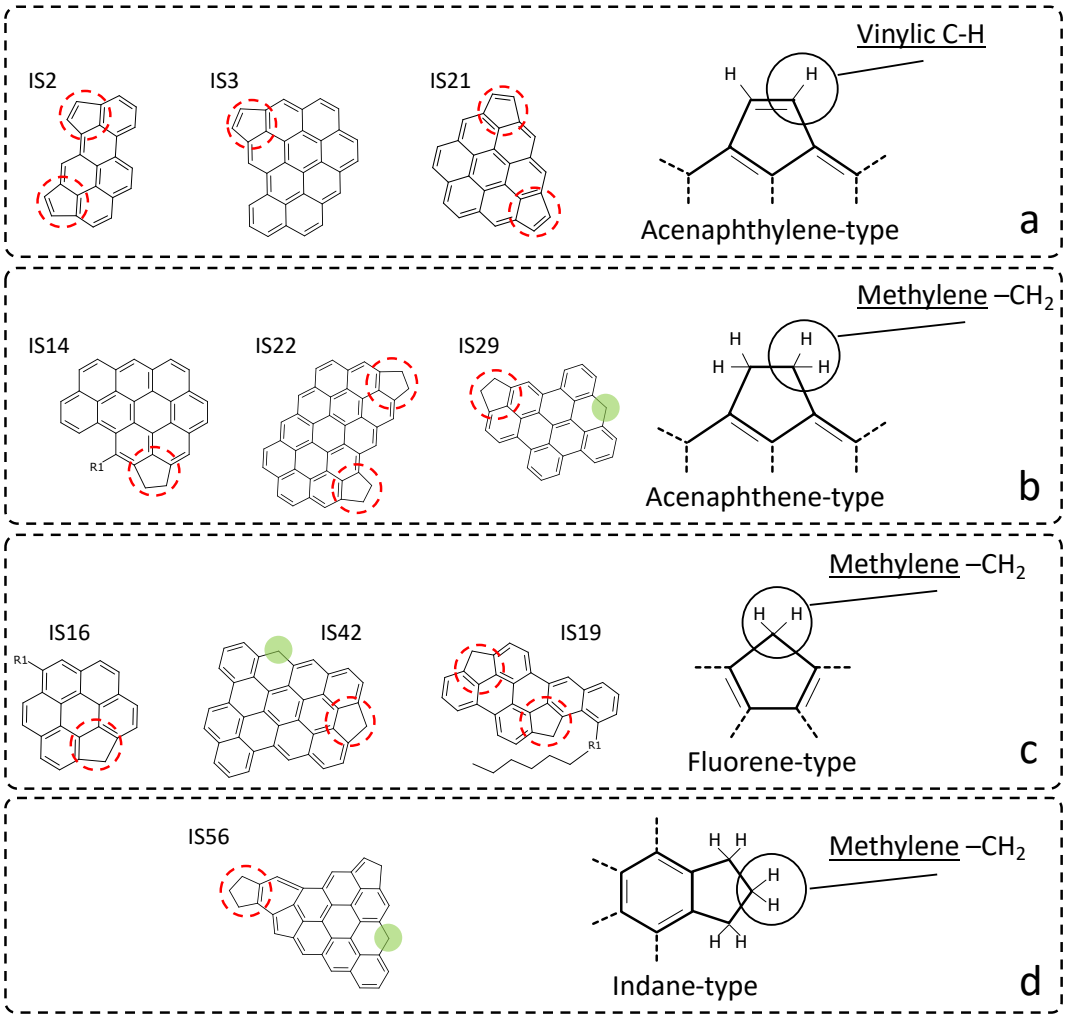


Figure A.2: **Chemical structures of molecules with peripheral five-membered rings.** (a) Molecules incorporating acenaphthylene-type moieties; (b) molecules incorporating acenaphthene-type moieties; (c) molecules incorporating fluorene-type moieties; (d) molecules with indane-type moieties. Dashed red circles indicate the positions of the five-membered rings, green dots indicate the position of methylene groups on peripheral benzenoid rings.

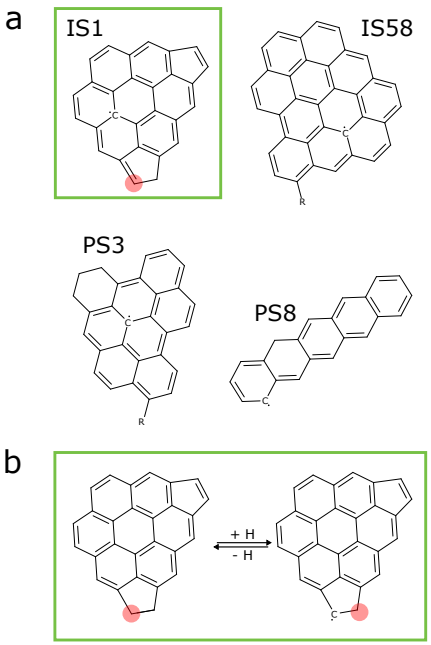


Figure A.3: **Molecules with radical character.** (a) Proposed structure of imaged molecules with radical character. Note that multiple resonant structures are possible for all radicals depicted here. (b) Possible mechanism for the formation of a $\pi$-radical (forward reaction, one hydrogen is removed from the $\pi$-system resulting in a $\pi$-radical $+H_2$) and a methylene group (backward reaction, one hydrogen is added to the $\pi$-radical) in **IS1**. The carbon atom where a radical could have been formed is highlighted in red.

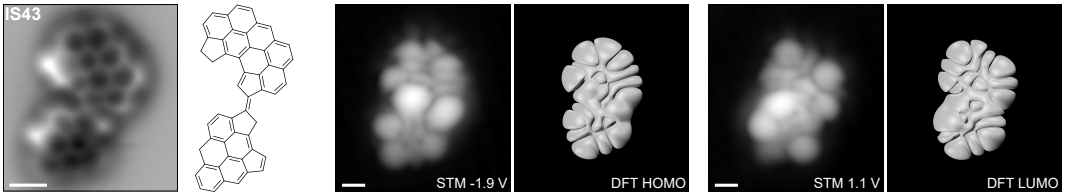


Figure A.4: **Orbital density images of IS43.** AFM image and proposed structure of IS43 together with constant-current STM images at PIR ($-1.9$ V) and NIR (1.1 V) showing the spatial distribution of HOMO and LUMO density, respectively. DFT calculations of the orbital densities of the proposed structure support the structure assignment. All scale bars are 5 Å.

Appendix B

# On-surface synthesis by atom manipulation

## B.1 STM characterization

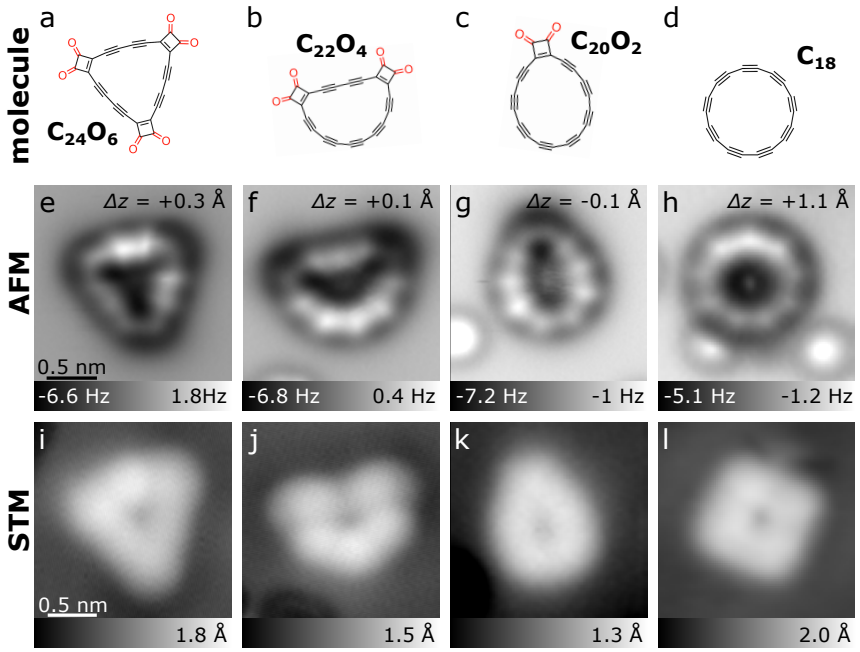


Figure B.1: **In-gap STM images.** The structures (first row) and AFM data (second row) are reproduced from Fig. 9.4 in chapter 9. The third row shows complementary STM data of the same molecules in that column, respectively. STM images were recorded in constant-current mode at $I = 0.5$ pA, $V = 0.2$ V (i, j, k) and $I = 0.7$ pA, $V = 0.1$ V (l). The same scale bar as in (e) and (i) applies to all AFM and all STM images, respectively. All measurements are obtained with CO-functionalized tips.

For the characterization of the electronic structure, STM images were recorded within the fundamental gap (denoted as in-gap), see Fig. B.1, and at the positive and negative ion resonances (PIR/NIR) for the precursor and the two most abundant intermediates, see Fig. B.2. For the $C_{24}O_6$ precursor, the in-gap STM image (Fig. B.1i) shows a bright feature in the center of the upper left side. This protrusion in the in-gap STM image was found in all imaged $C_{24}O_6$ molecules. It always corresponded to the bright side visible in the AFM images and therefore probably relates to the side of the molecule that has the largest

adsorption height. For cyclo[18]carbon, the in-gap STM shows fourfold symmetry with four protrusions, leading to a square-like shape (Fig. B.1l). The diagonals of the square were always aligned with non-polar directions of the NaCl(100) surface. We assign the fourfold contrast to the influence of the underlying fourfold symmetric NaCl surface.

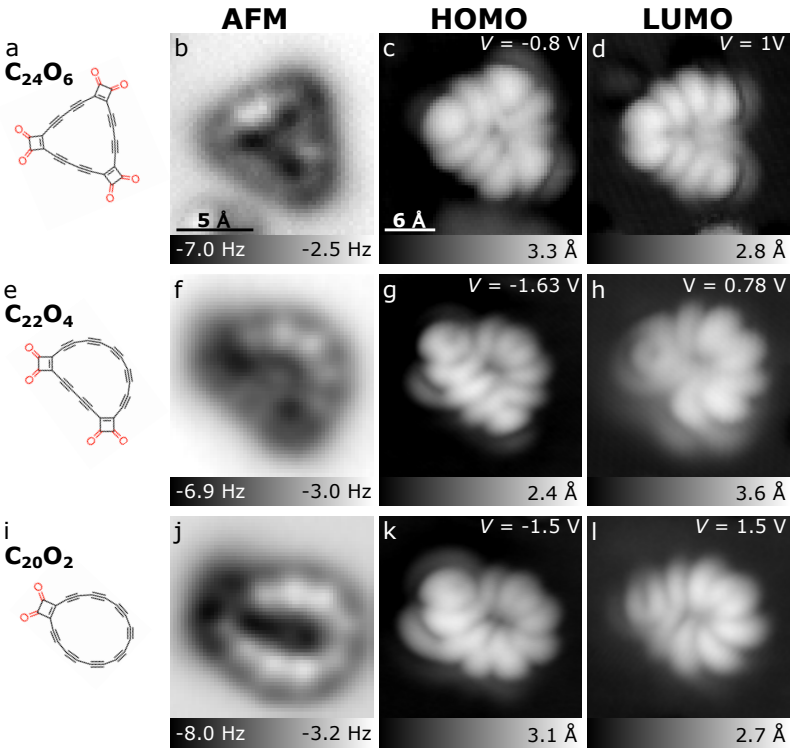


Figure B.2: **Orbital density maps.** Molecular structures (first column), AFM images (second column) and STM orbital density images (third and fourth column) of the cyclo[18]carbon precursors (a–d) $C_{24}O_6$ (STM at $I = 1$ pA), (e–h) $C_{22}O_4$ (STM at $I = 0.5$ pA) and (i–l) $C_{20}O_2$ (STM at $I = 0.5$ pA). The images acquired at the first resonance at negative bias voltage are interpreted as density of the HOMO, while the images acquired at the first resonance at positive bias voltage are interpreted as density of the LUMO.

The orbital density images of precursor and intermediates (Fig. B.2) show qualitatively different contrast and different nodal planes for PIR and NIR, indicating that these molecules are in a closed shell configuration and charge neutral when imaged within the gap. We can thus assign the STM image recorded at the PIR to the density of the HOMO and the NIR to the density of the LUMO. For cyclo[18]carbon, imaging of the ion resonances was not possible because of its charge bistability. Charge-state switching to the negative charge state was observed for positive bias, $V > 0.6$ V. At negative bias we did not observe a resonance for cyclo[18]carbon up to sample voltages of $V < -1.5$ V and the molecule was not stable (jumped on the surface) for increased negative voltages. Figure B.3 shows a cyclo[18]carbon adsorbed directly next to a $C_{24}O_6$ precursor molecule. Both molecules are not covalently linked, as is apparent from the AFM images at different tip-sample distances (Fig. B.3, a to c). At $V = -0.8$ V ($V = +1.3$ V), the onset of the PIR (NIR) of $C_{24}O_6$ is reached, leading to an increase in tunnel current at this voltage at the positions of large densities of

the HOMO (LUMO) above the $C_{24}O_6$ molecule in constant-height STM images (Fig. B.3, e to f). No contrast (no tunnel current) is measured above cyclo[18]carbon in these images.

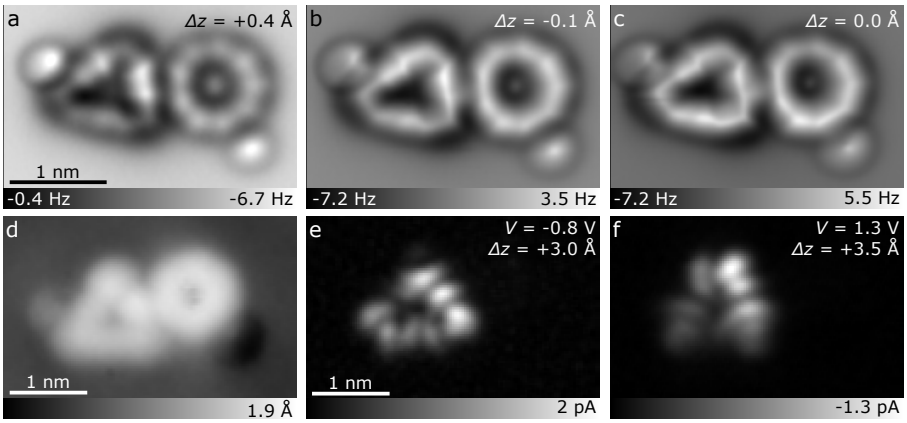


Figure B.3: **Comparative measurements of $C_{24}O_6$ and cyclo[18]carbon.** (a–c) AFM and (d–f) STM images of a $C_{24}O_6$ precursor and a cyclo[18]carbon molecule adsorbed adjacent to each other. The bright features in the AFM images next to the molecule stem from adjacently adsorbed CO molecules. (d) In-gap constant-current STM image at $V = 0.13$ V and $I = 0.5$ pA. (e, f) Constant-height STM images obtained at the onset of the PIR and NIR of the $C_{24}O_6$ precursor, respectively. In the images recorded in constant-height mode (a–c, e, f), $\Delta z$ corresponds to the tip-height offset with respect to an STM setpoint of $V = 0.2$ V and $I = 0.5$ pA.

## B.2 Reaction statistics

### Cyclocarbon oxide precursor

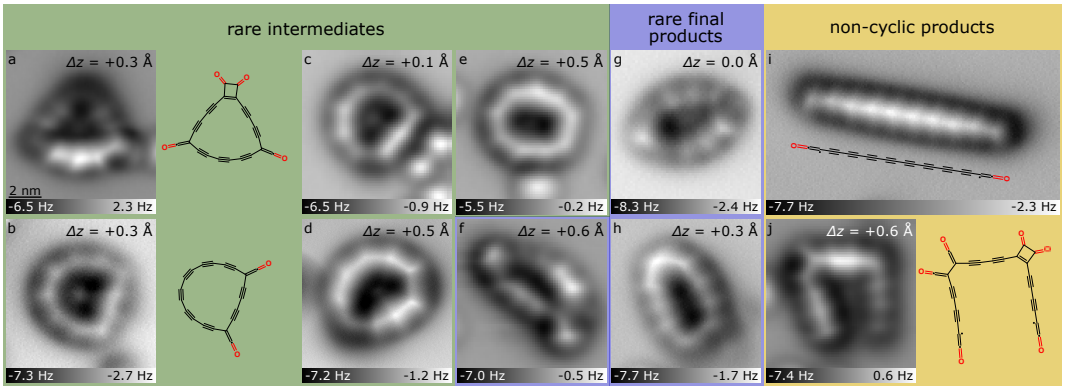


Figure B.4: **Molecules less commonly formed by atom manipulation.** AFM images and suggested chemical structures (for molecules a, b, i, j) of examples of molecules that have been formed by atom manipulation. (a–e) Less common intermediates, summarized as 'rare intermediates' in the reaction statistics (Table B.1). For the molecules shown in (a) and (b), the assigned chemical structures are displayed next to the AFM images. In these, the removal of 2 CO and 4 CO from $C_{24}O_6$, generated different $C_{22}O_4$ and $C_{20}O_2$ isomers compared to the ones described in the main text. (f–h) AFM images of cyclic molecules that did not react further upon voltage pulses. In the reaction statistics, molecules of this kind are summarized as 'rare final products'. (i, j) Products in which a bond within the cyclic unit was broken with the assigned structure to the molecule. (i) shows an AFM image of a linear polyyne chain with the assigned structure shown in the inset. In the reaction statistics, molecules of this kind are summarized as 'non-cyclic products'. $\Delta z$ is given with respect to the STM setpoint of $V = 0.2$ V and $I = 0.5$ pA in a, c, e and i; $V = 0.2$ V and $I = 0.8$ pA in b and h; $V = 0.2$ V and $I = 1$ pA in d; $V = 0.1$ V and $I = 0.7$ pA in f; $V = 0.3$ V and $I = 0.5$ pA in g; $V = 0.1$ V and $I = 0.5$ pA in j.

Figure B.4 shows products that were less frequently formed by atom manipulation. Less common intermediates in which the AFM image suggests that in two masking groups a single CO unit was removed to generate two monoketenes and subsequent rearrangement of the polyynic region to reveal an additional triple bond are summarized as 'rare intermediates' (Fig. B.4a–e). Rare cyclic reaction products that could not be further manipulated are indicated as 'rare final products' (Fig. B.4f–h). Reactions in which the cyclic unit was broken are indicated as 'non-cyclic products' (Fig. B.4i, j). Table B.1 summarizes the yield of all tip-induced decarbonylation attempts starting with either the intact precursor ($C_{24}O_6$) or an intermediate. The most abundant intermediates ($C_{22}O_4$ and $C_{20}O_2$) are listed separately. The yields for cyclo[18]carbon formation *via* the different experimentally observed paths is listed in Table B.2.

Table B.1: **Reaction statistics for on-surface reactions from $C_{24}O_6$.** Educts were the intact precursor $C_{24}O_6$, the two most abundant intermediates, $C_{22}O_4$ and $C_{20}O_2$ and other seldomly observed intermediates (rare intermediates). Reaction products were $C_{22}O_4$ and $C_{20}O_2$, rare intermediates, cyclo[18]carbon ($C_{18}$), chain-like structures due to breaking of a bond within the cyclic system (non-cyclic products) and other rare cyclic reaction products that could not be further manipulated (rare final products; see Fig. B.4). For the table in total N = 90 single molecule reactions induced by atom manipulation were evaluated.

| Educt \ Product | $C_{22}O_4$ | $C_{20}O_2$ | rare intermediates | $C_{18}$ | non-cyclic products | rare final products |
|---|---|---|---|---|---|---|
| $C_{24}O_6$ | 17% | 28% | 4% | 4% | 26% | 21% |
| $C_{22}O_4$ | / | 31% | 6% | 13% | 31% | 19% |
| $C_{20}O_2$ | / | / | 19% | 13% | 38% | 31% |
| rare intermediates | / | 20% | / | 20% | 20% | 40% |

Table B.2: Yield for the formation of cyclo[18]carbon *via* different observed reaction paths.

| reaction path | | | | | | | yield |
|---|---|---|---|---|---|---|---|
| $C_{24}O_6$ | → | $C_{18}$ | | | | | 4% |
| $C_{24}O_6$ | → | $C_{20}O_2$ | → | $C_{18}$ | | | 3.6% |
| $C_{24}O_6$ | → | $C_{22}O_4$ | → | $C_{18}$ | | | 2.2% |
| $C_{24}O_6$ | → | rare intermediate | → | $C_{18}$ | | | 0.8% |
| $C_{24}O_6$ | → | $C_{22}O_4$ | → | $C_{18}$ | | | 0.7% |
| $C_{24}O_6$ | → | $C_{20}O_2$ | → | rare intermediate | → | $C_{18}$ | 1.1% |
| $C_{24}O_6$ | → | $C_{22}O_4$ | → | rare intermediate | → | $C_{18}$ | 0.2% |
| $C_{24}O_6$ | → | rare intermediate | → | $C_{20}O_2$ | → | $C_{18}$ | 0.1% |

Total yield for cyclo[18]carbon formation: 12.7%

## Bromocyclocarbon precursor

Figure B.5 shows a series of AFM images of two bromocyclocarbon precursors prior to and after their tip-induced debromination reactions. This example illustrates the efficiency and reproducibility of cyclo[18]carbon formation by atom manipulation from bromocyclocarbon precursor molecules. The yields for cyclo[18]carbon formation from the bromocyclocarbon precursor $C_{18}Br_6$ are listed in Table B.3. Figure B.6 shows AFM data of cyclo[18]carbon (Fig. B.6a–c), unidentified intermediates (Fig. B.6d, e) and a rare final product formed by tip-induced atom manipulation from bromocyclocarbon precursors. After dissociation, the Br typically stayed close to the products.

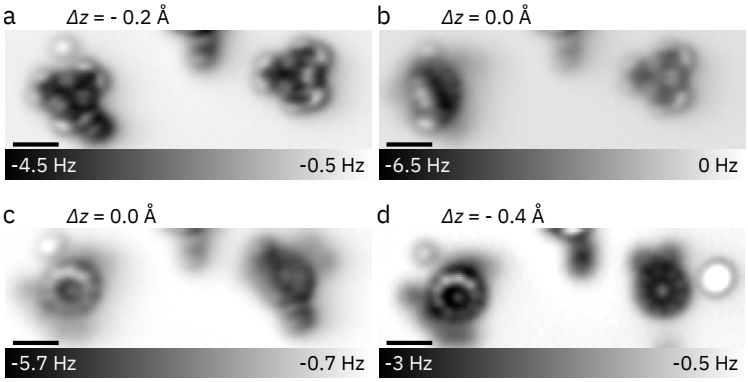


Figure B.5: **AFM images of two $C_{18}Br_6$ precursors prior to and after atom-manipulation.** (a) AFM image of two bromocyclocarbon precursors prior to atom manipulation. Bias voltage pulses of 2–3 V were applied with the tip in close proximity to the molecules. In (b), the precursor on the left has reacted to an intermediate while the precursor on the right remained intact. In (c) the precursor on the left has reacted to $C_{18}$ and the precursor on the right has reacted to an intermediate. (d) Shows two cyclo[18]carbon molecules generated by atom manipulation from the precursors shown in (a). The dark features next to the molecules can be assigned to dissociated Br atoms. They hinder motion of the molecules such that the intermediates and cyclo[18]carbon molecules are held in place during voltage pulsing. $\Delta z$ denotes the tip-height offset from an STM setpoint of $I = 0.5$ pA, $V = 0.2$ V. All scale bars correspond to 5 Å.

Table B.3: **Reaction statistics for on-surface reactions from $C_{18}Br_6$.** Educts were the intact precursor $C_{18}Br_6$ and partially debrominated intermediates. Reaction products were cyclo[18]carbon ($C_{18}$), partially debrominated intermediates, chain-like structures due to breaking of a bond within the cyclic system (non-cyclic products) and other rare cyclic reaction products that could not be further manipulated (rare final products). For the table in total 21 single molecule reactions induced by atom manipulation were evaluated out of which 14 started with the intact precursor and 7 started with an intermediate.

| Product / Educt | $C_{18}$ | unidentified intermediates | non-cyclic products | rare final products |
|---|---|---|---|---|
| $C_{18}Br_6$ | 21.4% | 42.9% | 7.1% | 28.3% |
| unidentified intermediates | 100% | / | / | / |

Total yield for cyclo[18]carbon formation: 64.3%

## B.3 Density functional theory calculations

DFT calculations were carried out using the all-electron code FHI-aims.[125] As an approximation to the exchange-correlation (x-c) functional the Heyd-Scuseria-Ernzerhof (HSE) hybrid functional[126] was used. The mixing parameter that controls the amount of exact exchange in HSE was set to 0.8. The Tkatchenko-Scheffler correction[221] was used to account for van der Waals interactions. For the calculations the default 'tight' settings for the atomic basis

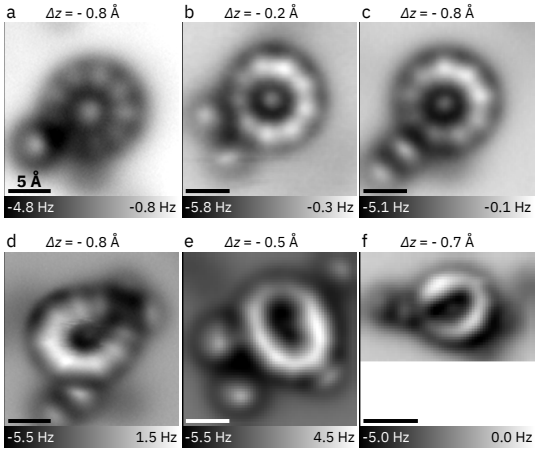


Figure B.6: **Additional AFM data of cyclo[18]carbon and other products synthesized from $C_{18}Br_6$.** (a)–(c) AFM images of different $C_{18}$ molecules. The bright features next to the molecules can be assigned to dissociated Br atoms. (d), (e) Intermediates with at least one Br masking group already dissociated. (f) Shows a rare final procut. $\Delta z$ denotes the tip-height offset from an STM setpoint of $I = 0.5$ pA, $V = 0.2$ V. All scale bars correspond to 5 Å.

sets were employed. All molecules were calculated in the gas phase, and the structures were relaxed until the forces acting on atoms were smaller than $10^{-3}$ eV $\cdot$ Å$^{-1}$.
For the intermediates ($C_{22}O_4$, $C_{20}O_2$), the HSE functional yielded similar bond-length alternation (BLA) for the different length polyynic segments in the different molecules ($C_{24}O_6$, $C_{22}O_4$, $C_{20}O_2$, $C_{18}$).
For the different resonance structures of cyclo[18]carbon shown in Fig. 9.1 and Figs. B.9–B.12, the geometries calculated by Arulmozhiraja and Ohno[171] from coupled-cluster singles and doubles (CCSD) calculations with the correlation-consistent polarized valence double-zeta (cc-pVDZ) basis set[171] as well as structures with twice and four times the BAA and half and twice the BLA were used. The respective electronic structures were calculated using DFT with the HSE x-c functional and the settings described above by letting the charge density relax while keeping the atom positions constrained.

## B.4 Additional AFM data and AFM simulations

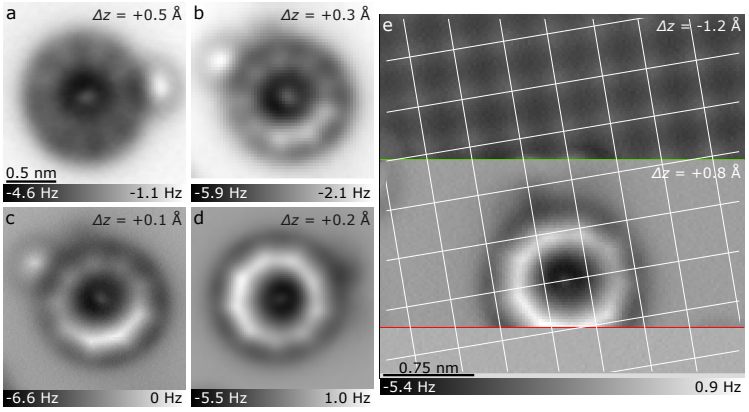


Figure B.7: **Additional AFM data of cyclo[18]carbon.** (a–d) Constant-height AFM images of different cyclo[18]carbon molecules recorded at different tip-sample distances, decreasing from (a) to (d). (b) and (c) show the same molecule. (e) AFM image of cyclo[18]carbon to determine the adsorption position. The slow scan direction was from top to bottom. In the upper part of the image, a small tip height ($\Delta z = -1.2$ Å) was used to resolve the NaCl surface atomically. The Cl anions appear as bright features and are indicated by the overlaid grid. At the green line, the tip height was increased to $\Delta z = 0.8$ Å. At the red line, the tip lost the CO molecule. The measurement shows cyclo[18]carbon adsorbed on a Cl-Cl bridge site. In (a, d, e), $\Delta z$ is given with respect to an STM setpoint of $V = 0.1$ V and $I = 0.5$ pA, in (b, c), $\Delta z$ is given with respect to an STM setpoint of $V = 0.2$ V and $I = 0.5$ pA.

Figure B.7e shows a constant-height AFM image in which the tip height was changed to determine the adsorption position of cyclo[18]carbon. In the top part of the image, a small tip- height offset of $\Delta z = -1.2$ Å (setpoint $V = 0.1$ V and $I = 0.5$ pA) was chosen to atomically resolve the NaCl lattice. The bright features in this part of the image correspond to Cl-atoms.[222] In the part of the image below the green line the tip-height offset was increased to $\Delta z = +0.8$ Å. Extrapolating the Cl lattice sites, we find that this cyclo[18]carbon is adsorbed with the center near a Cl-Cl bridge site. At the red line the CO-functionalized tip lost the CO.

AFM images acquired with CO-functionalized tips were simulated using the PPM code.[62,63] We simulated AFM images for the precursor $C_{24}O_6$, the partially decarbonylated intermediates ($C_{22}O_4$, $C_{20}O_2$) as well as the final product cyclo[18]carbon using the PPM code implemented by Hapala *et al.*.[62] This code also allows electrostatic interactions to be included by assigning a charge to the CO molecule and letting it interact with the Hartree potential of the sample. As input for the AFM simulation, we used the atomic coordinates from the DFT gas-phase structure optimization as well as the corresponding DFT Hartree potential. For all AFM simulations, we used a lateral spring constant for the CO at the tip of 0.2 $^{\mathrm{N}}/_{\mathrm{m}}$ and an electrostatic monopole on the oxygen of $-0.05$ e[223] and the experimental oscillation amplitude $A = 50$ pm.
Figure B.8 shows simulated AFM images for the intact precursor as well as the two most abundant intermediates at different tip-sample distances. All images have been calculated

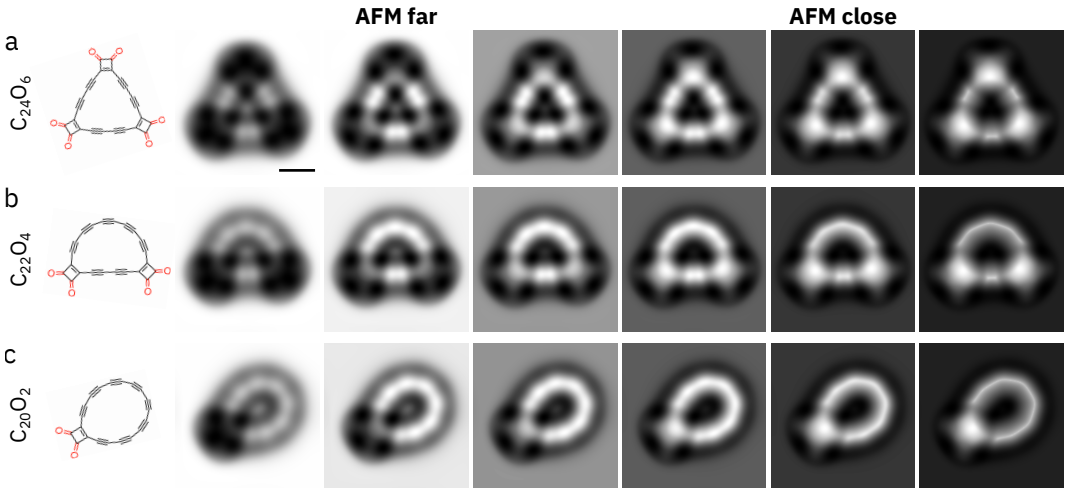


Figure B.8: **AFM simulations of the precursor and intermediates.** Chemical structure and simulated AFM images at decreasing tip-sample distances (from left to right) for the pristine precursor $C_{24}O_6$ (a) and the intermediates $C_{22}O_4$ (b) and $C_{20}O_2$ (c). The molecular structure was optimized by DFT using the HSE x-c functional. The scale bar is 5 Å and all images have the same scale.

using the results obtained from the HSE x-c functional as input. The HSE-based simulated images for the pristine precursor $C_{24}O_6$ (Fig. B.8a and Fig. 9.4d and e) show very good agreement with the experimental images, with two bright lobes on each of the three sides of the triangular carbon backbone. Each of the bright lobes can be ascribed to one of the triple bonds. For the two intermediates $C_{22}O_4$ and $C_{20}O_2$ (Fig. B.8b and c, respectively) the agreement with experimental data is very good as well. At large and medium tip-sample distances, the AFM simulations show five bright lobes at the longer bend part of the molecule for $C_{22}O_4$ and eight lobes for $C_{20}O_2$, which again correspond to the triple bonds. Since for the AFM simulations the optimized gas-phase geometry was used as an input, the simulation does not account for non-planar adsorption geometries. Therefore, all sides of the molecule exhibit equal contrast. Additionally, the CO moieties appear brighter compared to the experimental AFM images since they are not bent down towards the surface in the geometry that was used for simulating the AFM images.
Figures B.9 to B.12 show simulated AFM images for four different resonance structures of cyclo[18]carbon, *i.e.*, $D_{18h}$ cumulene (Fig. B.9), $D_{9h}$ polyyne (Fig. B.10), $D_{9h}$ cumulene (Fig. B.11) and $C_{9h}$ polyyne (Fig. B.12) with different degrees of BLA and BAA. As an input we used the Hartree potentials for the relaxed charge densities of the different geometries from the HSE x-c functional, as described above.
The AFM simulations confirm our interpretation of the experimental data that cyclo[18]carbon adopts a polyynic structure on NaCl. However, whether the ground state geometry exhibits $D_{9h}$ or $C_{9h}$ symmetry cannot be resolved since small bond angle alternations are not visible.

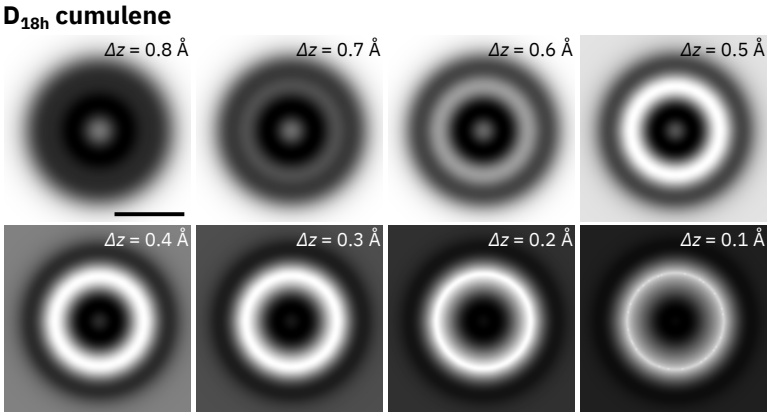


Figure B.9: $D_{18h}$ **cumulene.** Calculated AFM images of $C_{18}$ with a $D_{18h}$ cumulene geometry at decreasing tip-sample distances from top left to bottom right (geometry **A**: $d_1 = d_2 = 1.297$ Å, $\theta_1 = \theta_2 = 160°$). The images in the respective bottom right panels show again the AFM simulation for $\Delta z = 0.1$ Å, but overlaid with the corresponding molecular structure model.

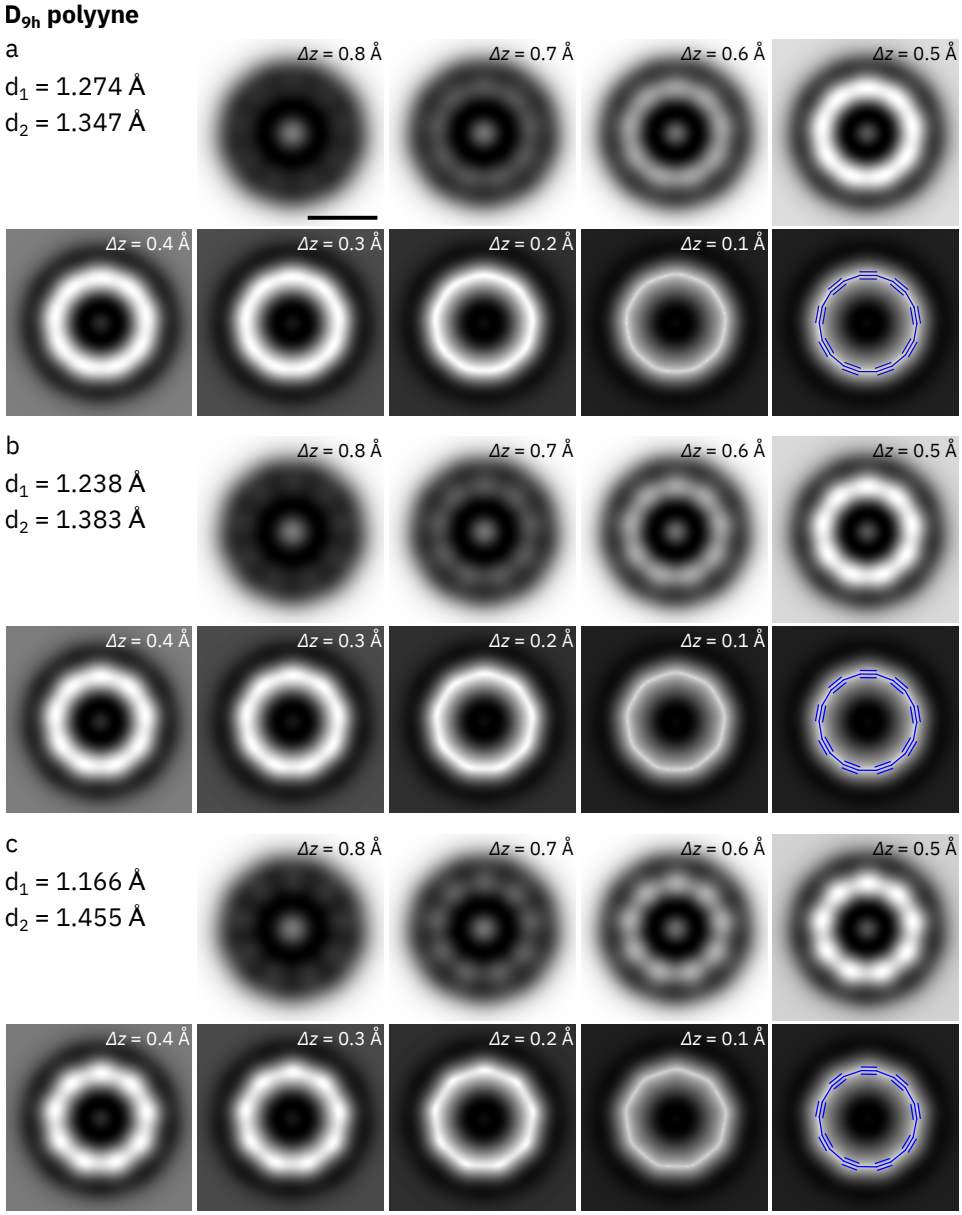


Figure B.10: $D_{9h}$ **polyyne.** Calculated AFM images of $C_{18}$ with a $D_{9h}$ polyyne geometry with different degrees of BLA at decreasing tip-sample distances from top left to bottom right. The BLA corresponds to half the theoretically predicted value (a, $BLA = 0.073$ Å), the predicted geometry of ref. [171] (b, $BLA = 0.145$ Å) and twice the predicted value (c, $BLA = 0.289$ Å). The images in the respective bottom right panels show again the AFM simulation for $\Delta z = 0.1$ Å, but overlaid with the corresponding molecular structure model.

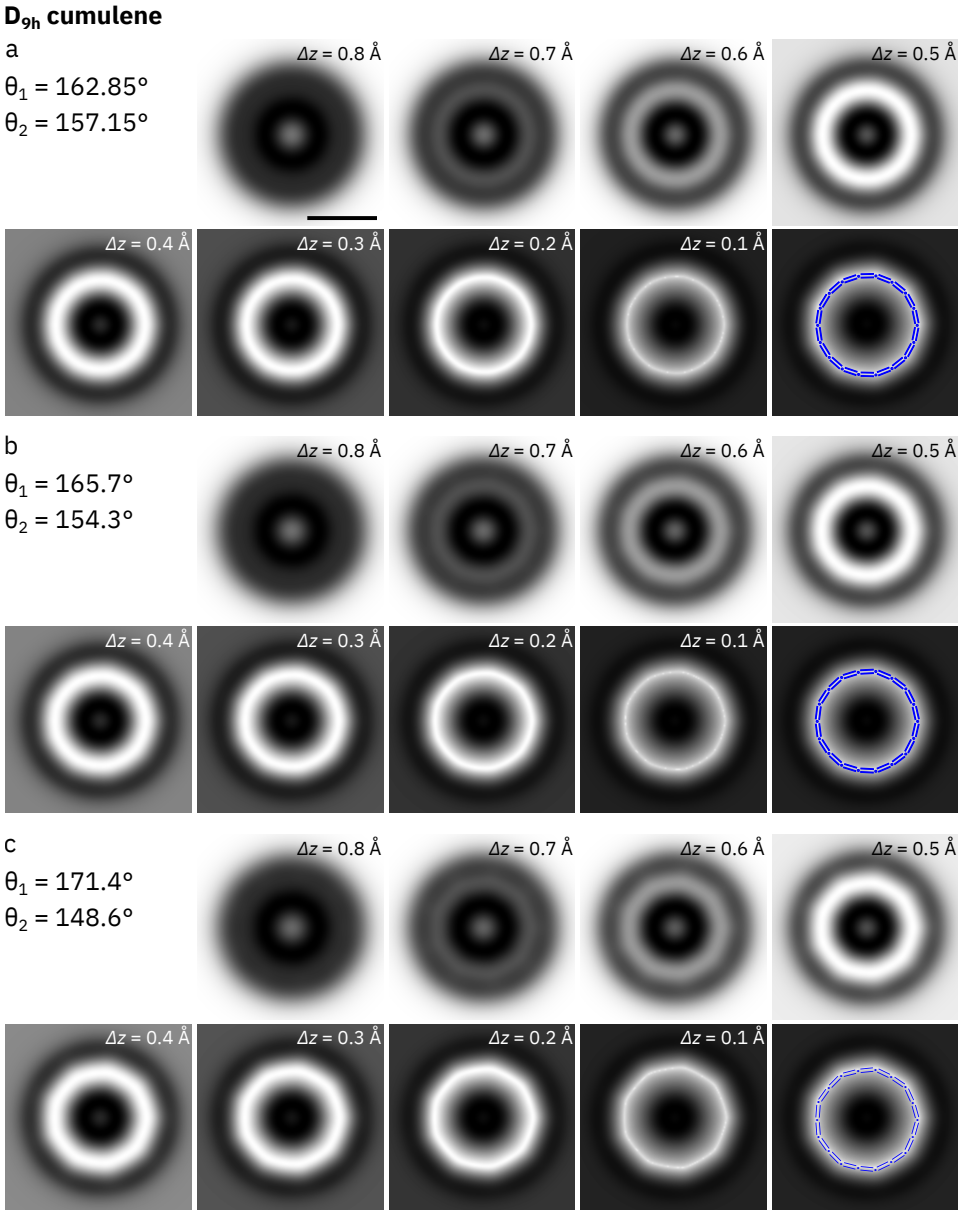


Figure B.11: $D_{9h}$ **cumulene.** Calculated AFM images of $C_{18}$ with a $D_{9h}$ cumulene geometry with different degrees of BAA at decreasing tip-sample distances from top left to bottom right. The BAA corresponds to the calculated geometry of ref. [171] (a, $BAA = 5.7°$), as well as twice (b, $BAA = 11.4°$) and four times the predicted value (c, $BAA = 22.4°$). The images in the respective bottom right panels show again the AFM simulation for $\Delta z = 0.1$ Å, but overlaid with the corresponding molecular structure model.

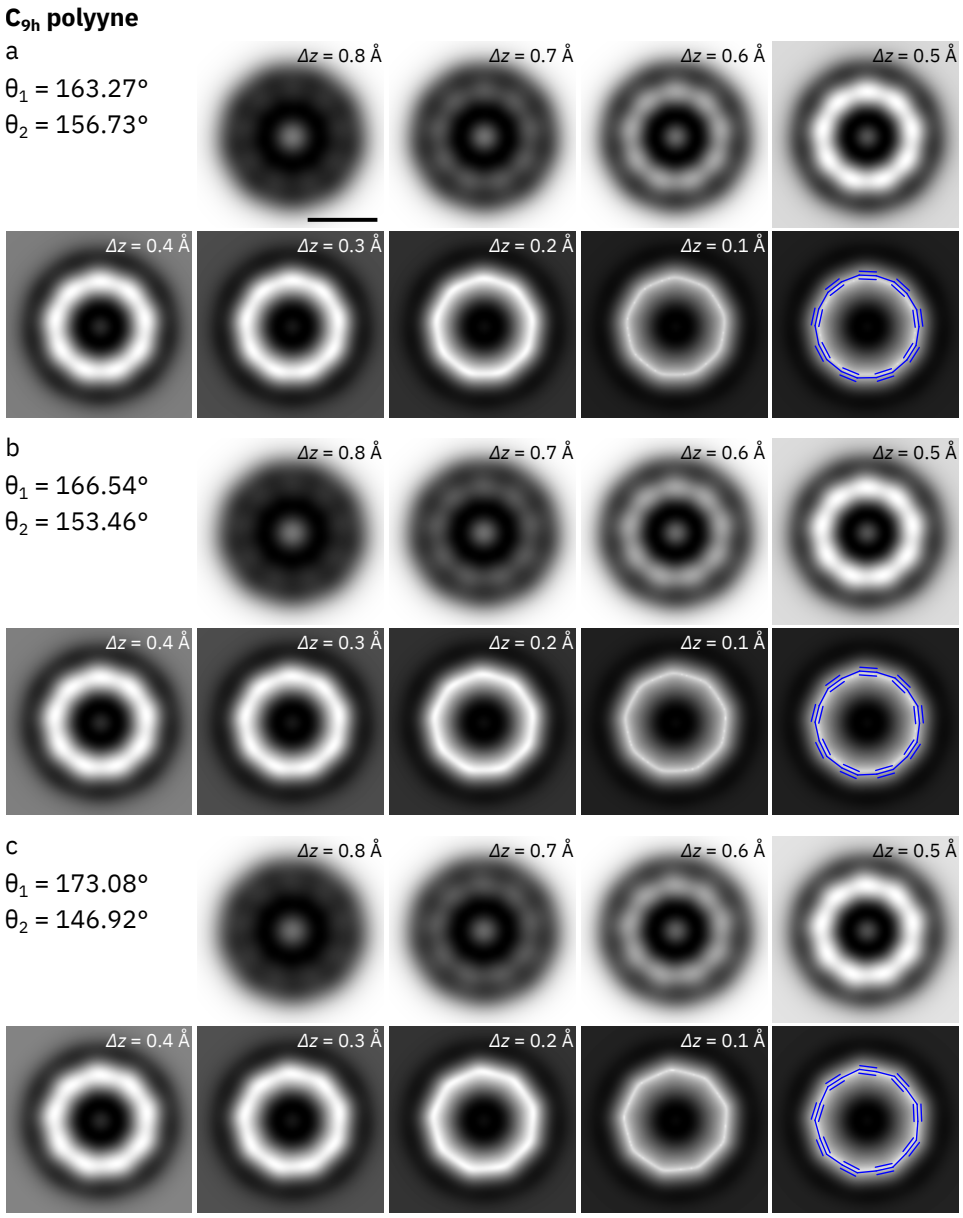


Figure B.12: $C_{9h}$ **polyyne.** Calculated AFM images of $C_{18}$ with a $C_{9h}$ polyyne geometry with $BLA = 0.145$ Å, corresponding to the calculated geometry of ref. [171], and different degrees of BAA at decreasing tip-sample distances from top left to bottom right. The BAA corresponds to the calculated geometry of ref. [171] (a, $BAA = 6.54°$), as well as twice (b, $BAA = 13.08°$) and four times the predicted value (c, $BAA = 26.16°$). The images in the respective bottom right panels show again the AFM simulation for $\Delta z = 0.1$ Å, but overlaid with the corresponding molecular structure model.

## B.5 On-surface covalent coupling of molecules by atom manipulation

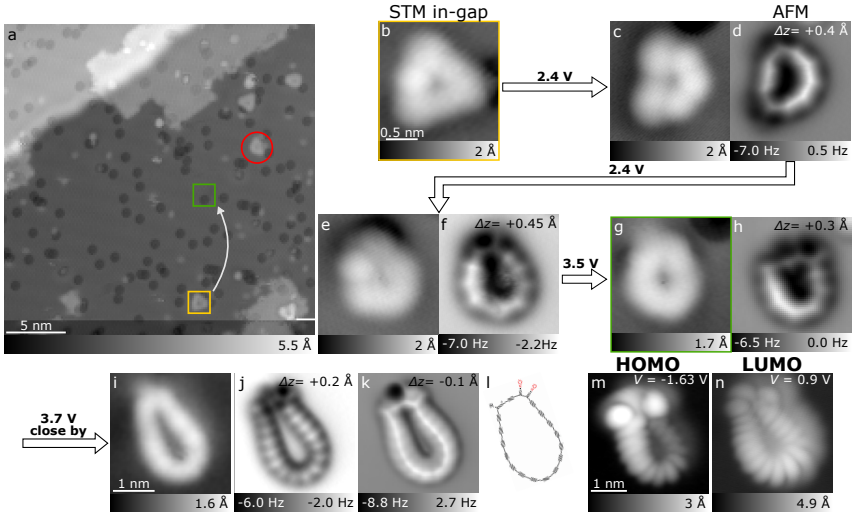


Figure B.13: **Pathway for the reaction of two adjacent molecules.** (a) STM overview ($V = 0.6$ V and $I = 0.5$ pA). The yellow box marks the $C_{24}O_6$ precursor shown in (b) that was chemically altered by applying voltage pulses/scanning at elevated bias voltages. Upon applying elevated bias voltages the molecule was partially decarbonylated, as indicated by the consecutive STM and AFM images (c–h). The voltages used to chemically alter the molecule are indicated above the arrows. During decarbonylation, the molecule jumped several times and eventually landed in the area marked by the green box in (a). In the last step, the molecule jumped and most likely reacted with the molecule marked by the red circle in (a), yielding the molecule shown in (i–k). (l) Suggested structure and (m, n) STM orbital density maps recorded at the PIR and NIR (at $I = 1$ pA), respectively, of the molecule shown in (i–k). The scale bars in (b, i, m) apply to all following images, respectively. (b–f) and (i–k) were recorded using a setpoint of $V = 0.2$ V and $I = 0.5$ pA, for (g–h) $V = 0.2$ V, $I = 1$ pA was used.

Figure B.13 depicts the formation of a large ring with at least one unknown side group by atom manipulation. Figure B.13a shows an STM overview image before the ring was formed. The employed $C_{24}O_6$ precursor (Fig. B.13b) is highlighted by a yellow box. Voltage pulses of $V = 2.4$ V and $V = 3.5$ V, respectively, were applied atop the molecule, resulting in partial decarbonylation (Fig. B.13c to f). Eventually, the molecule shown in Fig. B.13g and h was found in the area marked by the green box in Fig. B.13a. Upon scanning with an elevated bias voltage ($V = 3.7$ V, $I = 1$ pA), the molecule jumped away. The fused molecule shown in Fig. B.13i to n was found close to the molecule marked by the red circle in Fig. B.13a. Figure B.13i to k show STM images and AFM images at two different tip-sample distances, from which the suggested structure shown in Fig. B.13l is inferred. HOMO and LUMO densities of the fused cyclic molecule are shown in fig. B.13m and n. In addition to molecules fused by atom manipulation, we also found fused molecules on the surface that had likely reacted during the sublimation and adsorption process. Figure B.14 shows a molecule that was found on the surface, where no voltage pulses had been applied in the

vicinity before. The AFM contrast suggests that this molecule was formed by coalescence of three partially decarbonylated precursor molecules. STM orbital density images (Fig. B.14c and d) reveal that the $\pi$-system is delocalized over the entire molecule.

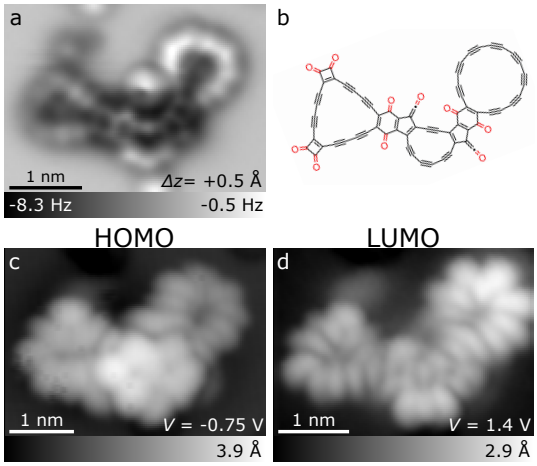


Figure B.14: **Three fused molecules.** (a) AFM image of an already reacted molecule. $\Delta z$ is given with respect to the STM setpoint of $V = 0.2$ V and $I = 0.7$ pA. (b) Tentatively assigned structure of the molecule with a molecular formula of $C_{64}O_{10}$. The molecule could have resulted from the reaction $C_{24}O_6$ + $C_{20}O_2$ + $C_{20}O_2$. (c, d) STM orbital density images of the same molecule recorded at the PIR and NIR, respectively, at $I = 0.7$ pA. Delocalization of the orbital densities over the entire molecule indicate a delocalized $\pi$-system.

Appendix C

# Scanning tunneling microscopy indued luminescence

## C.1 Plasmonic emission in STML

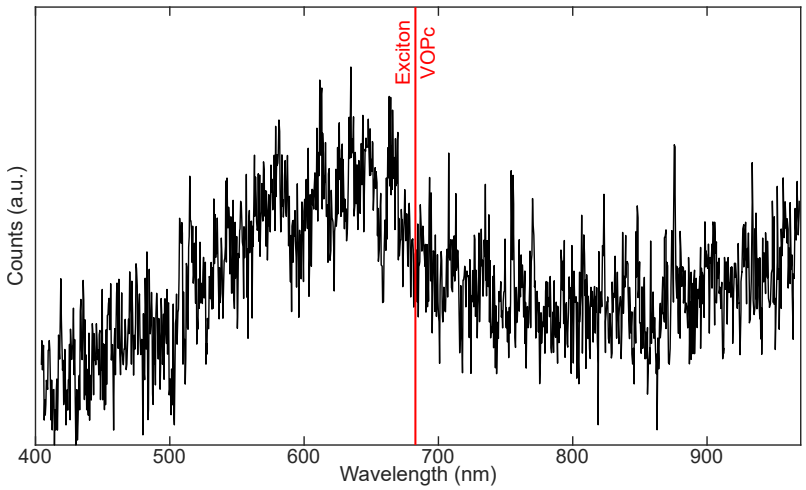


Figure C.1: **Plasmonic emission on bilayer NaCl.** STML spectrum recorded on bare bilayer NaCl, showing the purely plasmonic emission for this particular tip. The spectrum was recorded at a setpoint of $I = 150$ pA and $V = -2.5$ V and an integration time per frame of 4 min summed over 2 frames. The data is Savitzky-Golay- and Hampel-filtered. The supposed increase in intensity for larger wavelengths is an artifact stemming from the background correction.

In advance to STML measurements on the different molecular species, the purely plasmonic emission on the bare NaCl bilayer was recorded. This, on the one hand, allows an assessment of the quality of the tip in terms of its capability to excite NCP modes. On the other hand, since the coupling between molecular exciton and NCP plays a crucial role in the efficiency of the radiative decay of the exciton, and possibly already in the exciton formation,[79–81] knowledge of the plasmon spectrum is essential for the interpretation of the occurrence and/or relative intensities of radiative transitions within the molecules. An exemplary STML spectrum recorded on the bare bilayer NaCl is shown in Figure C.1 for a setpoint of $I = 150$ pA and $V = -2.5$ V. It shows the purely plasmonic emission for the same tip as in Figure 10.5b in the main manuscript, with maximum intensity around 630 nm.

## Appendix D

# Abbreviations

| | |
|---|---|
| AFM | atomic force microscope/microscopy |
| AM-AFM | amplitude modulation atomic force microscope/microscopy |
| AGC | automated gain control |
| BAA | bond angle alternation |
| BLA | bond length alternation |
| CCD | charge-coupled device |
| DFT | density functional theory |
| DHDMBA | 1,2-dihydro-3,5-dimethylbenz(J)aceanthrylene |
| DMBA | 3,5-dimethylbenz(J)aceanthrylene |
| EA | electron affinity |
| FIB | focused ion beam |
| FM-AFM | frequency modulation atomic force microscope/microscopy |
| HOMO | highest occupied molecular orbital |
| HSE | Heyd-Scuseria-Ernzerhof |
| IP | ionization potential |
| IS | incipient soot |
| ISL | interface state localization |
| LDOS | local density of states |
| LJ | Lennard-Jones |
| LUMO | lowest unoccupied molecular orbital |
| LSPP | localized surface plasmon polariton |
| NCP | nanocavity plasmon |
| NIR | negative ion resonance |
| PAH | polycyclic aromatic hydrocarbon |
| PBE | Perdew-Burke-Ernzerhof |
| PIR | positive ion resonance |
| PLL | phase-locked loop |
| PPM | probe particle model |
| PS | primary soot |
| PTCDA | Perylenetetracarboxylic dianhydride |
| SPM | scanning probe microscope/microscopy |
| SPP | surface plasmon polariton |
| STM | scanning tunneling microscope/microscopy |
| STML | scanning tunneling microscopy induced luminescence |
| STS | scanning tunneling spectroscopy |
| UHV | ultra-high vacuum |
| vdW | van der Waals |
| VOPc | vanadyl-phthalocyanine |
| VPc | vanadium-phthalocyanine |
| x-c | exchange correlation |

| | |
|---|---|
| 2DEG | 2-dimensional electron gas |
| 4NCuPc | copper(II)-tetraazaphthalocyanine |

# Contributors to this work

The majority of the work presented in this thesis was only possible thanks to the collaboration with other scientists. First of all my co-workers and former co-workers at IBM Research (in alphabetical order): Florian Albrecht, Rolf Allenspach, Shadi Fatayer, Leo Gross, Gerhard Meyer, Nikolaj Moll and Fabian Schulz. They contributed to all parts of this thesis through discussions, valuable advice, proofreading and general support in the lab. Fabian Schulz participated in all measurements.

The following list summarizes other relevant contributors to the different projects of this thesis.

**Chapter 8:** Mario Commodo and Patrizia Minutolo from the Insituto di Ricerche sulla Combustione, CNR as well as Gianluigi De Falco and Andrea D'Anna from the Dipartimento di Ingegneria Chimica, dei Materiali e della Produzione Industriale from the University of Naples Federico II both from Naples, Italy work in the field of combustion research. They provided and pre-characterized the soot samples by differential mobility analysis and Raman spectrosopy. Most importantly, they introduced us to the field of combustion research, interpreted our results together with us and put them into a greater context and taught us a lot about the formation of soot in general. Fabian Schulz measured the model compound and performed the DFT calculations on one of the proposed structures.

**Chapter 9:** Lorel M. Scriven, Przemyslaw Gawel, Harry L. Anderson, Alistair J. Sterling, Steffen L. Woltering and Kirsten E. Christensen from the Department of Chemistry from the University of Oxford synthesized and pre-characterized the precursor molecules. Harry Anderson and Leo Gross came up with the idea to synthesize cyclocarbon by atom manipulation. Lorel Scriven performed the synthesis and, as part of her PhD thesis, developed the synthetic route to bromocyclocarbon. She was at the IBM Research lab for a total of two weeks, assisting in the measurements and discussing the reaction mechanisms for the unmasking of the precursors. Kirsten Christensen analyzed the crystal structure.

# Bibliography


[1] G. Binnig, H. Rohrer, C. Gerber, and E. Weibel. "Surface Studies by Scanning Tunneling Microscopy". *Phys. Rev. Lett.* **49**, 57–61 (1982). DOI: 10.1103/PhysRevLett.49.57.

[2] G. Binnig, C. F. Quate, and C. Gerber. "Atomic Force Microscope". *Phys. Rev. Lett.* **56**, 930–933 (1986). DOI: 10.1103/PhysRevLett.56.930.

[3] T. R. Albrecht, P. Grütter, D. Horne, and D. Rugar. "Frequency Modulation Detection Using High-Q Cantilevers for Enhanced Force Microscope Sensitivity". *J. Appl. Phys.* **69**, 668–673 (1991). DOI: 10.1063/1.347347.

[4] F. J. Giessibl. "High-speed force sensor for force microscopy and profilometry utilizing a quartz tuning fork". *Appl. Phys. Lett.* **73**, 3956–3958 (1998). DOI: 10.1063/1.122948.

[5] L. Gross, F. Mohn, N. Moll, P. Liljeroth, and G. Meyer. "The Chemical Structure of a Molecule Resolved by Atomic Force Microscopy". *Science* **325**, 1110–1114 (2009). DOI: 10.1126/science.1176210.

[6] L. Gross, F. Mohn, N. Moll, B. Schuler, A. Criado, E. Guitián, D. Peña, A. Gourdon, and G. Meyer. "Bond-Order Discrimination by Atomic Force Microscopy". *Science* **337**, 1326–1329 (2012). DOI: 10.1126/science.1225621.

[7] S. Fatayer, F. Albrecht, Y. Zhang, D. Urbonas, D. Peña, N. Moll, and L. Gross. "Molecular structure elucidation with charge-state control". *Science* **365**, 142–145 (2019). DOI: 10.1126/science.aax5895.

[8] J. Repp, G. Meyer, S. M. Stojkovič, A. Gourdon, and C. Joachim. "Molecules on Insulating Films: Scanning-Tunneling Microscopy Imaging of Individual Molecular Orbitals". *Phys. Rev. Lett.* **94**, 026803 (2005). DOI: 10.1103/PhysRevLett.94.026803.

[9] D. Eigler, C. Lutz, and W. Rudge. "An atomic switch realized with the scanning tunnelling microscope". *Nature* **352**, 600–603 (1991). DOI: 10.1038/352600a0.

[10] L. Bartels, G. Meyer, and K.-H. Rieder. "Basic Steps of Lateral Manipulation of Single Atoms and Diatomic Clusters with a Scanning Tunneling Microscope Tip". *Phys. Rev. Lett.* **79**, 697–700 (1997). DOI: 10.1103/PhysRevLett.79.697.

[11] T. A. Jung, R. R. Schlittler, J. K. Gimzewski, H. Tang, and C. Joachim. "Controlled Room-Temperature Positioning of Individual Molecules: Molecular Flexure and Motion". *Science* **271**, 181–184 (1996). DOI: 10.1126/science.271.5246.181.

[12] G. V. Nazin, X. H. Qiu, and W. Ho. "Visualization and Spectroscopy of a Metal-Molecule-Metal Bridge". *Science* **302**, 77–81 (2003). DOI: 10.1126/science.1088971.

[13] D. Eigler and E. Schweizer. "Positioning single atoms with a scanning tunnelling microscope". *Nature* **344**, 524–526 (1990). DOI: 10.1038/344524a0.

[14] L. Bartels, G. Meyer, and K.-H. Rieder. "Controlled Vertical Manipulation of Single CO Molecules with the Scanning Tunneling Microscope: A Route to Chemical Contrast". *Appl. Phys. Lett.* **71**, 213–215 (1997). DOI: 10.1063/1.119503.

[15] B. C. Stipe, M. A. Rezaei, W. Ho, S. Gao, M. Persson, and B. I. Lundqvist. "Single-Molecule Dissociation by Tunneling Electrons". *Phys. Rev. Lett.* **78**, 4410–4413 (1997). DOI: 10.1103/PhysRevLett.78.4410.

[16] S.-W. Hla, L. Bartels, G. Meyer, and K.-H. Rieder. "Inducing All Steps of a Chemical Reaction with the Scanning Tunneling Microscope Tip: Towards Single Molecule Engineering". *Phys. Rev. Lett.* **85**, 2777–2780 (2000). DOI: 10.1103/PhysRevLett.85.2777.

[17] P. Liljeroth, J. Repp, and G. Meyer. "Current-Induced Hydrogen Tautomerization and Conductance Switching of Naphthalocyanine Molecules". *Science* **317**, 1203–1206 (2007). DOI: 10.1126/science.1144366.

[18] L. Grill. "Functionalized molecules studied by STM: motion, switching and reactivity". *J. Phys. Condens. Matter* **20**, 053001 (2008). DOI: 10.1088/0953-8984/20/05/053001.

[19] J. Repp, G. Meyer, S. Paavilainen, F. E. Olsson, and M. Persson. "Imaging Bond Formation Between a Gold Atom and Pentacene on an Insulating Surface". *Science* **312**, 1196–1199 (2006). DOI: 10.1126/science.1126073.

[20] N. Pavliček, B. Schuler, S. Collazos, N. Moll, D. Pérez, E. Guitián, G. Meyer, D. Peña, and L. Gross. "On-Surface Generation and Imaging of Arynes by Atomic Force Microscopy". *Nat. Chem.* **7**, 623–628 (2015). DOI: 10.1038/nchem.2300.

[21] N. Pavliček, A. Mistry, Z. Majzik, N. Moll, G. Meyer, D. J. Fox, and L. Gross. "Synthesis and Characterization of Triangulene". *Nat. Nanotechnol.* **12**, 308 (2017). DOI: 10.1038/nnano.2016.305.

[22] S. Fatayer, N. Moll, S. Collazos, D. Pérez, E. Guitián, D. Peña, L. Gross, and G. Meyer. "Controlled Fragmentation of Single Molecules with Atomic Force Microscopy by Employing Doubly Charged States". *Phys. Rev. Lett.* **121**, 226101 (2018). DOI: 10.1103/PhysRevLett.121.226101.

[23] D. G. de Oteyza et al. "Direct Imaging of Covalent Bond Structure in Single-Molecule Chemical Reactions". *Science* **340**, 1434–1437 (2013). DOI: 10.1126/science.1238187.

[24] B. Schuler, S. Fatayer, F. Mohn, N. Moll, N. Pavliček, G. Meyer, D. Peña, and L. Gross. "Reversible Bergman cyclization by atomic manipulation". *Nature Chem.* **8**, 220–224 (2016). DOI: 10.1038/nchem.2438.

[25] N. Pavliček, P. Gawel, D. R. Kohn, Z. Majzik, Y. Xiong, G. Meyer, H. L. Anderson, and L. Gross. "Polyyne Formation via Skeletal Rearrangement Induced by Atomic Manipulation". *Nat. Chem.* **10**, 853–858 (2018). DOI: 10.1038/s41557-018-0067-y.

[26] R. Berndt, R. Gaisch, J. K. Gimzewski, B. Reihl, R. R. Schlittler, W. D. Schneider, and M. Tschudy. "Photon Emission at Molecular Resolution Induced by a Scanning Tunneling Microscope". *Science* **262**, 1425–1427 (1993). DOI: 10.1126/science.262.5138.1425.

[27] X. H. Qiu, G. V. Nazin, and W. Ho. "Vibrationally Resolved Fluorescence Excited with Submolecular Precision". *Science* **299**, 542–546 (2003). DOI: 10.1126/science.1078675.

[28] Y. Zhang et al. "Visualizing Coherent Intermolecular Dipole-Dipole Coupling in Real Space". *Nature* **531**, 623–627 (2016). DOI: 10.1038/nature17428.

[29] B. Doppagne, M. C. Chong, E. Lorchat, S. Berciaud, M. Romeo, H. Bulou, A. Boeglin, F. Scheurer, and G. Schull. "Vibronic Spectroscopy with Submolecular Resolution from STM-Induced Electroluminescence". *Phys. Rev. Lett.* **118**, 127401 (2017). DOI: 10.1103/PhysRevLett.118.127401.

[30] H. Haken and H. C. Wolf. *Atom- und Quantenphysik*. 7 edition, Springer, 2002.

[31] C. J. Chen. *Introduction to Scanning Tunneling Microscopy*. 2 edition, Oxford University Press, 2008.

[32] G. Binnig, H. Rohrer, C. Gerber, and E. Weibel. "Tunneling through a controllable vacuum gap". *Appl. Phys. Lett.* **40**, 178–180 (1982). DOI: 10.1063/1.92999.

[33] J. Bardeen. "Tunnelling from a Many-Particle Point of View". *Phys. Rev. Lett.* **6**, 57–59 (1961). DOI: 10.1103/PhysRevLett.6.57.

[34] J. Tersoff and D. R. Hamann. "Theory of the scanning tunneling microscope". *Phys. Rev. B* **31**, 805–813 (1985). DOI: 10.1103/PhysRevB.31.805.

[35] C. J. Chen. "Theory of scanning tunneling spectroscopy". *J. Vac. Sci. Technol.* **6**, 319–322 (1988). DOI: 10.1116/1.575444.

[36] C. J. Chen. "Tunneling matrix elements in three-dimensional space: The derivative rule and the sum rule". *Phys. Rev. B* **42**, 8841–8857 (1990). DOI: 10.1103/PhysRevB.42.8841.

[37] B. C. Stipe, M. A. Rezaei, and W. Ho. "Single-Molecule Vibrational Spectroscopy and Microscopy". *Science* **280**, 1732–1735 (1997). DOI: 10.1126/science.280.5370.1732.

[38] X. H. Qiu, G. V. Nazin, and W. Ho. "Vibronic States in Single Molecule Electron Transport". *Phys. Rev. Lett.* **92**, 206102 (2004). DOI: 10.1103/PhysRevLett.92.206102.

[39] S. W. Wu, G. V. Nazin, X. Chen, X. H. Qiu, and W. Ho. "Control of Relative Tunneling Rates in Single Molecule Bipolar Electron Transport". *Phys. Rev. Lett.* **93**, 236802 (2004). DOI: 10.1103/PhysRevLett.93.236802.

[40] J. Repp, G. Meyer, S. Paavilainen, F. E. Olsson, and M. Persson. "Scanning Tunneling Spectroscopy of Cl Vacancies in NaCl Films: Strong Electron-Phonon Coupling in Double-Barrier Tunneling Junctions". *Phys. Rev. Lett.* **95**, 225503 (2005). DOI: 10.1103/PhysRevLett.95.225503.

[41] S. Fatayer, B. Schuler, W. Steurer, I. Scivetti, J. Repp, L. Gross, M. Persson, and G. Meyer. "Reorganization Energy Upon Charging a Single Molecule on an Insulator Measured by Atomic Force Microscopy". *Nat. Nanotechnol.* **13**, 376–380 (2018). DOI: 10.1038/s41565-018-0087-1.

[42] , I. Swart, J. Niedenführ, G. Meyer, and J. Repp. "Symmetry Dependence of Vibration-Assisted Tunneling". *Phys. Rev. Lett.* **110**, 136101 (2013). DOI: 10.1103/PhysRevLett.110.136101.

[43] B. S. Brunschwig, S. Ehrenson, and N. Sutin. "Solvent reorganization in optical and thermal electron-transfer processes". *J. Phys. Chem.* **90**, 3657–3668 (1986). DOI: 10.1021/j100407a037.

[44] Valérie Vaissier, Piers Barnes, James Kirkpatrick, and Jenny Nelson. "Influence of polar medium on the reorganization energy of charge transfer between dyes in a dye sensitized film". *Phys. Chem. Chem. Phys.* **15**, 4804–4814 (2013). DOI: 10.1039/C3CP44562C.

[45] Rudolph A. Marcus. "Electron transfer reactions in chemistry. Theory and experiment". *Rev. Mod. Phys.* **65**, 599–610 (1993). DOI: 10.1103/RevModPhys.65.599.

[46] F. E. Olsson, S. Paavilainen, M. Persson, J. Repp, and G. Meyer. "Multiple Charge States of Ag Atoms on Ultrathin NaCl Films". *Phys. Rev. Lett.* **98**, 176803 (2007). DOI: 10.1103/PhysRevLett.98.176803.

[47] I. Swart, T. Sonnleitner, and J. Repp. "Charge State Control of Molecules Reveals Modification of the Tunneling Barrier with Intramolecular Contrast". *Nano Lett.* **11**, 1580–1584 (2011). DOI: 10.1021/nl104452x.

[48] J. Repp, G. Meyer, and K.-H. Rieder. "Snell's Law for Surface Electrons: Refraction of an Electron Gas Imaged in Real Space". *Phys. Rev. Lett.* **92**, 036803 (2004). DOI: 10.1103/PhysRevLett.92.036803.

[49] M. Crommie, C. Lutz, and D. Eigler. "Imaging standing waves in a two-dimensional electron gas". *Nature* **363**, 524–527 (1993). DOI: 10.1038/363524a0.

[50] Y. Hasegawa and Ph. Avouris. "Direct observation of standing wave formation at surface steps using scanning tunneling spectroscopy". *Phys. Rev. Lett.* **71**, 1071–1074 (1993). DOI: 10.1103/PhysRevLett.71.1071.

[51] J. Repp, G. Meyer, F. E. Olsson, and M. Persson. "Controlling the Charge State of Individual Gold Adatoms". *Science* **305**, 493–495 (2004). DOI: 10.1126/science.1099557.

[52] N. A. Burnham and R. J. Colton. "Measuring the nanomechanical properties and surface forces of materials using an atomic force microscope". *J. Vac. Sci. Technol. A* **7**, 2906–2913 (1989). DOI: 10.1116/1.576168.

[53] F. J. Giessibl. "Forces and frequency shifts in atomic-resolution dynamic-force microscopy". *Phys. Rev. B* **56**, 16010–16015 (1997). DOI: 10.1103/PhysRevB.56.16010.

[54] F. J. Giessibl. "Advances in atomic force microscopy". *Rev. Mod. Phys.* **75**, 949–983 (2003). DOI: 10.1103/RevModPhys.75.949.

[55] , I. Swart, J. Niedenführ, G. Meyer, and J. Repp. *Noncontact Atomic Force Microscopy*. 1 edition, vol. 3. Springer, 2015, 136101 pages. DOI: 10.1103/PhysRevLett.110.136101.

[56] N. Moll, L. Gross, F. Mohn, A. Curioni, and G. Meyer. "The mechanisms underlying the enhanced resolution of atomic force microscopy with functionalized tips". *New J. Phys.* **12**, 125020 (2010). DOI: 10.1088/1367-2630/12/12/125020.

[57] F. Mohn. "Probing electronic and structural properties of single molecules on the atomic scale". PhD thesis. Universität Regensburg, 2012, 136101 pages. DOI: 10.1103/PhysRevLett.110.136101.

[58] Y. Martin, C. C. Williams, and H. K. Wickramasinghe. "Atomic force microscope–force mapping and profiling on a sub 100-Å scale". *J. Appl. Phys.* **61**, 4723–4729 (1987). DOI: 10.1063/1.338807.

[59] H. C. Hamaker. "The London–van der Waals attraction between spherical particles". *Physica* **4**, 1058–1072 (1937). DOI: 10.1103/PhysRevLett.110.136101.

[60] L. Gross. "Recent Advances in Submolecular Resolution with Scanning Probe Microscopy". *Nat. Chem.* **3**, 273–278 (2011). DOI: 10.1038/nchem.1008.

[61] P. Hapala, R. Temirov, F. S. Tautz, and P. Jelínek. "Origin of High-Resolution IETS-STM Images of Organic Molecules with Functionalized Tips". *Phys. Rev. Lett.* **113**, 226101 (2014). DOI: 10.1103/PhysRevLett.113.226101.

[62] P. Hapala, G. Kichin, C. Wagner, F. S. Tautz, R. Temirov, and P. Jelínek. "Mechanism of high-resolution STM/AFM imaging with functionalized tips". *Phys. Rev. B* **90**, 085421 (2014). DOI: 10.1103/PhysRevB.90.085421.

[63] S. K. Hämäläinen, N. van der Heijden, J. van der Lit, S. den Hartog, P. Liljeroth, and I. Swart. "Intermolecular contrast in atomic force microscopy images without intermolecular bonds". *Phys. Rev. Lett.* **113**, 186102 (2014). DOI: 10.1103/PhysRevLett.113.186102.

[64] F. Mohn, B. Schuler, L. Gross, and G. Meyer. "Different Tips for High-Resolution Atomic Force Microscopy and Scanning Tunneling Microscopy of Single Molecules". *Appl. Phys. Lett.* **102**, 073109 (2013). DOI: 10.1063/1.4793200.

[65] B. Schuler, W. Liu, A. Tkatchenko, N. Moll, G. Meyer, A. Mistry, D. Fox, and L. Gross. "Adsorption Geometry Determination of Single Molecules by Atomic Force Microscopy". *Phys. Rev. Lett.* **111**, 106103 (2013). DOI: 10.1103/PhysRevLett.111.106103.

[66] L. Gross, B. Schuler, F. Mohn, N. Moll, W. Steurer, I. Scivetti, K. Kotsis, M. Persson, and G. Meyer. "Investigating atomic contrast in atomic force microscopy and Kelvin probe force microscopy on ionic systems using functionalized tips". *Phys. Rev. B* **90**, 155455 (2014). DOI: 10.1103/PhysRevB.90.155455.

[67] N. Hauptmann, F. Mohn, L. Gross, G. Meyer, T. Frederiksen, and R. Berndt. "Force and conductance during contact formation to a C60molecule". *New J. Phys.* **14**, 073032 (2012). DOI: 10.1088/1367-2630/14/7/073032.

[68] L. Pauling, L. O. Brockway, and J. Y. Beach. "The Dependence of Interatomic Distance on Single Bond-Double Bond Resonance". *J. Am. Chem. Soc.* **57**, 2705–2709 (1935). DOI: 10.1021/ja01315a105.

[69] J. Sedlar, I. Anđelić, I. Gutman, D. Vukičević, and A. Graovac. "Vindicating the Pauling-bond-order concept". *Chem. Phys. Lett.* **427**, 418–420 (2006). DOI: 10.1016/j.cplett.2006.06.026.

[70] M. P. Boneschanscher, S. K. Hämäläinen, P. Liljeroth, and I. Swart. "Sample Corrugation Affects the Apparent Bond Lengths in Atomic Force Microscopy". *ACS Nano* **8**, 3006–3014 (2014). DOI: 10.1021/nn500317r.

[71] M. Neu, N. Moll, L. Gross, G. Meyer, F. J. Giessibl, and J. Repp. "Image correction for atomic force microscopy images with functionalized tips". *Phys. Rev. B* **89**, 205407 (2014). DOI: 10.1103/PhysRevB.89.205407.

[72] F. Mohn, L. Gross, and G. Meyer. "Measuring the short-range force field above a single molecule with atomic resolution". *Appl. Phys. Lett.* **99**, 053106 (2011). DOI: 10.1063/1.3619829.

[73] J. K. Gimzewski, B. Reihl, J. H. Coombs, and R.R. Schlittler. "Photon emission with the scanning tunneling microscope". *Z. Phys. B* **72**, 497–501 (1988). DOI: 10.1007/BF01314531.

[74] I.I. Smolyaninov. "Photon emission from a layer of copper phthalocyanine molecules on a gold (111) film surface induced by STM". *Surf. Sci.* **364**, 79–88 (1996). DOI: 10.1016/0039-6028(96)00581-X.

[75] D. Fujita, T. Ohgi, W.-L. Deng, H. Nejo, T. Okamoto, S. Yokoyama, K. Kamikado, and S. Mashiko. "STM induced photon emission from adsorbed porphyrin molecules on a Cu(100) surface in ultrahigh vacuum". *Surf. Sci.* **454–456**, 1021–1025 (2000). DOI: 10.1016/S0039-6028(00)00274-0.

[76] G. Hoffmann, L. Libioulle, and R. Berndt. "Tunneling-Induced Luminescence from Adsorbed Organic Molecules with Submolecular Lateral Resolution". *Phys. Rev. B* **65**, 212107 (2002). DOI: 10.1103/PhysRevB.65.212107.

[77] N. Nilius, N. Ernst, and H.-J. Freund. "Photon Emission Spectroscopy of Individual Oxide-Supported Silver Clusters in a Scanning Tunneling Microscope". *Phys. Rev. Lett.* **84**, 3994–3997 (2000). DOI: 10.1103/PhysRevLett.84.3994.

[78] B. Doppagne, M. C. Chong, H. Bulou, A. Boeglin, F. Scheurer, and G. Schull. "Electrofluorochromism at the Single-Molecule Level". *Science* **361**, 251–255 (2018). DOI: 10.1126/science.aat1603.

[79] A. Yu, S. Li, H. Wang, S. Chen, R. Wu, and W. Ho. "Visualization of Nanoplasmonic Coupling to Molecular Orbital in Light Emission Induced by Tunneling Electrons". *Nano Lett.* **18**, 3076–3080 (2018). DOI: 10.1021/acs.nanolett.8b00613.

[80] J. Kröger, B. Doppagne, F. Scheurer, and G. Schull. "Fano Description of Single-Hydrocarbon Fluorescence Excited by a Scanning Tunneling Microscope". *Nano Lett.* **18**, 3407–3413 (2018). DOI: 10.1021/acs.nanolett.8b00304.

[81] H. Imada, K. Miwa, M. Imai-Imada, S. Kawahara, K. Kimura, and Y. Kim. "Single-Molecule Investigation of Energy Dynamics in a Coupled Plasmon-Exciton System". *Phys. Rev. Lett.* **119**, 013901 (2017). DOI: 10.1103/PhysRevLett.119.013901.

[82] H. Imada, K. Miwa, M. Imai-Imada, S. Kawahara, K. Kimura, and Y. Kim. "Real-Space Investigation of Energy Transfer in Heterogeneous Molecular Dimers". *Nature* **538**, 364–367 (2016). DOI: 10.1038/nature19765.

[83] Z.-C. Dong, X.-L. Guo, A. S. Trifonov, P. S. Dorozhkin, K. Miki, K. Kimura, S. Yokoyama, and S. Mashiko. "Vibrationally Resolved Fluorescence from Organic Molecules near Metal Surfaces in a Scanning Tunneling Microscope". *Phys. Rev. Lett.* **92**, 086801 (2004). DOI: 10.1103/PhysRevLett.92.086801.

[84] K. Miwa, H. Imada, M. Imai-Imada, K. Kimura, M. Galperin, and Y. Kim. "Many-Body State Description of Single-Molecule Electroluminescence Driven by a Scanning Tunneling Microscope". *Nano Lett.* **19**, 2803–2811 (2019). DOI: 10.1021/acs.nanolett.8b04484.

[85] B. E. A. Saleh and M. C. Teich. *Fundamentals of Photonics*. 1 edition, vol. 90. Wiley-Interscience, 1991, 155455 pages. DOI: 10.1103/PhysRevB.90.155455.

[86] S. A. Maier. *Plasmonics: Fundamentals and Applications*. 1 edition, vol. 90. Springer US, 2007, 155455 pages. DOI: 10.1103/PhysRevB.90.155455.

[87] L.-L. Nian, Y. Wang, and J.-T. Lü. "On the Fano Line Shape of Single Molecule Electroluminescence Induced by a Scanning Tunneling Microscope". *Nano Lett.* **18**, 6826–6831 (2018). DOI: 10.1021/acs.nanolett.8b02706.

[88] J. Lambe and S. L. McCarthy. "Light Emission from Inelastic Electron Tunneling". *Phys. Rev. Lett.* **37**, 923–925 (1976). DOI: 10.1103/PhysRevLett.37.923.

[89] R. W. Rendell, D. J. Scalapino, and B. Mühlschlegel. "Role of Local Plasmon Modes in Light Emission from Small-particle Tunnel Junctions". *Phys. Rev. Lett.* **41**, 1746–1750 (1978). DOI: 10.1103/PhysRevLett.41.1746.

[90] P. Johansson, R. Monreal, and P. Apell. "Theory for light emission from a scanning tunneling microscope". *Phys. Rev. B* **42**, 9210–9213 (1990). DOI: 10.1103/PhysRevB.42.9210.

[91] R. Berndt, J. K. Gimzewski, and P. Johansson. "Inelastic tunneling excitation of tip-induced plasmon modes on noble-metal surfaces". *Phys. Rev. Lett.* **67**, 3796–3799 (1991). DOI: 10.1103/PhysRevLett.67.3796.

[92] L. Novotny and N. van Hulst. "Antennas for Light". *Nat. Photonics* **5**, 53–90 (2011). DOI: 10.1038/nphoton.2010.237.

[93] E. Kazuma, J. Jung, H. Ueba, M. Trenary, and Y. Kim. "Real-space and real-time observation of a plasmon-induced chemical reaction of a single molecule". *Science* **360**, 521–526 (2018). DOI: 10.1126/science.aao0872.

[94] Y. Zhang et al. "Sub-nanometre control of the coherent interaction between a single molecule and a plasmonic nanocavity". *Nat. Commun.* **8**, 1–7 (2017). DOI: 10.1038/ncomms15225.

[95] B. Laks and D. L. Mills. "Photon emission from slightly roughened tunnel junctions". *Phys. Rev. B* **20**, 4962–4980 (1979). DOI: 10.1103/PhysRevB.20.4962.

[96] B. N. J. Persson and A. Baratoff. "Theory of photon emission in electron tunneling to metallic particles". *Phys. Rev. Lett.* **68**, 3224–3227 (1992). DOI: 10.1103/PhysRevLett.68.3224.

[97] G. Hoffmann, R. Berndt, and P. Johansson. "Two-Electron Photon Emission from Metallic Quantum Wells". *Phys. Rev. Lett.* **90**, 046803 (2003). DOI: 10.1103/PhysRevLett.90.046803.

[98] G. Schull, N. Néel, P. Johansson, and R. Berndt. "Electron-Plasmon and Electron-Electron Interactions at a Single Atom Contact". *Phys. Rev. Lett.* **102**, 057401 (2009). DOI: 10.1103/PhysRevLett.102.057401.

[99] S. Liu, M. Wolf, and T. Kumagai. "Plasmon-Assisted Resonant Electron Tunneling in a Scanning Tunneling Microscope Junction". *Phys. Rev. Lett.* **121**, 226802 (2018). DOI: 10.1103/PhysRevLett.121.226802.

[100] P. K. Hansma and H. P. Broida. "Light emission from gold particles excited by electron tunneling". *Appl. Phys. Lett.* **32**, 545–547 (1978). DOI: 10.1063/1.90123.

[101] R. Berndt, J. K. Gimzewski, and P. Johansson. "Electromagnetic interactions of metallic objects in nanometer proximity". *Phys. Rev. Lett.* **71**, 3493–3496 (1993). DOI: 10.1103/PhysRevLett.71.3493.

[102] G. Hoffmann, J. Aizpurua, P. Apell, and R. Berndt. "Influence of tip geometry in light emission from the scanning tunnelling microscope". *Surf. Sci.* **482**, 1159–1162 (2001). DOI: 10.1016/S0039-6028(00)01079-7.

[103] N. L. Schneider, G. Schull, and R. Berndt. "Optical Probe of Quantum Shot-Noise Reduction at a Single-Atom Contact". *Phys. Rev. Lett.* **105**, 026601 (2010). DOI: 10.1103/PhysRevLett.105.026601.

[104] Z. C. Dong et al. "Generation of molecular hot electroluminescence by resonant nanocavity plasmons". *Nat. Photonics* **4**, 50 (2010). DOI: 10.1038/nphoton.2009.257.

[105] G. Tian, J.-C. Liu, and Y. Luo. "Density-Matrix Approach for the Electroluminescence of Molecules in a Scanning Tunneling Microscope". *Phys. Rev. Lett.* **106**, 177401 (2011). DOI: 10.1103/PhysRevLett.106.177401.

[106] M. C. Chong, G. Reecht, H. Bulou, A. Boeglin, F. Scheurer, F. Mathevet, and G. Schull. "Narrow-Line Single-Molecule Transducer between Electronic Circuits and Surface Plasmons". *Phys. Rev. Lett.* **116**, 036802 (2016). DOI: 10.1103/PhysRevLett.116.036802.

[107] H.-F. Wang, X.-G. Li, and Z.-C. Dong. "Role of nanocavity plasmons in tunneling electron induced light emission on and near a molecule". *Chin. J. Chem. Phys.* **31**, 263–268 (2018). DOI: 10.1063/1674-0068/31/cjcp1802024.

[108] J. Doležal, P. Merino, J. Redondo, L. Ondič, A. Cahlík, and M. Švec. "Charge Carrier Injection Electroluminescence with CO-Functionalized Tips on Single Molecular Emitters". *Nano Lett.* **19**, 8605–8611 (2019). DOI: 10.1021/acs.nanolett.9b03180.

[109] E. M. Purcell, R. V. Pound, and N. Bloembergen. "Nuclear Magnetic Resonance Absorption in Hydrogen Gas". *Phys. Rev.* **70**, 986–987 (1946). DOI: 10.1103/PhysRev.70.986.

[110] G. Meyer. "A simple low-temperature ultrahigh-vacuum scanning tunneling microscope capable of atomic manipulation". *Rev. Sci. Instrum.* **67**, 2960–2965 (1996). DOI: 10.1063/1.1147080.

[111] CreaTec Fischer & Co. GmbH. *LT-STM/AFM System*. 2014. DOI: 10.1103/PhysRevB.90.155455. URL: https://createc.de/LT-STMAFM/. (accessed: 05.08.2020).

[112] K. Besocke. "An easily operable scanning tunneling microscope". *Surf. Sci.* **181**, 145–153 (1987). DOI: https://doi.org/10.1016/0039-6028(87)90151-8.

[113] J. Frohn, J. F. Wolf, K. Besocke, and M. Teske. "Coarse tip distance adjustment and positioner for a scanning tunneling microscope". *Rev. Sci. Instrum.* **60**, 1200–1201 (1989). DOI: 10.1063/1.1140287.

[114] IBM Research. *Sensor*. 2014. DOI: 10.1103/PhysRevB.90.155455. URL: https://www.flickr.com/photos/ibm_research_zurich/23874244373/in/photostream/. (accessed: 05.11.2020).

[115] F. J. Giessibl. *Sensor for noncontact profiling of a surface*. US Patent 8,393,009. 2013. DOI: 10.1103/PhysRevB.90.155455.

[116] R. Bennewitz, V. Barwich, M. Bammerlin, C. Loppacher, M. Guggisberg, A. Baratoff, E. Meyer, and H.-J. Güntherodt. "Ultrathin films of NaCl on Cu(111): a LEED and dynamic force microscopy study". *Surf. Sci.* **438**, 289–296 (1999). DOI: https://doi.org/10.1016/S0039-6028(99)00586-5.

[117] R. J. Beuhler, E. Flanigan, L. J. Greene, and L. Friedman. "Proton transfer mass spectrometry of peptides. Rapid heating technique for underivatized peptides containing arginine". *J. Am. Chem. Soc.* **96**, 3990–3999 (1974). DOI: 10.1021/ja00819a043.

[118] T. Zambelli, P. Jiang, J. Lagoute, S. E. Grillo, S. Gauthier, A. Gourdon, and C. Joachim. "Deformation of a 3.7-nm long molecular wire at a metallic step edge". *Phys. Rev. B* **66**, 075410 (2002). DOI: 10.1103/PhysRevB.66.075410.

[119] J. E. Sader and S. P. Jarvis. "Accurate formulas for interaction force and energy in frequency modulation force spectroscopy". *Appl. Phys. Lett.* **84**, 1801–1803 (2004). DOI: 10.1063/1.1667267.

[120] Teledyne Princeton Instruments. *LightField Software*. 2014. DOI: 10.1103/PhysRevB.90.155455. URL: https://www.princetoninstruments.com/products/software-family/lightfield. (accessed: 26.03.2021).

[121] MathWorks. *Outlier removal using Hampel identifier*. 2014. DOI: 10.1103/PhysRevB.90.155455. URL: https://ch.mathworks.com/help/signal/ref/hampel.html. (accessed: 05.26.2020).

[122] P. Hohenberg and W. Kohn. "Inhomogeneous Electron Gas". *Phys. Rev.* **136**, B864–B871 (1964). DOI: 10.1103/PhysRev.136.B864.

[123] W. Kohn and L. J. Sham. "Self-Consistent Equations Including Exchange and Correlation Effects". *Phys. Rev.* **140**, A1133–A1138 (1965). DOI: 10.1103/PhysRev.140.A1133.

[124] N. Argaman and G. Makov. "Density functional theory: An introduction". *American Journal of Physics* **68**, 69–79 (2000). DOI: 10.1119/1.19375.

[125] V. Blum, R. Gehrke, F. Hanke, P. Havu, V. Havu, X. Ren, K. Reuter, and M. Scheffler. "Ab initio molecular simulations with numeric atom-centered orbitals". *Comput. Phys. Commun.* **180**, 2175–2196 (2009). DOI: https://doi.org/10.1016/j.cpc.2009.06.022.

[126] J. Heyd, G. E. Scuseria, and M. Ernzerhof. "Hybrid functionals based on a screened Coulomb potential". *J. Chem. Phys.* **118**, 8207–8215 (2003). DOI: 10.1063/1.1564060.

[127] J. P. Perdew, K. Burke, and M. Ernzerhof. "Generalized Gradient Approximation Made Simple". *Phys. Rev. Lett.* **77**, 3865–3868 (1996). DOI: 10.1103/PhysRevLett.77.3865.

[128] F. Schulz, M. Commodo, K. Kaiser, G. De Falco, P. Minutolo, G. Meyer, A. D'Anna, and L. Gross. "Insights into Incipient Soot Formation by Atomic Force Microscopy". *Proc. Combust. Inst.* **37**, 885–892 (2019). DOI: 10.1016/j.proci.2018.06.100.

[129] M. Commodo, K. Kaiser, G. De Falco, P. Minutolo, F. Schulz, A. D'Anna, and L. Gross. "On the early stages of soot formation: Molecular structure elucidation by high-resolution atomic force microscopy". *Combust. Flame* **205**, 154–164 (2019). DOI: https://doi.org/10.1016/j.combustflame.2019.03.042.

[130] P. A. Peaden, M. L. Lee, Y. Hirata, and M. Novotny. "High-Performance Liquid Chromatographic Separation of High-Molecular-Weight Polycyclic Aromatic Compounds in Carbon Black". *Anal. Chem.* **52**, 2268–2271 (1980). DOI: 10.1021/ac50064a008.

[131] W. B. Wilson, H. V. Hayes, L. C. Sander, A. D. Campiglia, and S. A. Wise. "Qualitative characterization of SRM 1597a coal tar for polycyclic aromatic hydrocarbons and methyl-substituted derivatives via normal-phase liquid chromatography and gas chromatography/mass spectrometry". *Anal. Bioanal. Chem.* **409**, 5171–5183 (2017). DOI: 10.1007/s00216-017-0464-x.

[132] S. Fatayer et al. "Atomic Force Microscopy Identifying Fuel Pyrolysis Products and Directing the Synthesis of Analytical Standards". *J. Am. Chem. Soc.* **140**, 8156–8161 (2018). DOI: 10.1021/jacs.8b02525.

[133] B. Schuler et al. "Heavy Oil Based Mixtures of Different Origins and Treatments Studied by Atomic Force Microscopy". *Energy Fuels* **31**, 6856–6861 (2017). DOI: 10.1021/acs.energyfuels.7b00805.

[134] S. Fatayer, A. I. Coppola, F. Schulz, B. D. Walker, T. A. Broek, G. Meyer, E. R. M. Druffel, M. McCarthy, and L. Gross. "Direct Visualization of Individual Aromatic Compound Structures in Low Molecular Weight Marine Dissolved Organic Carbon". *Geophys. Res. Lett.* **45**, 5590–5598 (2018). DOI: 10.1029/2018GL077457.

[135] Y. Zhang et al. "Elucidating the Geometric Substitution of Petroporphyrins by Spectroscopic Analysis and Atomic Force Microscopy Molecular Imaging". *Energy Fuels* **33**, 6088–6097 (2019). DOI: 10.1021/acs.energyfuels.9b00816.

[136] R. Hoffmann, L. N. Kantorovich, A. Baratoff, H. J. Hug, and H.-J. Güntherodt. "Sublattice Identification in Scanning Force Microscopy on Alkali Halide Surfaces". *Phys. Rev. Lett.* **92**, 146103 (2004). DOI: 10.1103/PhysRevLett.92.146103.

[137] Y. Sugimoto, P. Pou, M. Abe, P. Jelinek, R. Pérez, S. Morita, and Ó. Custance. "Chemical identification of individual surface atoms by atomic force microscopy". *Nature* **446**, 64–67 (2007). DOI: 10.1038/nature05530.

[138] N. Moll, L. Gross, F. Mohn, A. Curioni, and G. Meyer. "A simple model of molecular imaging with noncontact atomic force microscopy". *New J. Phys.* **14**, 083023 (2012). DOI: 10.1088/1367-2630/14/8/083023.

[139] F. Schulz, J. Ritala, O. Krejčí, A. P. Seitsonen, A. S. Foster, and P. Liljeroth. "Elemental Identification by Combining Atomic Force Microscopy and Kelvin Probe Force Microscopy". *ACS Nano* **12**, 5274–5283 (2018). DOI: 10.1021/acsnano.7b08997.

[140] M. Ellner, P. Pou, and R. Pérez. "Molecular Identification, Bond Order Discrimination, and Apparent Intermolecular Features in Atomic Force Microscopy Studied with a Charge Density Based Method". *ACS Nano* **13**, 786–795 (2019). DOI: 10.1021/acsnano.8b08209.

[141] B. Schuler et al. "Characterizing aliphatic moieties in hydrocarbons with atomic force microscopy". *Chem. Sci.* **8**, 2315–2320 (2017). DOI: 10.1039/C6SC04698C.

[142] L. Grill. "Large molecules on surfaces: deposition and intramolecular STM manipulation by directional forces". *J. Phys. Condens. Matter* **22**, 084023 (2010). DOI: 10.1088/0953-8984/22/8/084023.

[143] F. Albrecht, N. Pavliček, C. Herranz-Lancho, M. Ruben, and J. Repp. "Characterization of a Surface Reaction by Means of Atomic Force Microscopy". *J. Am. Chem. Soc.* **137**, 7424–7428 (2015). DOI: 10.1021/jacs.5b03114.

[144] T. S. Totton, A. J. Misquitta, and M. Kraft. "A quantitative study of the clustering of polycyclic aromatic hydrocarbons at high temperatures". *Phys. Chem. Chem. Phys.* **14**, 4081–4094 (2012). DOI: 10.1039/C2CP23008A.

[145] K. O. Johansson et al. "Formation and emission of large furans and oxygenated hydrocarbons from flames". *Proc. Natl. Acad. Sci.* **113**, 8374–8379 (2016). DOI: 10.1073/pnas.1604772113.

[146] E. K. Y. Yapp, C. G. Wells, J. Akroyd, S. Mosbach, R. Xu, and M. Kraft. "Modelling PAH curvature in laminar premixed flames using a detailed population balance model". *Combust. Flame* **176**, 172–180 (2017). DOI: 10.1016/j.combustflame.2016.10.004.

[147] L. Pascazio, M. Sirignano, and A. D'Anna. "Simulating the morphology of clusters of polycyclic aromatic hydrocarbons: The influence of the intermolecular potential". *Combust. Flame* **185**, 53–62 (2017). DOI: 10.1016/j.combustflame.2017.07.003.

[148] A. D'Anna, A. Violi, A. D'Alessio, and A. F. Sarofim. "A reaction pathway for nanoparticle formation in rich premixed flames". *Combust. Flame* **127**, 1995–2003 (2001). DOI: https://doi.org/10.1016/S0010-2180(01)00303-0.

[149] M. Commodo, G. De Falco, A. Bruno, C. Borriello, P. Minutolo, and A. D'Anna. "Physicochemical evolution of nascent soot particles in a laminar premixed flame: from nucleation to early growth". *Combust. Flame* **162**, 3854–3863 (2015). DOI: https://doi.org/10.1016/j.combustflame.2015.07.022.

[150] F. Carbone, M. Attoui, and A. Gomez. "Challenges of measuring nascent soot in flames as evidenced by high-resolution differential mobility analysis". *Aerosol Sci. Tech.* **50**, 740–757 (2016). DOI: 10.1080/02786826.2016.1179715.

[151] Q. Tang, R. Cai, X. You, and J. Jiang. "Nascent soot particle size distributions down to 1nm from a laminar premixed burner-stabilized stagnation ethylene flame". *Proc. Combust. Inst.* **36**, 993–1000 (2017). DOI: 10.1016/j.proci.2016.08.085.

[152] P. Elvati and A. Violi. "Thermodynamics of poly-aromatic hydrocarbon clustering and the effects of substituted aliphatic chains". *Proc. Combust. Inst.* **34**, 1837–1843 (2013). DOI: https://doi.org/10.1016/j.proci.2012.07.030.

[153] M. Frenklach, D. W. Clary, W. C. Gardiner, and S. E. Stein. "Detailed kinetic modeling of soot formation in shock-tube pyrolysis of acetylene". *Symp. (Int.) Combust.* **20**, 887–901 (1985). DOI: 10.1016/S0082-0784(85)80578-6.

[154] A. D'Anna. "Combustion-formed nanoparticles". *Proc. Combust. Inst.* **32**, 593–613 (2009). DOI: https://doi.org/10.1016/j.proci.2008.09.005.

[155] Z. Mou, K. Uchida, T. Kubo, and M. Kertesz. "Evidence of $\sigma$- and $\pi$-Dimerization in a Series of Phenalenyls". *J. Am. Chem. Soc.* **136**, 18009–18022 (2014). DOI: 10.1021/ja509243p.

[156] K. Kaiser, L. Scriven, F. Schulz, P. Gawel, L. Gross, and H. Anderson. "An sp-hybridized molecular carbon allotrope, cyclo[18]carbon". *Science* **365**, 1299–1301 (2019). DOI: 10.1126/science.aay1914.

[157] L. M. Scriven, K. Kaiser, F. Schulz, A. J. Sterling, S. L. Woltering, P. Gawel, K. E. Christensen, H. L. Anderson, and L. Gross. "Synthesis of Cyclo [18] carbon via Debromination of C18Br6". *J. Am. Chem. Soc.* **142**, 12921–12924 (2020). DOI: 10.1103/PhysRevB.90.155455.

[158] F. Albrecht, D. Rey, S. Fatayer, F. Schulz, D. Pérez, D. Peña, and L. Gross. "Intramolecular Coupling of Terminal Alkynes by Atom Manipulation". *Angew. Chem. Int. Ed.* **59**, 22989–22993 (2020). DOI: https://doi.org/10.1002/anie.202009200.

[159] Z. Majzik, N. Pavliček, M. Vilas-Varela, D. Pérez, N. Moll, E. Guitián, G. Meyer, D. Peña, and L. Gross. "Studying an antiaromatic polycyclic hydrocarbon adsorbed on different surfaces". *Nat. Commun.* **9**, 1198 (2018). DOI: 10.1038/s41467-018-03368-9.

[160] R. Hoffmann. "Extended Hückel theory–V: Cumulenes, polyenes, polyacetylenes and Cn". *Tetrahedron* **22**, 521–538 (1966). DOI: 10.1016/0040-4020(66)80020-0.

[161] F. Diederich, Y. Rubin, C. B. Knobler, R. L. Whetten, K. E. Schriver, K. N. Houk, and Y. Li. "All-carbon molecules: evidence for the generation of cyclo [18] carbon from a stable organic precursor". *Science* **245**, 1088–1090 (1989). DOI: 10.1126/science.245.4922.1088.

[162] F. Diederich and M. Kivala. "All-carbon scaffolds by rational design". *Adv. Mater.* **22**, 803–812 (2010). DOI: 10.1002/adma.200902623.

[163] S. W. McElvany, M. M. Ross, N. S. Goroff, and F. Diederich. "Cyclocarbon coalescence: Mechanisms for tailor-made fullerene formation". *Science* **259**, 1594–1596 (1993). DOI: 10.1126/science.259.5101.1594.

[164] G. Von Helden, N. G. Gotts, and M. T. Bowers. "Experimental evidence for the formation of fullerenes by collisional heating of carbon rings in the gas phase". *Nature* **363**, 60–63 (1993). DOI: 10.1038/363060a0.

[165] P. W. Fowler, N. Mizoguchi, D. E. Bean, and R. W. A. Havenith. "Double Aromaticity and Ring Currents in All-Carbon Rings". *Chem. Eur. J.* **15**, 6964–6972 (2009). DOI: 10.1002/chem.200900322.

[166] V. Parasuk, J. Almlof, and M. W. Feyereisen. "The [18] all-carbon molecule: Cumulene or polyacetylene?" *J. Am. Chem. Soc.* **113**, 1049–1050 (1991). DOI: 0002-7863/91/1513-1049S02.50/0.

[167] C. Neiss, E. Trushin, and A. Görling. "The Nature of One-Dimensional Carbon: Polyynic versus Cumulenic". *ChemPhysChem* **15**, 2497–2502 (2014). DOI: 10.1103/PhysRevB.90.155455.

[168] A. Nandi, E. Solel, and S. Kozuch. "Carbon Tunneling in the Automerization of Cyclo[18]carbon". *Chem. Eur. J.* **26**, 625–628 (2020). DOI: 10.1002/chem.201904929.

[169] D. A. Plattner and K. N. Houk. "C18 Is a Polyyne". *J. Am. Chem. Soc.* **117**, 4405–4406 (1995). DOI: 10.1021/ja00120a026.

[170] T. Torelli and L. Mitas. "Electron correlation in C 4 n+ 2 carbon rings: aromatic versus dimerized structures". *Phys. Rev. Lett.* **85**, 1702 (2000). DOI: 10.1103/PhysRevLett.85.1702.

[171] S. Arulmozhiraja and T. Ohno. "CCSD calculations on $C_{14}$, $C_{18}$, and $C_{22}$ carbon clusters". *J. Chem. Phys* **128**, 114301 (2008). DOI: 10.1063/1.2838200.

[172] Y. Rubin, C. B. Knobler, and F. Diederich. "Synthesis and crystal structure of a stable hexacobalt complex of cyclo[18]carbon". *J. Am. Chem. Soc.* **112**, 4966–4968 (1990). DOI: 10.1021/ja00168a056.

[173] Y. Rubin, M. Kahr, C. B. Knobler, F. Diederich, and C. L. Wilkins. "The higher oxides of carbon C8nO2n (n= 3-5): synthesis, characterization, and X-ray crystal structure. Formation of cyclo[n]carbon ions Cn+ (n= 18, 24), Cn- (n= 18, 24, 30), and higher carbon ions including C60+ in laser desorption Fourier transform mass spectrometric experiments". *J. Am. Chem. Soc.* **113**, 495–500 (1991). DOI: 10.1021/ja00002a017.

[174] Y. Tobe, H. Matsumoto, K. Naemura, Y. Achiba, and T. Wakabayashi. "Generation of Cyclocarbons with 4n Carbon Atoms (C12, C16, and C20) by [2+2] Cycloreversion of Propellane-Annelated Dehydroannulenes". *Angew. Chem. Int. Ed. Engl.* **35**, 1800–1802 (1996). DOI: 10.1002/anie.199618001.

[175] A. E. Boguslavskiy, H. Ding, and J. P. Maier. "Gas-phase electronic spectra of C18 and C22 rings". *J. Chem. Phys.* **123**, 034305 (2005). DOI: 10.1063/1.1961564.

[176] N. Pavliček and L. Gross. "Generation, Manipulation and Characterization of Molecules by Atomic Force Microscopy". *Nat. Rev. Chem.* **1**, 1–11 (2017). DOI: 10.1038/s41570-016-0005.

[177] A. Riss et al. "Local electronic and chemical structure of oligo-acetylene derivatives formed through radical cyclizations at a surface". *Nano Lett.* **14**, 2251–2255 (2014). DOI: 10.1021/nl403791q.

[178] V. Schendel, B. Borca, I. Pentegov, T. Michnowicz, U. Kraft, H. Klauk, P. Wahl, U. Schlickum, and K. Kern. "Remotely Controlled Isomer Selective Molecular Switching". *Nano Lett.* **16**, 93–97 (2016). DOI: 10.1021/acs.nanolett.5b02974.

[179] J. N. Ladenthin, L. Grill, S. Gawinkowski, S. Liu, J. Waluk, and T. Kumagai. "Hot Carrier-Induced Tautomerization within a Single Porphycene Molecule on Cu(111)". *ACS Nano* **9**, 7287–7295 (2015). DOI: 10.1021/acsnano.5b02147.

[180] N. Pavliček, Z. Majzik, S. Collazos, G. Meyer, D. Pérez, E. Guitián, D. Peña, and L. Gross. "Generation and Characterization of a meta-Aryne on Cu and NaCl Surfaces". *ACS Nano* **11**, 10768–10773 (2017). DOI: 10.1021/acsnano.7b06137.

[181] N. Pavliček, B. Fleury, M. Neu, J. Niedenführ, C. Herranz-Lancho, M. Ruben, and J. Repp. "Atomic force microscopy reveals bistable configurations of dibenzo [a, h] thianthrene and their interconversion pathway". *Phys. Rev. Lett.* **108**, 086101 (2012). DOI: 10.1103/PhysRevLett.108.086101.

[182] N. Pavliček, C. Herranz-Lancho, B. Fleury, M. Neu, J. Niedenführ, M. Ruben, and J. Repp. "High-resolution scanning tunneling and atomic force microscopy of stereochemically resolved dibenzo[a,h]thianthrene molecules". *Phys. Status Solidi B* **250**, 2424–2430 (2013). DOI: 10.1002/pssb.201349229.

[183] T. Leoni, O. Guillermet, H. Walch, V. Langlais, A. Scheuermann, J. Bonvoisin, and S. Gauthier. "Controlling the Charge State of a Single Redox Molecular Switch". *Phys. Rev. Lett.* **106**, 216103 (2011). DOI: 10.1103/PhysRevLett.106.216103.

[184] P. Muller. "Glossary of terms used in physical organic chemistry (IUPAC Recommendations 1994)". *Pure & Appl. Chem.* **66**, 1077–1184 (1994). DOI: 10.1351/pac199466051077.

[185] D. K. Mandal. "Chapter 3 - Pericyclic Reactions: Introduction, Classification and the Woodward-Hoffmann Rules". In: *Pericyclic Chemistry*. Ed. by D. K. Mandal. 1st ed. Vol. 90. Elsevier, 2018, pp. 63–106. DOI: 10.1016/B978-0-12-814958-4.00003-9.

[186] K. Kaiser, L. Gross, and F. Schulz. "A Single-Molecule Chemical Reaction Studied by High-Resolution Atomic Force Microscopy and Scanning Tunneling Microscopy Induced Light Emission". *ACS Nano* **13**, 6947–6954 (2019). DOI: 10.1021/acsnano.9b01852.

[187] R. Zhang et al. "Chemical Mapping of a Single Molecule by Plasmon-Enhanced Raman Sattering". *Nature* **498**, 82 (2013). DOI: 10.1038/nature12151.

[188] S. Jiang, Y. Zhang, R. Zhang, C. Hu, M. Liao, Y. Luo, J. Yang, Z. Dong, and J. G. Hou. "Distinguishing Adjacent Molecules on a Surface Using Plasmon-Enhanced Raman Scattering". *Nat. Nanotechnol.* **10**, 865 (2015). DOI: 10.1038/NNANO.2015.17.

[189] Y. Zhang, R. Zhang, S. Jiang, Y. Zhang, and Z.-C. Dong. "Probing the Adsorption Configurations of Small Molecules on Surfaces by Single-Molecule Tip-Enhanced Raman Spectroscopy". *ChemPhysChem* **20**, 37–41 (2019). DOI: 10.1002/cphc.201800861.

[190] L. Gross, N. Moll, F. Mohn, A. Curioni, G. Meyer, F. Hanke, and M. Persson. "High-Resolution Molecular Orbital Imaging Using a p-Wave STM Tip". *Phys. Rev. Lett.* **107**, 086101 (2011). DOI: 10.1103/PhysRevLett.107.086101.

[191] F. Schulz, M. Ijäs, R. Drost, S. K. Hämäläinen, A. Harju, A. P. Seitsonen, and P. Liljeroth. "Many-Body Transitions in a Single Molecule Visualized by Scanning Tunnelling Microscopy". *Nat. Phys.* **11**, 229–234 (2015). DOI: 10.1038/nphys3212.

[192] F. Schulz et al. "Precursor Geometry Determines the Growth Mechanism in Graphene Nanoribbons". *J. Phys. Chem. C* **121**, 2896–2904 (2017). DOI: 10.1021/acs.jpcc.6b12428.

[193] A. Riss et al. "Imaging Single-Molecule Reaction Intermediates Stabilized by Surface Dissipation and Entropy". *Nat. Chem.* **8**, 678–683 (2016). DOI: 10.1038/nchem.2506.

[194] P. Ruffieux et al. "On-Surface Synthesis of Graphene Nanoribbons with Zigzag Edge Topology". *Nature* **531**, 489 (2016). DOI: 10.1038/nature17151.

[195] A. Zhao et al. "Controlling the Kondo Effect of an Adsorbed Magnetic Ion Through Its Chemical Bonding". *Science* **309**, 1542–1544 (2005). DOI: 10.1126/science.1113449.

[196] M. G. Walter, A. B. Rudine, and C. C. Wamser. "Porphyrins and Phthalocyanines in Solar Photovoltaic Cells". *J. Porphyr. Phthalocyanines* **14**, 759–792 (2010). DOI: 10.1142/S1088424610002689.

[197] K. Kuhnke, C. Große, P. Merino, and K. Kern. "Atomic-Scale Imaging and Spectroscopy of Electroluminescence at Molecular Interfaces". *Chem. Rev.* **117**, 5174–5222 (2017). DOI: 10.1021/acs.chemrev.6b00645.

[198] M. Casarin and S. Carlotto. ""Pigments of Life", Molecules Well Suited to Investigate Metal-Ligand Symmetry-Restricted Covalency". *Eur. J. Inorg. Chem.* **2018**, 3145–3155 (2018). DOI: 10.1002/ejic.201800480.

[199] Y. L. Pan, Y. J. Wu, L. B. Chen, Y. Y. Zhao, Y. H. Shen, F. M. Li, S. Y. Shen, and D. H. Huang. "Structure and Spectroscopic Characterization of Polycrystalline Vanadyl Phthalocyanine (VOPc) Films Fabricated by Vacuum Deposition". *Appl. Phys. A* **66**, 569–573 (1998). DOI: 10.1103/PhysRevB.90.155455.

[200] D. Wróbel, A. Boguta, and R. M. Ion. "Spectroscopic and Photoelectric Studies of Phthalocyanines in Polyvinyl Alcohol for Application in Solar Energy Conversion". *Int. J. Photoenergy* **2**, 87–96 (2000). DOI: 10.1155/S1110662X0000012X.

[201] G. Dujardin, R. E. Walkup, and PH. Avouris. "Dissociation of Individual Molecules with Electrons from the Tip of a Scanning Tunneling Microscope". *Science* **255**, 1232–1235 (1992). DOI: 10.1126/science.255.5049.1232.

[202] F. Albrecht, M. Neu, C. Quest, I. Swart, and J. Repp. "Formation and Characterization of a Molecule-Metal-Molecule Bridge in Real Space". *J. Am. Chem. Soc.* **135**, 9200–9203 (2013). DOI: 10.1021/ja404084p.

[203] P. J. Blowey et al. "The Structure of VOPc on Cu(111): Does V=O Point Up, or Down, or Both?" *J. Phys. Chem. C* **123**, 8101–8111 (2019). DOI: 10.1021/acs.jpcc.8b07530.

[204] T. Niu, J. Zhang, and W. Chen. "Molecular Ordering and Dipole Alignment of Vanadyl Phthalocyanine Monolayer on Metals: The Effects of Interfacial Interactions". *J. Phys. Chem. C* **118**, 4151–4159 (2014). DOI: 10.1021/jp4101653.

[205] J. Zhang, Z. Wang, T. Niu, Z. Li, and W. Chen. "Single Molecule Tunneling Spectroscopy Investigation of Reversibly Switched Dipolar Vanadyl Phthalocyanine on Graphite". *Appl. Phys. Lett.* **104**, 113506 (2014). DOI: 10.1063/1.4869115.

[206] K. Eguchi, T. Nakagawa, Y. Takagi, and T. Yokoyama. "Direct Synthesis of Vanadium Phthalocyanine and Its Electronic and Magnetic States in Monolayers and Multilayers on Ag(111)". *J. Phys. Chem. C* **119**, 9805–9815 (2015). DOI: 10.1021/jp512935v.

[207] B. de la Torre et al. "Non-Covalent Control of Spin-State in Metal-Organic Complex by Positioning on n-Doped Graphene". *Nat. Comm.* **9**, 2831 (2018). DOI: 10.1038/s41467-018-05163-y.

[208] T. Chutora, B. de la Torre, P. Mutombo, J. Hellerstedt, J. Kopeček, P. Jelínek, and M. Švec. "Nitrous Oxide as an Effective AFM Tip Functionalization: a Comparative Study". *Beilstein J. Nanotechnol.* **10**, 315–321 (2019). DOI: 10.3762/bjnano.10.30.

[209] R. Pawlak, S. Fremy, S. Kawai, T. Glatzel, H. Fang, L.-A. Fendt, F. Diederich, and E. Meyer. "Directed Rotations of Single Porphyrin Molecules Controlled by Localized Force Spectroscopy". *ACS Nano* **6**, 6318–6324 (2012). DOI: 10.1021/nn301774d.

[210] J. Schaffert, M. C. Cottin, A. Sonntag, H. Karacuban, C. A. Bobisch, N. Lorente, J.-P. Gauyacq, and R. Möller. "Imaging the Dynamics of Individually Adsorbed Molecules". *Nat. Mater.* **12**, 223 (2013). DOI: 10.1038/nmat3527.

[211] K. Moth-Poulsen and T. Bjørnholm. "Molecular Electronics with Single Molecules in Solid-State Devices". *Nat. Nanotechnol.* **4**, 551 (2009). DOI: 10.1038/nnano.2009.176.

[212] F. Manke, J. M. Frost, V. Vaissier, J. Nelson, and P. R. F. Barnes. "Influence of a nearby Substrate on the Reorganization Energy of Hole Exchange between Dye Molecules". *Phys. Chem. Chem. Phys.* **17**, 7345–7354 (2015). DOI: 10.1039/C4CP06078D.

[213] Ping Yu, N. Kocić, J. Repp, B. Siegert, and A. Donarini. "Apparent Reversal of Molecular Orbitals Reveals Entanglement". *Phys. Rev. Lett.* **119**, 056801 (2017). DOI: 10.1103/PhysRevLett.119.056801.

[214] Mikko M. Ervasti, Fabian Schulz, Peter Liljeroth, and Ari Harju. "Single- and Many-Particle Description of Scanning Tunneling Spectroscopy". *J. Electron Spectros. Relat. Phenomena* **219**, 63–71 (2017). DOI: 10.1016/j.elspec.2016.11.004.

[215] Özer Bekaroğlu. *Functional Phthalocyanine Molecular Materials*. 1 edition, vol. 90. Springer Science & Business Media, 2010, 155455 pages. DOI: 10.1103/PhysRevB.90.155455.

[216] A. T. Davidson. "The Effect of the Metal Atom on the Absorption Spectra of Phthalocyanine Films". *J. Chem. Phys.* **77**, 168–172 (1982). DOI: 10.1063/1.443636.

[217] M.-S. Liao and S. Scheiner. "Electronic Structure and Bonding in Metal Phthalocyanines, Metal=Fe, Co, Ni, Cu, Zn, Mg". *J. Chem. Phys.* **114**, 9780–9791 (2001). DOI: 10.1063/1.1367374.

[218] Tebello N. "Effects of Substituents on the Photochemical and Photophysical Properties of Main Group Metal Phthalocyanines". *Coord. Chem. Rev.* **251**, 1707–1722 (2007). DOI: 10.1016/j.ccr.2006.11.011.

[219] J. W. Perry, K. Mansour, S. R. Marder, K. J. Perry, D. Alvarez, and I. Choong. "Enhanced Reverse Saturable Absorption and Optical Limiting in Heavy-Atom-Substituted Phthalocyanines". *Opt. Lett.* **19**, 625–627 (1994). DOI: 10.1364/OL.19.000625.

[220] B. Schuler, G. Meyer, D. Peña, O. C. Mullins, and L. Gross. "Unraveling the Molecular Structures of Asphaltenes by Atomic Force Microscopy". *J. Am. Chem. Soc.* **137**, 9870–9876 (2015). DOI: 10.1021/jacs.5b04056.

[221] A. Tkatchenko and M. Scheffler. "Accurate Molecular Van Der Waals Interactions from Ground-State Electron Density and Free-Atom Reference Data". *Phys. Rev. Lett.* **102**, 073005 (2009). DOI: 10.1103/PhysRevLett.102.073005.

[222] M. Ellner, N. Pavliček, P. Pou, B. Schuler, N. Moll, G. Meyer, L. Gross, and R. Peréz. "The Electric Field of CO Tips and Its Relevance for Atomic Force Microscopy". *Nano Lett.* **16**, 1974–1980 (2016). DOI: 10.1021/acs.nanolett.5b05251.

[223] J. van der Lit, F. Di Cicco, P. Hapala, P. Jelinek, and I. Swart. "Submolecular Resolution Imaging of Molecules by Atomic Force Microscopy: The Influence of the Electrostatic Force". *Phys. Rev. Lett.* **116**, 096102 (2016). DOI: 10.1103/PhysRevLett.116.096102.

# List of Figures

# List of Tables

# Acknowledgments

At this point I want to thank all the people without whom this thesis but also this chapter of my life would not have been possible. And since this is solely dedicated to them, this small section is going to be bilingual.

I want to thank Leo Gross and Jascha Repp for accepting me as their PhD student.

I am grateful for the opportunity to work, spend time with, and learn from the great colleagues I had throughout my time at IBM Research. Leo, you managed to keep the balance between giving me the freedom to develop and pursue my own ideas, being supportive and helping whenever I struggled, and providing distraction with the latest stories from the farm whenever things went south in the lab. Thank you for being a great supervisor. Fabian, thank you for always being there when I needed help, for never losing patience with me, and for all the wisdom on old-school movies. You were an amazing mentor. Thank you also to Shadi for all the excellent discussions and for always having a helping hand when needed, Florian for your patience explaining me how our lab equipment works and all the valuable information on chicken, and Felix for helping me learn how to teach and the great conversations over coffee. And thank you to the rest of the Physics of Nanoscale Systems group, especially Rolf. You always knew when to manage and when to rather share hiking/skiing stories or cake. Thank you for keeping things together.

Ein grosser Dank auch allen Freunden auf deren Unterstützung und Ablenkung ich immer zählen konnte. An all die 'alten Hasen' aus Schule und Studium: Ich bin froh, dass wir uns nie aus den Augen verloren haben und dass ihr weiterhin, wenn auch aufgrund der Entfernung meist digital, Teil meines Lebens seid. An alle, die ich während meiner Zeit hier kennenlernen durfte: Danke, dass ihr mich mit offenen Armen aufgenommen habt, ich will euch nicht mehr missen.

Der grösste Dank gebührt meiner Familie. Sandro, Mama, Opa: Ihr seid mein Halt, meine Stärke und manchmal auch meine Stimme der Vernunft. Ihr habt mich zu der Person gemacht die ich heute bin. Mit aller Gewichtung die ich in diese Worte legen kann: Danke für alles.